CHARACTERIZATION OF SOLID STATE MATERIALS FOR USE AS OPTICAL SPATIAL LIGHT MODULATORS

By

BAHMAN TAHERI

Bachelor of Science
California Polytechnic State University
San Luis Obispo, California, 1989

Masters of Science
Oklahoma State University
Stillwater, Oklahoma, 1992

Submitted to the Faculty of the
Graduate College of the
Oklahoma State University
in partial fulfillment of
the requirements for
the Degree of
DOCTOR OF PHILOSOPHY
December, 1994

CHARACTERIZATION OF SOLID STATE MATERIALS
FOR USE AS OPTICAL SPATIAL
LIGHT MODULATORS

Thesis Approved:

Richard C. Powell

Thesis Adviser

Jinjin Song

Paul Westhaus

Donna Kay Bandy

Thomas C. Collins

Dean of the Graduate College

ACKNOWLEDGEMENTS

In the following chapters I will be presenting an overview of my research at OSU. That means, I will present details about equipment, materials, and techniques that I used as well as the results that I obtained. So it is only fair that I devote this section to acknowledging some of the people who have been instrumental in the completion of this thesis.

As an undergraduate, I felt that I could get through life with my limited knowledge, bypassing any tedious work, like homework. My adviser at the time, Dr. Ron Zammit, was the first person, apart from my parents of course, to point out this flaw in my thinking. Within a year, I was determined to get my PhD in physics. The only problem was that by the time I had made up my mind to attend graduate school, the application deadline for most schools had passed. Fortunately, Dr. Westhaus accepted me into the program only a few days before the start of the academic year. A couple of classes with Dr. Nandi and the late, great Dr. Lafon and I was sure that I made the right decision to pursue a career as a physicist.

With enthusiasm, I started working for Dr. Richard Powell on nonlinear optics and solid state physics. As I expected, he exposed me to a number of different areas in optical physics, and on the way taught me the meaning of the term "hard labor". From his encouragement to attempt different ideas, I learned the importance of diverse thinking and from his constant push to do independent research, I learned self confidence. His belief in these ideas is no where more apparent than when he agreed to remain my adviser even after moving to the Optical Sciences Center at the University of Arizona. Up to today, almost two years later, he still converses with me on my projects. For all his help and confidence in me, I thank him.

The job of financial support, after Dr. Powell's departure, befell on Dr. R.J. Reeves who gladly accepted it, allowing me to get back to finishing my research. Nine months later, however, Dr. Reeves returned to New Zealand and again I was in limbo. At this point, Dr. Jin Joo Song took over. Even though she had no obligation, she offered me financial support asking for nothing in return. The smooth ride from that point to completion of this thesis is attributed to her. I thank her for her help in the hour that I needed it the most.

Now, I wish to express my gratitude to the people who were more directly involved in the research that I did. First, I wish to thank Drs. Istvan Foldvari, Baha Jassemnejad, Hiumin Liu and Antonio Munoz. In addition to providing me with necessities, like samples and technical assistance, they provided me with friendship. Their help and support has proven immeasurable and is greatly appreciated. Also, I wish to extended my deepest thanks to Dr. J. K. Furdyna for providing me with the semiconductor samples that I used in my research. His trust to send samples to an unknown graduate student after a brief conversation over the phone is to be admired. I also wish to thank my fellow graduate students, Scott Holmstrom (with whom I worked the most), Keith VerSteeg and Roger Petrin for their laboratory assistance. Finally, I wish to thank Dr. and Mrs. Wicksted for all their help, both professional and personal.

I wish to thank my other committee members, Drs. Donna Bandy, Jerzy Krasinski and Steve McKeever for their patience through the changes in my program.

None of this work could have even been initiated if it were not for the help of my parents who never hesitated to provide me with financial and emotional support. Even till today, I rely on them for the most important decisions of my life. Their belief in higher education and enjoyment of life has eased my most difficult decisions. To them I devote this work as well as any success that I have had or will have in the future.

TABLE OF CONTENTS

LIST OF TABLES

LIST OF FIGURES

Figure Page

Part A

BACKGROUND

CHAPTER I

INTRODUCTION

What are Optical Spatial Light Modulators?

As computers become faster and more powerful, the ultimate limitations on their electronic and architectural designs becomes more apparent. The electronic limitations stem from the fact that it is becoming increasing harder to reduce the size of the active elements. Even if we could shrink them as much as needed, the ultimate switching time would be dictated by the communication time between various elements. This time is determined by the RC time constant of the interconnect which does not decrease beyond a certain limit even with a decrease in the dimension. Furthermore, since currents are due to charged particles, electrons, the interference of adjacent interconnects severely hinders the operation of any micro electronic device. The architectural limitation is due to the 'sequential' method of computing where the computation process is separated from the memory and interconnection processes [1]. As indicated by its name, in sequential computing the instructions are implemented in sequence and therefore, the speed of the computer is dictated by the speed at which each instruction is executed. Increasing the number of processors working in 'parallel' increases the speed of computing by performing several instructions simultaneously. Unfortunately, increasing the number of processors does not increase the speed linearly. More realistically, the increase in the speed due to presence of n parallel processors is given by $n/\ln(n)$ and not n as expected [2].

There are several approaches currently undertaken to reduce these limitations. Optical interconnects, for example, decrease the constraint on the RC time constant as well as removing the limitation produced by interference between adjacent interconnects. There are also neural network approaches to computing which are aimed at resolving the 'sequential' computing problem. More recently, all optical switching has gained much interest due to its potential in ultrafast computing and pattern recognition. Currently, these techniques are at their infancy and as such are subject to intense research. The essence of optical switching is based on its counterpart, electronic switching. In the later case, conductivity of a component in an external field is determined by the presence of a second current (transistor) whereas in the former, the state of one beam is altered by the presence of the second. This alteration can take the form of a change in the beam's polarization, frequency, intensity or direction. Here we refer to devices that alter the direction of one beam due to the presence of the second as *Optical Spatial Light Modulators* (OSLM). This action can be fast (optical switching) or long lived (optical memory). Operation of all OSLM is based on the nonlinear optical properties of a material. It is, therefore, desirable to study these properties in various classes of materials to find the suitability of each class for this task. This is the main focus of this thesis.

Optical Switching via Polarization Rotation

As an example of Optical Spatial Light Modulation, a simple polarization rotation switch is used to construct an *AND* and an *OR* gate. We demonstrate this effect on a bulk CdTe where high efficiencies for this process are observed[3]. We then demonstrate the significance of some of the geometric factors involved in this configuration.

Experimental Setup

The experimental arrangement for a typical polarization rotation switch (SPR) is shown in Fig. 1 (a). In the two beam configuration shown, beam 1 is σ polarized while beam 2 is polarized at an angle with both σ and π components.

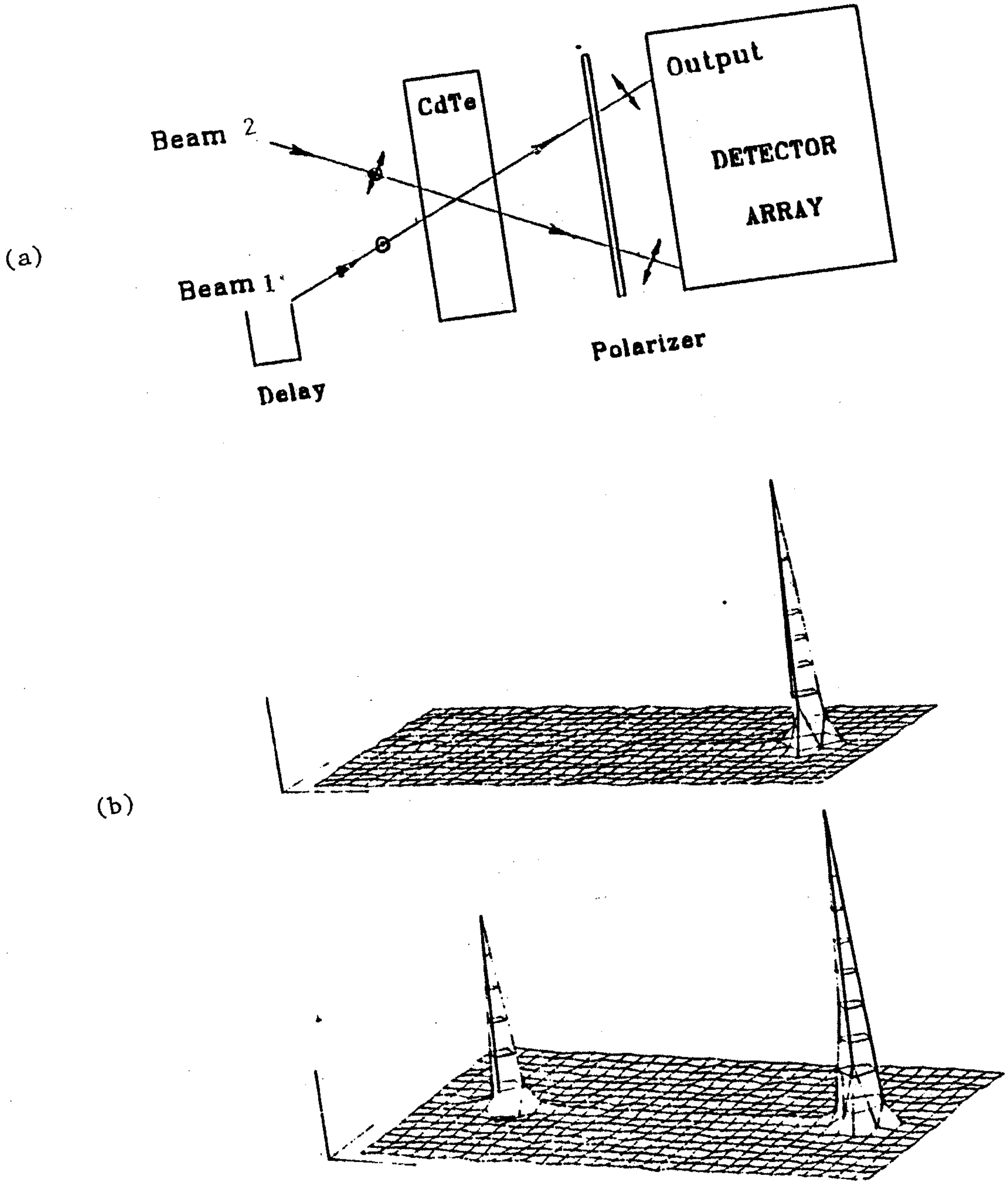

Figure 1. (a) Experimental setup for polarization rotation switches. (b) typical results obtained for CdTe. Note that the presence of both beams is required for a signal at the output detector.

With the optical delay line set so the pulses from beams arrive simultaneously and are spatially overlapped in the material, the σ components of the beam create an interference pattern within the sample. Free electron hole pairs are created in the light regions of the grating via two photon absorption. The presence of these free carriers alters the refractive index of the light region from the dark region. This index grating results in Bragg scattering of a portion of the π component of beam 2 in the direction of the transmitted beam 1 (see chapters 2 and 3). Using a polarizer in front of the detector allows monitoring of the scattered and transmitted π components. The laser used was a mode-locked, Q-switched Nd:YAG laser with 27 ps pulses at 1064 nm which is below bandgap excitation of the materials studied. Computer controlled optical delay lines provided timing within 1 ps. A Spiricon detector array was used for monitoring the transmitted beams. The size of each pixel in the two dimensional array was 60 μm in diameter with a pixel spacing of 740 μm which determines the resolution of the configuration. The crossing angle of the two beams and the sample thickness dictate the interaction length and in this study they were chosen to be 27^o and 1 mm respectively. Using the experimental arrangements described above a π polarized signal is detected at the output only in the presence of both beams (Fig. 1 b). This is the logic equivalent of an *AND* gate truth table.

For an *OR* gate logic a third beam, beam 3, containing both σ and π polarizations is also focused on the overlap region. A signal at the detector can be observed due to interaction of beam 1 with beam 2 *OR* beam 3. The condition of no signal at the detector can only be achieved if neither of the two beams (beam 2 or beam 3) is allowed to interact with beam 1. This is the logic equivalent to an *OR* gate for beams 2 and 3. Figure 2 shows the experiment geometry and the observed signal at the detector for the cases stated. In particular, in the absence of beam 2, beam 3 interacts with beam 1 as in the case of the *AND* gate described above. Similarly, in the presence of beam 2 and absence of beam 3, beam 1 interacts with beam 2 and results in a signal at the detector. If all three beams are

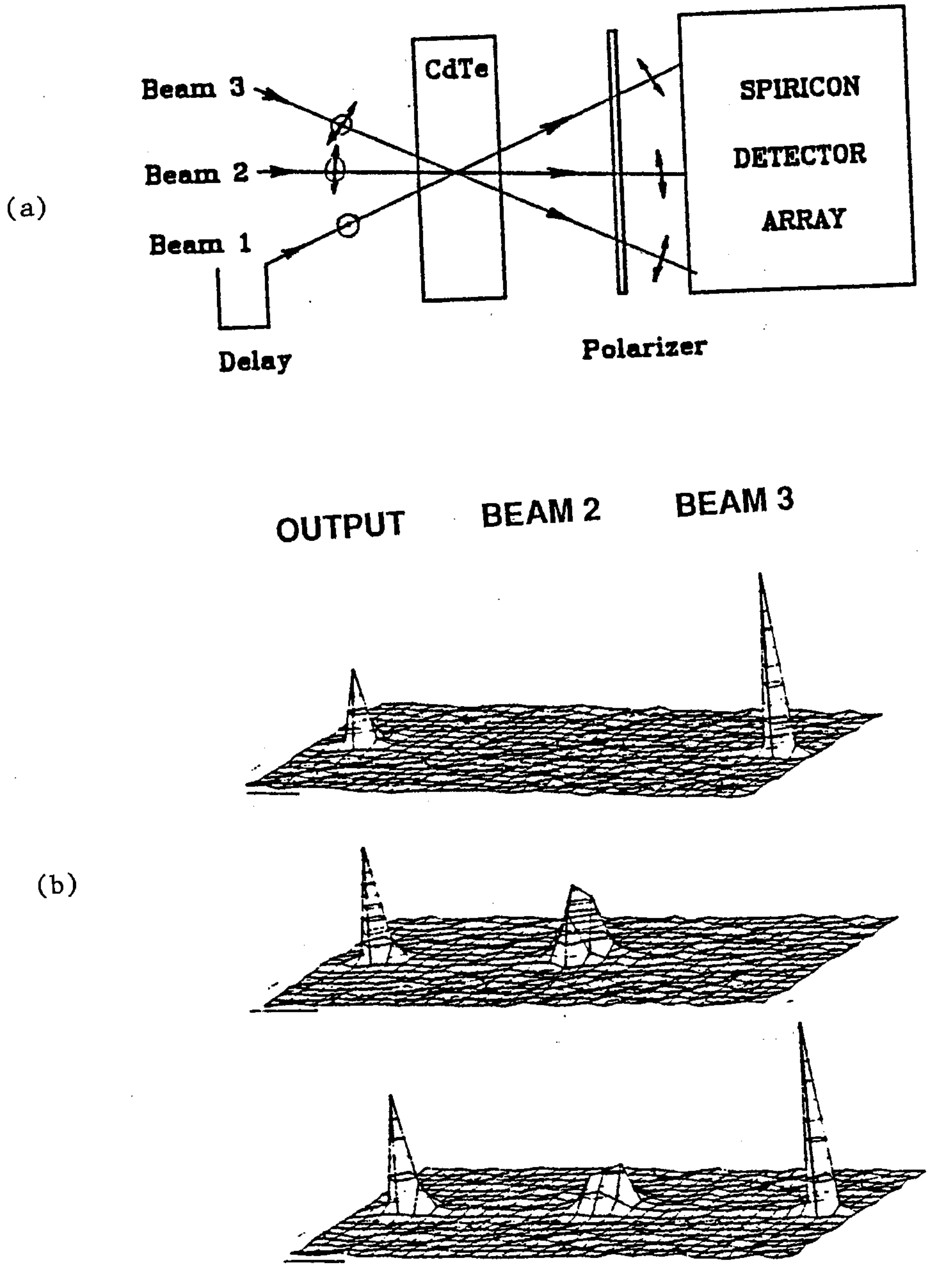

Figure 2. (a) Experimental setup and (b) typical results for use of polarization rotation as an .OR. gate for beams 2 and 3.

present, the signal at the detector is due to both interactions, i.e. beam 1 with beam 2 and beam 1 with beam 3.

Geometric Aspects

High efficiencies in SPR can be achieved with an increase in the interaction length through an increase in the sample thickness and/or beam crossing angle. However, these parameters are set by device specifications and their optimization varies with the usage of the switches. In this study the beam crossing angle and sample thickness were kept constant at 27^o and 1 mm respectively. Figure 3 demonstrates the variation of the SPR efficiency associated with various experimental parameters. The efficiency is defined as the signal energy divided by the total transmitted energy of the π component of beam 1. The first consideration is the relative difference in the polarization between the two beams. Using a beam 2/ beam 1 ratio of 2:1 with beam 2 fluence of 10 mJ/cm^2, the relative polarization between the beams that produced the optimum SPR efficiency was 45^o (Fig. 3.(a)). The results are not sharply peaked at this angle and a tolerance of $\pm 10^o$ is easily acceptable for device performance. The next parameter investigated was the ratio of the relative intensities using the relative polarization of 45^o between the beams, and a beam 2 fluence of 10 mJ/cm^2. As shown in Fig. 3 .(b), the maximum SPR efficiency was achieved when the fluence of beam 2 was twice that of beam 1. This is due to the fact that the scattering efficiency depends on the modulation depth of the laser induced grating and this is greatest for equal fluence of the interacting beams. Thus half of the fluence of beam 2 interact with equal fluence of beam 1 to produce a grating and the other half of beam 2 acts as the probe beam that scatters off the grating. Note that these results are sharply peaked at the maximum efficiency indicating that the accurate control of the relative beam fluence is critical for optimum device performance. Figure 3 (c) shows the results of the efficiency as a function of the relative delay between the two pulses. The peak efficiency is obtained at the zero delay between the two beams as expected. However, for the fluence used, the data is not sharply peaked at the zero delay

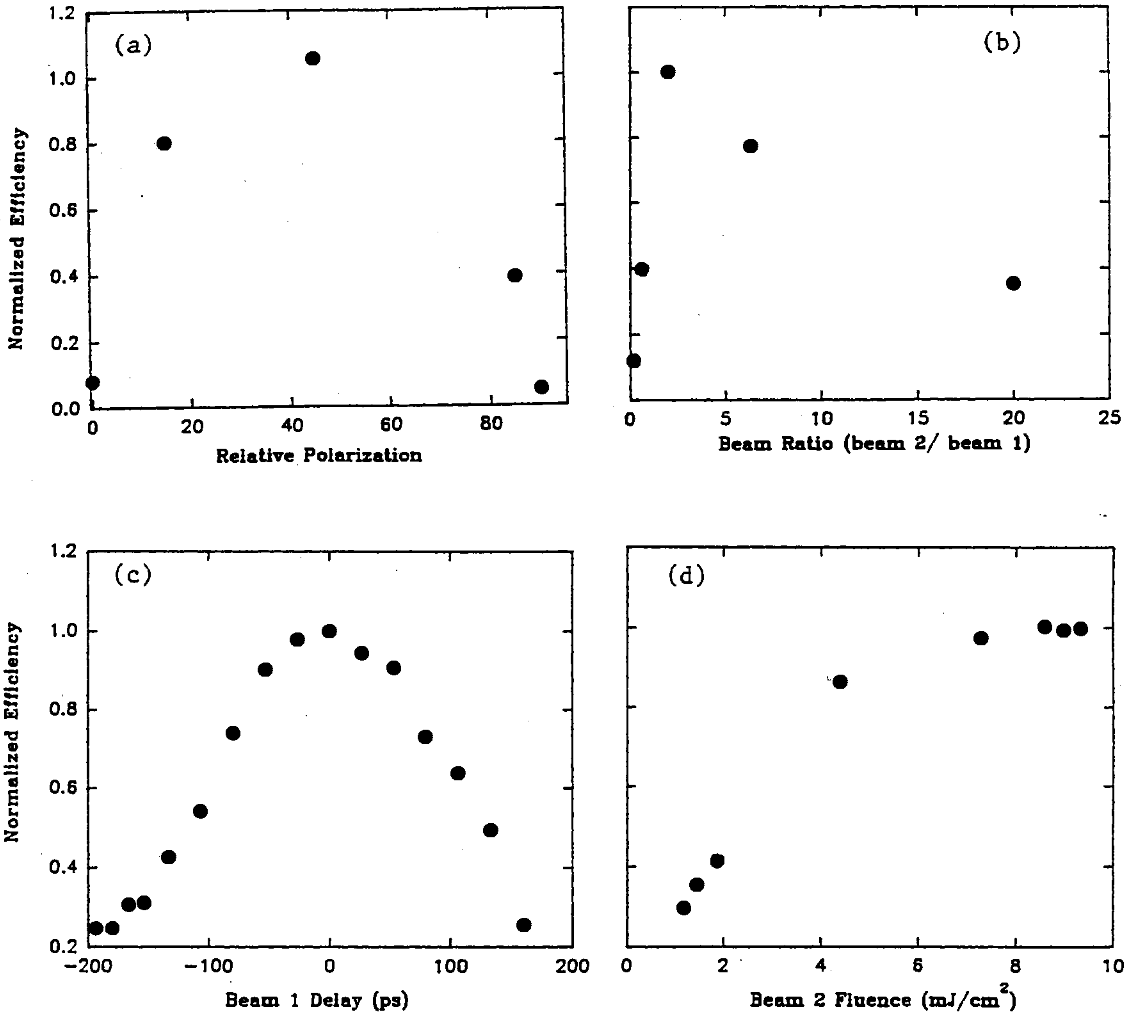

Figure 3. Dependence of the scattering efficiency of a PR switch on the experimental parameters.

value and a timing jitter of ±50 ps would not produce significant changes in the device performance. This result is surprising for pulses of 27 ps FWHM. It may be associated with the possible existence of long wings to the pulses or with the fact that the data were taken at fluence well above the saturation of $\chi^{(3)}$ response of the material. The effect of beam fluence is shown in Fig. 3.(d). It indicates that the efficiency increases quadratically with the total fluence of the two beams up to 7.5 mJ/cm^2. The saturation above this level, observed perviuosly, has been attributed to the free carrier absorption[3].

Optical interconnect via four wave mixing

As a second example of OSLM, forward propagating four wave mixing (FWM) is demonstrated as a possible means for optical switching and interconnect.

Experimental geometry

To demonstrate the full capability of FWM for optical interconnect, a folded boxcar geometry was used. Figure 4 shows the schematic for this two dimensional geometry. Beams A, B, and C form three corners of a box. They are focused in the material and the result is a box with beams at every corner. The scattered beams are monitored by a 2-dimensional Spiricon detector array. The out-of-plane Bragg reflection has several advantages over the conventional geometry presented earlier. First, this geometry can easily be reduced to the geometry used in the last section. For example, removal of beams B or C reduces this geometry used to the one used for an AND gate. Rotation of polarization of beams B or C allows the use of this configuration as an optical OR gate. Therefore all previous results would still apply. Second, additional detectors can be addressed in the two dimensional geometry that could not be addressed via the one-dimensional configuration. Third, this configuration can make use of current intermediate focal plane geometries that are based on two dimensional configurations.

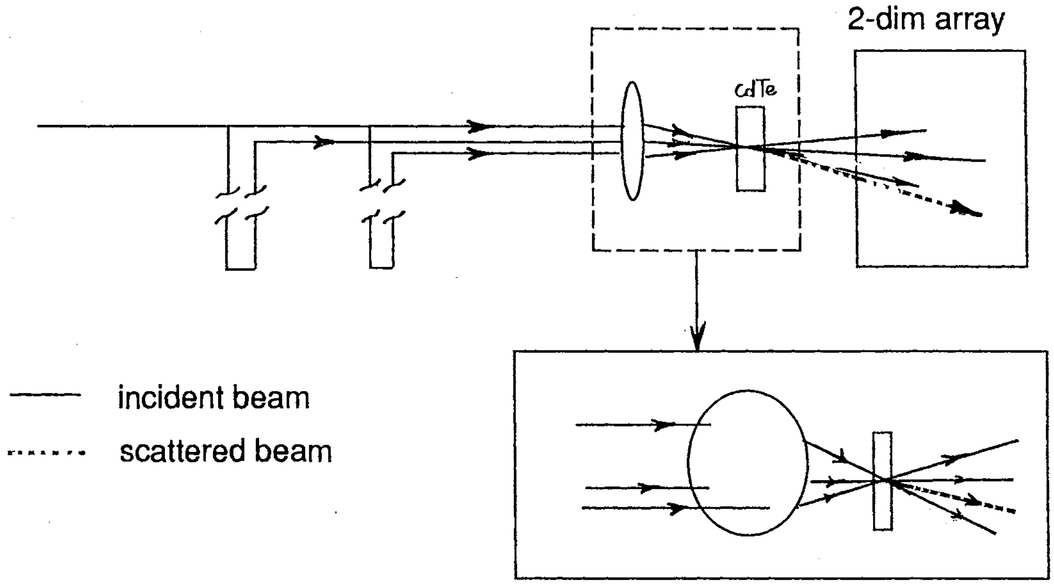

Figure 4. Experimental setup for forward propagating degenerate four wave mixing for use as optical interconnect. The scattered signal is represented in by dotted line.

In this geometry, at small crossing angles (0.1 radians), Bragg and Raman-Nath scattering are observed. This further increases the ability of the device to address different detectors. Figure 5 shows typical outputs observed at the Spircon detector array.

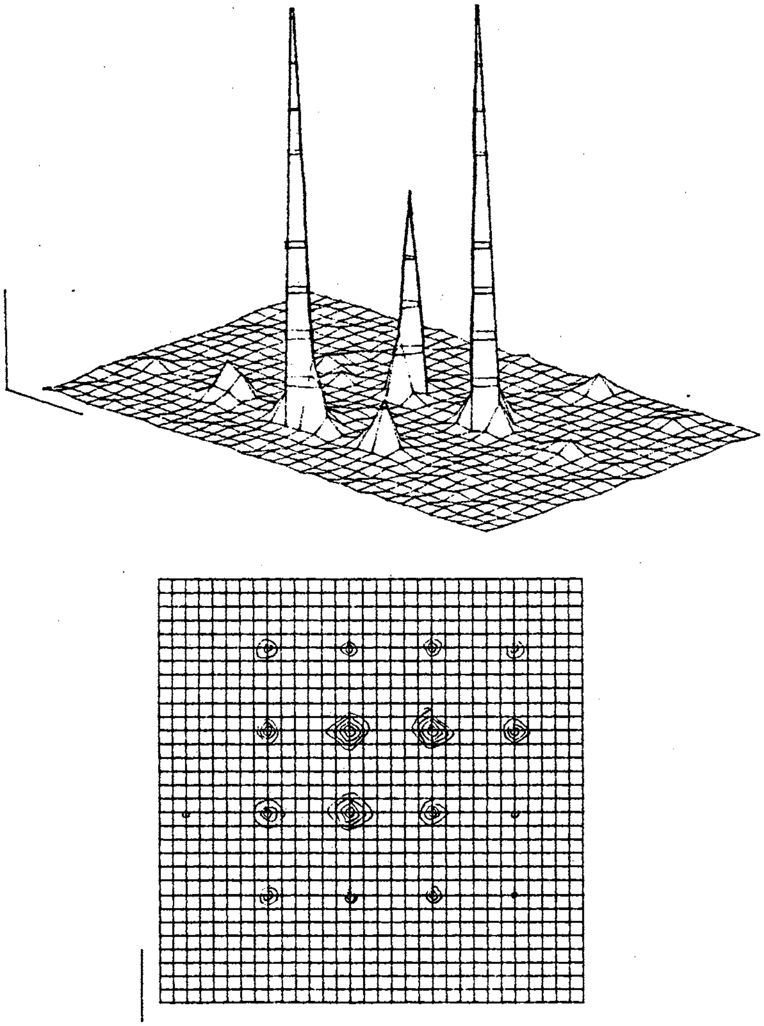

Figure 5. Typical results of Raman-Nath scattering in a forward propagating degenerate fourwave mixing geometry.

The presence of all three beams results in the fourth beam which is not present in the one-dimensional geometry. This should make it possible to develop a variety of different logic gates. For example, beam four used with one of the other first order diffracted beams (2 or 3) could yield a logic gate switch equivalent to a NOR or an XOR gate. Combined with the other combinations used for AND and OR gates design of any optical logic gate becomes possible.

The relative energies in each of the scattered spots is also a function of the three input beams. For example, removal of any beam results in the observation of Raman-Nath scattering between the remaining beams only. Figure 6 shows a summary of the method of isolation of specific spots.

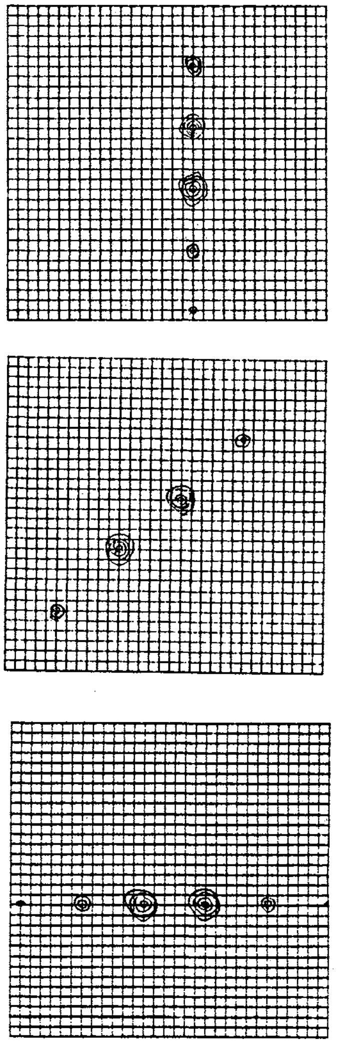

Figure 6. Isolation of connected detectors by blocking one of the incident beams.

Summary of Thesis

In the above examples we were able to obtain ultrafast switching using a rather simple technique. Even with geometric optimization, however, a powerful Nd:YAG, producing pulses of 27 ps in duration and a few milliJoules in energy was needed. Furthermore, each pulse is only able to activate one optical switch. In realistic optical computing a pulse should activate several optical switches. This factor produces the strongest limitation on these devices. To compensate for this short coming, we require more efficient switches. At this point we may proceed in two ways, (i) attempt to discover new and more efficient method or (ii) look for more suitable materials with higher switching capability. Since the latter is a requirement for any optically based switching, this work focuses on determining the relative size of optical nonlinearities in various materials.

With that in mind, the thesis is divided into three parts. In the first part, covering this chapter and and the next chapter, the reader is introduced to the goal of the thesis and the mathematical background needed to determine the suitability of a class of material. Chapter 2 is devoted to presentation of the mathematical formalism commonly used in relation to optical properties of a medium (both linear and nonlinear). Since the most common optical switches are based on third order nonlinearities, emphasis is placed on that term. In addition, scattering from a thick grating and propagation of a distorted wave front in free space are examined as these are needed to determine the optical coefficients. To save the reader from exhausting review of step-by-step derivation of known ideas, focus is placed on theories and equations directly used in the study. Any first principle calculations not in dire needs is placed in the appendices. In part two, we look at materials which are best suited for fast switching. These are materials which exhibit a large instantaneous response and a fast recovery time. Chapter 3 looks at the II-VI semiconductors containing Mn ions. Particularly, the effect of Mn concentration on the nonlinear optical and carrier dynamics of $Cd_xMn_{1-x}Te$ and $Cd_xMn_{1-x}Se$ are studied. In chapter 4 we present results obtained from C_{60} and C_{70} solutions as they are expected to exhibit large third order nonlinearities due to their delocalized π-electrons. In part three, we look at materials which are better known for the memory storage capabilities. Chapter 5 focuses on photorefractive materials. We focus on their two photon absorption coefficients as this is their main source of carrier generation under intense light illumination. The photorefractive behavior of BiTeO and SBN are also investigated. Finally, in chapter 6 we look at permanent refractive index changes in a number of Eu doped glasses. We will show the importance of network former and modifier ions in this process.

CHAPTER II

THEORETICAL

Linear Optics

Lorentz model

There are several formalisms to describe light-material interaction, but by far the most intuitive is the classical Lorentz model[4]. The model is as follows: let us assume that our material is made up of N nuclei per unit length, each having a single electron in orbit. The electric field of an incident electromagnetic wave induces a polarization in the electronic cloud of first row of atoms. The atoms, behaving as a dipole, oscillates with the same frequency as the incident wave. The phase of the dipole oscillation, however, lags the phase of the incident field. In other words, re-radiated light from the dipoles has the same frequency but a different phase from the incident wave. This means that the resultant wave, incident plus re-radiated, has a different phase from the incident. This wave is now the incident wave for the next row of atom which in turn encodes an additional phase change on it. Light emerging from the back surface of the medium, therefore, has undergone a phase change proportional to N. The phase change can be interpreted as an increase in the optical path length of the light due to the presence of the atoms. The increase is dependent on the material and is described by the refractive index coefficient. Such a model can easily be represented by a simple harmonic oscillator with equation of motion given by:

$$\frac{d^2x}{dt^2} + \Gamma\frac{dx}{dt} + \omega_o^2 x = -\frac{e}{m}E(\omega)e^{-i\omega t} + c.c. \tag{1}$$

with x denoting the displacement of the electron, m its mass, e its charge, ω_o its natural frequency, γ a damping constant and E the oscillating field of the applied light. This equation has a solution,

$$x = -\frac{e}{m} E \frac{e^{-i\omega t}}{\omega_o^2 - i\gamma\omega - \omega^2} + c.c. \tag{2}$$

Therefore, the complex susceptibility of the material with N molecules per unit volume, with f_j electrons in each molecule with binding frequency, ω_j, and damping constant, γ_j, is[5]:

$$\tilde{\chi} = \frac{Ne^2}{m} \sum_j \frac{f_j}{\omega_j^2 - i\gamma_j\omega - \omega^2} \tag{3}$$

In the above we have used the relation $P = -Nex = \chi E$. This susceptibility is related to the complex index of refraction of material through the dielectric constant, $\tilde{\epsilon}$:

$$\tilde{n}^2 = \tilde{\epsilon} = 1 + 4\pi\tilde{\chi} \tag{4}$$

Wave Equation

The above model, though intuitive, is too simplistic for our application. Alternatively, we may approach the problem from Maxwell's equations and neglect the microscopic nature of interactions. The light-atom interaction can then be studied from a semi-classical formalism. To show the form of the wave equation in a medium, we first start with Maxwell's equations. Following reference [6], Maxwell's equations in Gaussian units are:

$$\begin{aligned}
\nabla \cdot \mathbf{D} &= 4\pi\rho_{free} && \text{(Gauss's law)} \\
\nabla \cdot \mathbf{B} &= 0 && \text{(no name)} \\
\nabla \times \mathbf{E} &= -\frac{1}{c}\frac{\partial \mathbf{B}}{\partial t} && \text{(Faraday's law)} \\
\nabla \times \mathbf{H} &= \frac{1}{c}\frac{\partial \mathbf{D}}{\partial t} + \frac{4\pi}{c}\mathbf{J} && \text{(Ampère's law)}
\end{aligned} \tag{5}$$

where the symbols have their usual meaning and bold letters denote vector quantities. These are supplemented by additional relations known as material equations. For an isotropic medium, these equations are:

$$\begin{aligned}
\mathbf{D} &= \tilde{\varepsilon}\mathbf{E} \\
\mathbf{J} &= \tilde{\sigma}\mathbf{E} \\
\mathbf{B} &= \mu\mathbf{H}
\end{aligned} \tag{6}$$

Here, $\tilde{\varepsilon}$, $\tilde{\sigma}$, and μ are the complex dielectric constant, conductivity and the magnetic permeability, respectively. In addition, we have assumed that the macroscopic polarization, P, is proportional to the applied field, E:

$$\mathbf{P} = \frac{1}{4\pi}(\tilde{\varepsilon} - 1)\mathbf{E} = \tilde{\chi}\mathbf{E} \tag{7}$$

where $\tilde{\chi}$ is the material susceptibility. This equation is the same as its more common representation, $\mathbf{D} = \mathbf{E} + 4\pi\mathbf{P}$.

Having taken care of some definitions, we take the curl of the Faraday's equation:

$$\nabla \times (\nabla \times \mathbf{E}) = -\frac{1}{c}\frac{\partial}{\partial t}(\nabla \times \mathbf{B}) \tag{8}$$

Using the identity, $\nabla \times (\nabla \times \mathbf{E}) = \nabla(\nabla \cdot \mathbf{E}) - \nabla^2\mathbf{E}$ and Ampere's equation we get:

$$\nabla(\nabla \cdot \mathbf{E}) - \nabla^2\mathbf{E} = -\frac{\mu}{c}\frac{\partial}{\partial t}\left(\frac{\tilde{\varepsilon}}{c}\frac{\partial \mathbf{E}}{\partial t} + \frac{4\pi\tilde{\sigma}}{c}\mathbf{E}\right). \tag{9}$$

If we assume that $\rho_{free} \approx 0$, this reduces to:

$$\nabla^2 \mathbf{E} = \frac{\mu\tilde{\varepsilon}}{c^2}\frac{\partial^2 \mathbf{E}}{\partial t^2} + \frac{4\pi\mu\tilde{\sigma}}{c^2}\frac{\partial \mathbf{E}}{\partial t} \tag{10}$$

which is the general wave equation in a conducting medium.

We could have done this work in the Fourier space. The equation obtained is the scalar wave equation, also known as Helmholtz equation. The advantage of Helmholtz equation to Eq. 10 is that the latter is an ordinary differential equation. We can achieve the same effect if we assume a solution of the form $\sim Ee^{-i\omega t}$ for the wave equation[6]. With this assumption, Eq. 10 reduces to the Helmholtz equation:

$$\nabla^2 \mathbf{E} + \frac{\omega^2}{c^2}\mu\tilde{\epsilon}\mathbf{E} = 0 \tag{11}$$

where $\tilde{\epsilon}$ is the complex dielectric constant and is related to $\tilde{\varepsilon}$ and $\tilde{\sigma}$ by:

$$\begin{aligned} \tilde{\epsilon} &= (\tilde{\varepsilon} + i\frac{4\pi\tilde{\sigma}}{\omega}) \\ &= (\{\varepsilon_R + i\varepsilon_I\} + i\frac{4\pi}{\omega}\{\sigma_R + i\sigma_I\}) \end{aligned} \tag{12}$$

The real and imaginary parts of $\tilde{\epsilon}$ dictate phase and absorption of a light within a medium, respectively. For materials with small conductivity (insulators, undoped semiconductors) we can neglect contributions due to $\tilde{\sigma}$. In these cases we can define a complex refractive index as:

$$\sqrt{\tilde{\epsilon}} = \tilde{n} = n + i\frac{\alpha}{2k_o} \tag{13}$$

with $k_o = \omega/c = 2\pi/\lambda$ being the wavevector in free space, α the absorption coefficient and n the real index of refraction. The terms, index of refraction and the refractive index are used interchangeably in literature. However, to distinguish the difference between the complex refractive index and its real part, $\tilde{n}$ is refered to as the refractive index and n as the index of refraction.

Up to this point, we have not yet specified any special limitations on the material parameters, $\tilde{\epsilon}$ and $\tilde{n}$. They can be constants or functions of the spatial coordinated. Depending on the medium, they can be purely real (vacuum) or highly complex (metals). Additionally, they may exhibit dispersion with respect to the incident fields frequency. The only constraint that is imposed for now is that they are not functions of electric field. Later, in the nonlinear optics section, even this constraint is relaxed.

Propagation in free space

The first case investigated is the simplest one, in vacuum. Here, dielectric function is purely real and has a numerical value of 1. In effect, this states that the light wave travels at the speed, c, and is not absorbed. Furthermore, the dispersionless vacuum means that the pulse shape of the wave is not altered by propagation. Therefore, the time dependence does not play a role and we can use the Helmholtz's scalar wave equation to describe the propagation.

The approach that we take to solve this problem is based on Huygen's principle[6]. It states that every point in space is a source of radiation of spherical waves of the form, $E \sim E_o e^{ikr}/r$. Where the strength of the field, E_o, depends on the strength of the primary source of radiation at that point. Each of these points, inturn, behave as a source of a secondary spherical wave. Now, the field at every point on a wavefront is the summation of the fields at that point from all the points preceding it. This point becomes clearer as the discussion continues but for now we restrain ourselves from an in depth explanation of the origin of this principle. The interested reader may refer to any optics books such as ref. [6]. Fresnel added a postulate that these secondary waves interfere with each other (Huygen-Fresnel Principle). So for example, we can have a source of light, followed by an infinite screen with an opening in it. Then, according to the principle, the light on the other side of the screen is made up from interference of a series of spherical lights originating at the opening. We can use this principle to find the scalar field at any point given the field at the earlier point. This is given by (see appendix A):

$$E(P_2) = -\frac{ik_o}{2\pi}\int_S E(P_1)\frac{e^{ikr}}{r}dS \tag{14}$$

In the above, the integration is over all possible secondary sources, and e^{ikr}/r is the field at a distance, r, from a source, $P1$, of a secondary wave. The strength at the origin of the secondary wave is $E(P1)$, and it determines the contribution from that source. The phase factor, i, is necessary for a correct reconstruction of the wave[6], and it means that the secondary wave is out of phase with respect to the primary.

Using Fig. 7 we can expand r in terms of (x_1, y_1, z_1) and (x_2, y_2, z_2) to find:

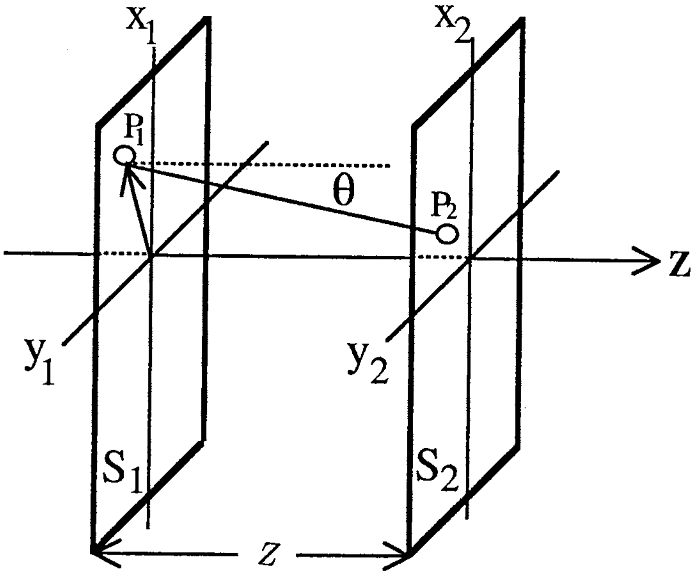

Figure 7. Coordinate specification for a propagating light.

$$r = (z_2 - z_1)\sqrt{1 + \left(\frac{x_2 - x_1}{z_2 - z_1}\right)^2 + \left(\frac{y_2 - y_1}{z_2 - z_1}\right)^2} \tag{15}$$

If we define $Z = (z_2 - z_1)$ and assume that $Z \gg (x_2 - x_1)$ and $(y_2 - y_1)$ we can use binomial expansion $(1 + x)^{1/2} \simeq 1 + x/2$ to get:

$$r \simeq Z\left(1+\frac{1}{2}\left[\frac{x_2-x_1}{Z}\right]^2+\frac{1}{2}\left[\frac{y_2-y_1}{Z}\right]^2\right) \tag{16}$$

Rewriting in terms of polar coordinate we have:

$$r \simeq Z+\frac{1}{2Z}\{\rho_1^2+\rho_2^2-2\rho_1\rho_2\cos(\theta_1-\theta_2)\} \tag{17}$$

Finally, we substitute this into Eq. 14:

$$E(\rho_2,z_2)=-\frac{i}{Z\lambda}e^{ikZ}e^{i(k/2Z)\rho_2^2}\int E(\rho_1,z_1)e^{i(k/2Z)\rho_1^2}\rho_1 d\rho_1\int e^{(-ik/Z)\rho_1\rho_2\cos(\theta_1-\theta_2)}d\theta_1$$

We can write the angular integral using zeroth order Bessel function[7]:

$$E(\rho_2,z_2)=-\frac{i}{Z\lambda}e^{ikZ}e^{i(k/2Z)\rho_2^2}\int E(\rho_1,z_1)e^{i(k/2Z)\rho_1^2}\mathrm{J}_o(k\rho_1\rho_2/Z)\rho_1 d\rho_1 \tag{18}$$

This is the Kirchoff's diffraction integral and can be used to evaluate a field at any point given the field at earlier location. It should be noted that the time dependence in the field is implicitly implied.

Propagation in a homogeneous medium

Having formulated free space propagation we turn our attention to propagation in a medium. For simplicity we use a nonconducting ($\sigma = 0$) homogeneous medium. Returning to Helmholtz equation:

$$\nabla^2\mathbf{E}+k_o^2\tilde{\varepsilon}\mathbf{E}=0 \tag{19}$$

a constant and dispersionless $\tilde{\varepsilon}$ is assumed. For a field of the form $\mathbf{E}=\mathcal{E}e^{i\phi}$, the above reduces to:

$$2i\frac{\partial\mathcal{E}}{\partial z}\frac{\partial\phi}{\partial z}-\mathcal{E}\left(\frac{\partial\phi}{\partial z}\right)^2+k_o^2\tilde{\varepsilon}\mathcal{E}=0 \tag{20}$$

In the above we have invoked the slowly varying amplitude and phase approximation (SVAPA). This assumption states that amplitude and phase of the field are not significantly altered within one wavelength[8]. In general, this is an excellent approximation for a thin, absorbing medium.

To have Eq. 20 satisfied, it is necessary to have the real and the imaginary parts of the equation be independently zero. Remembering that the dielectric function, $\tilde{\varepsilon}$, is a complex quantity, the equations become:

$$\begin{aligned} \mathcal{E}\left(\frac{\partial\phi}{\partial z}\right)^2 &= k_o^2\varepsilon_R\mathcal{E} \\ 2\frac{\partial\mathcal{E}}{\partial z}\frac{\partial\phi}{\partial z} &= -k_o^2\varepsilon_I\mathcal{E} \end{aligned} \tag{21}$$

These two can be solved to give two uncoupled differential equations for the amplitude and the phase variation due to a media:

$$\begin{aligned} \frac{\partial\phi}{\partial z} &= k_o\sqrt{\varepsilon_R} \\ \frac{\partial\mathcal{E}}{\partial z} &= -\frac{k_o\varepsilon_I}{2\sqrt{\varepsilon_R}}\mathcal{E} \end{aligned} \tag{22}$$

We can also relate these equations to the complex refractive index, $\tilde{n} = n + i\alpha/2k_o$ since,

$$\begin{aligned} \tilde{\varepsilon} &= \left(n + i\frac{\alpha}{2k_o}\right)^2 \\ \varepsilon_R + i\varepsilon_I &= \left(n^2 - \frac{\alpha^2}{4k_o^2}\right) + i\left(\frac{n\alpha}{k_o}\right) \end{aligned} \tag{23}$$

In the limit of SVAPA, $n^2 \gg \alpha^2/4k_o^2$, so we get $n \simeq \sqrt{\varepsilon_R}$ and $\alpha \simeq k_o\varepsilon_I/\sqrt{\varepsilon_R}$. Therefore, it can be concluded that:

$$\begin{aligned} \frac{\partial\phi}{\partial z} &= k_o n \quad \Rightarrow \quad \phi = nk_o z \\ \frac{\partial\mathcal{E}}{\partial z} &= -\frac{\alpha}{2}\mathcal{E} \quad \Rightarrow \quad \mathcal{E} = \mathcal{E}_o e^{-\alpha z/2} \end{aligned} \tag{24}$$

which is exactly as expected. The first equation is the simple restatement of the role of index of refraction in alteration of the optical path length. The second is better known as Beer's law of exponential absorption of light in absorbing media.

An important point that must be re-emphasized is that these equations are strictly valid for a monochromatic light. In the event that the dispersion of the material is significant or the incident field has a time dependence it is necessary to use the time dependant wave equation (Eq. 10). However, that approach readily reduce to the above if the thickness of the sample is smaller than the length of the pulse in space ($c \times pulsewidth$)[9]. In the experiments presented in this thesis this condition holds, therefore, this formalisms is followed throughout this work.

Diffraction from a thick grating

As a final application of the Helmholtz equation in linear optics, we apply it to a medium with a periodic modulation in its dielectric constant of a form:

$$\tilde{\varepsilon} = \tilde{\varepsilon}_o + \tilde{\varepsilon}_1(1 + \cos(\mathbf{q} \cdot \mathbf{r})) = \tilde{\varepsilon}'_o + \tilde{\varepsilon}_1 \cos(\mathbf{q} \cdot \mathbf{r}) \tag{25}$$

with $|\mathbf{q}| = 2\pi/\Lambda$ and $\varepsilon_o \gg \varepsilon_1$. In this case Eq. 19 becomes:

$$\nabla^2 \mathbf{E} + k_o^2 \tilde{\varepsilon}(x, z)\mathbf{E} = 0 \tag{26}$$

An incident plane wave with wave-vector, $\mathbf{k}_i$, and amplitude A_i undergoes diffraction from such a pattern much like X-ray diffraction off a periodic lattice in a crystal. At certain exit angles, coherent summation of scattered light occurs. This is dictated by the Bragg condition[10]:

$$\mathbf{k}_m = \mathbf{k}_i + m\mathbf{q} \text{ with } m = 0, \pm 1, \pm 2, ... \tag{27}$$

where $\mathbf{k}_m$ is the wave vector of the diffracted beam and has a magnitude equal to that of the incident beam, i.e. $|\mathbf{k}_m| = |\mathbf{k}_i|$. We can solve the Helmholtz equation by assuming a solution made from an infinite number of plane wave with wave-vector

$\mathbf{k}_m$. For an H-polarized wave, the Helmholtz equation becomes a scalar equation with $E \sim E(x,z)$ given by:

$$E(x,z) = \sum_{m=-\infty}^{\infty} S_m(z)\exp(i\mathbf{k}_m\cdot\mathbf{r}) + c.c. \tag{28}$$

where $\mathbf{k}_m$ is the wave vector within the material[11]. If this is substituted into Eq. 26, assuming that:

$$\mathbf{q} = \mathbf{q}_x = q \tag{29}$$

we get:

$$\sum_m \left[\frac{\partial^2 S_m}{\partial z^2} + 2i(\mathbf{k}_i)_z\frac{\partial S_m}{\partial z} - \{(\mathbf{k}_m\cdot\mathbf{k}_m) + k_o^2(\tilde{\varepsilon}_o' + \frac{\tilde{\varepsilon}_1}{2}\left(e^{i\mathbf{q}\cdot\mathbf{r}} + e^{-i\mathbf{q}\cdot\mathbf{r}}\right))\}S_m\right]e^{i\mathbf{k}_m\cdot\mathbf{r}} = 0 \tag{30}$$

Using the Bragg condition (Eq. 27):

$$\sum_m \left[\frac{\partial^2 S_m}{\partial z^2} + 2i(\mathbf{k}_i)_z\frac{\partial S_m}{\partial z} - (k_i^2 - k_o^2\tilde{\varepsilon}_o')S_m + \frac{k_o^2\tilde{\varepsilon}_1}{2}(S_{m+1} + S_{m-1})\right]e^{i\mathbf{k}_m\cdot\mathbf{r}} = 0 \tag{31}$$

This equation must be satisfied for all values of m. Therefore, in SVAPA, we have:

$$2i(\mathbf{k}_i)_z\frac{\partial S_m}{\partial z} + (k_o^2\tilde{\varepsilon}_o' - k_i^2)S_m + \frac{k_o^2\tilde{\varepsilon}_1}{2}(S_{m+1} + S_{m-1}) = 0 \tag{32}$$

This is known as the coupled-wave equation[12]. If we assume that the grating is thick, only the zeroth and first order terms survive. Assuming that the incident beam makes an angle, θ, with the z-axis and using $k_i^2 = \tilde{n}^2 k_o^2$ where $\tilde{n}^2 = \tilde{\varepsilon}_o$ the above reduces to:

$$\begin{aligned}\frac{\partial S_o}{\partial z} &= i\frac{k_o\tilde{\varepsilon}_1}{2\tilde{n}\cos\theta}S_o + i\frac{k_o\tilde{\varepsilon}_1}{4\tilde{n}\cos\theta}S_1\\ \frac{\partial S_1}{\partial z} &= i\frac{k_o\tilde{\varepsilon}_1}{2\tilde{n}\cos\theta}S_1 + i\frac{k_o\tilde{\varepsilon}_1}{4\tilde{n}\cos\theta}S_o\end{aligned} \tag{33}$$

The solution to this set of coupled first-order differential equation with the boundary condition of $S_o(z=0) = A_i$ and $S_1(z=0) = 0$ is:

$$\begin{aligned} S_o &= A_i \exp\left(i\frac{k_o\tilde{\varepsilon}_1}{2\tilde{n}\cos\theta}z\right)\cos\left(\frac{k_o\tilde{\varepsilon}_1}{4\tilde{n}\cos\theta}z\right) \\ S_1 &= iA_i \exp\left(i\frac{k_o\tilde{\varepsilon}_1}{2\tilde{n}\cos\theta}z\right)\sin\left(\frac{k_o\tilde{\varepsilon}_1}{4\tilde{n}\cos\theta}z\right) \end{aligned} \tag{34}$$

The dielectric change, $\tilde{\varepsilon}_1$, can be related to the more commonly used material parameters, n and α:

$$\begin{aligned} \tilde{\varepsilon} &= \tilde{n}^2 = n + i\alpha/2k_o \\ \tilde{\varepsilon}_1 &= \Delta\tilde{\varepsilon} \simeq 2\tilde{n}\Delta\tilde{n} = 2\tilde{n}(\Delta n + i\Delta\alpha/2k_o) \end{aligned} \tag{35}$$

Therefore,

$$\begin{aligned} S_o &= A_i \exp\left(i\frac{k_o\Delta n}{\cos\theta}z\right)\exp\left(-\frac{\Delta\alpha}{2\cos\theta}z\right)\cos\left(\frac{k_o\Delta n + i\Delta\alpha/2}{2\cos\theta}z\right) \\ S_1 &= iA_i \exp\left(i\frac{k_o\Delta n}{\cos\theta}z\right)\exp\left(-\frac{\Delta\alpha}{2\cos\theta}z\right)\sin\left(\frac{k_o\Delta n + i\Delta\alpha/2}{2\cos\theta}z\right) \end{aligned} \tag{36}$$

The two waves, transmitted and diffracted, are given by:

$$E_m = \frac{1}{2}\left\{S_m \exp\left(-\frac{\alpha}{2\cos\theta}z\right)\exp\left(i\frac{k_o n}{\cos\theta}z\right) + c.c.\right\} \tag{37}$$

The intensity of the transmitted and diffracted beams, normalized to the input intensity, I_i, is:

$$\begin{aligned} \frac{I_o}{I_i} &= \exp\left(-\frac{\alpha+\Delta\alpha}{\cos\theta}z\right)\left[\cos^2\left(\frac{k_o\Delta n\ z}{2\cos\theta}\right) + \cosh^2\left(\frac{\Delta\alpha\ z}{4\cos\theta}\right) - 1\right] \\ \eta = \frac{I_1}{I_i} &= \exp\left(-\frac{\alpha+\Delta\alpha}{\cos\theta}z\right)\left[\sin^2\left(\frac{k_o\Delta n\ z}{2\cos\theta}\right) + \sinh^2\left(\frac{\Delta\alpha\ z}{4\cos\theta}\right)\right] \end{aligned} \tag{38}$$

Which is the desired solution and somewhat more general than the one in ref.[11]. A few points of interest about this result. $\Delta\alpha$ and Δn are the average values for the absorption and index changes in the grating. In addition there is a energy transfer between the two beams, extension of which is determined by the change in the optical path length due to the presence of the grating.

Nonlinear Optics

Nonlinear Polarization

Up to this point we have assumed that the polarizability of the material was a constant. At this stage we relax this requirement. This leads to the branch of optics known as nonlinear optics. In terms of the Lorentz model presented earlier, when the intensity of the incident light is increased, a simple harmonic oscillator model is no longer sufficient for description of light-atom interaction. It can, however, be modified by inclusion of higher order terms, i.e. Eq. 1 becomes:

$$\frac{d^2x}{dt^2} + 2\Gamma\frac{dx}{dt} + \omega_o^2 x + ax^2 + bx^3 + \cdots = -\frac{e}{m}E(\omega)e^{-i\omega t} + c.c \tag{39}$$

where all the terms have their previous meaning. We are, also, assuming that there is only one incident wave with a single frequency. The additional terms result in an anharmonic behavior of the electronic displacement, x. In this case, the oscillation of the electron is at a frequency dictated by a combination of the frequency of the incident light and its higher harmonics[9]. Equation 39 does not have an exact solution, but if the higher order terms are small (as they usually are), we can solve it to successive order of approximation by Taylor series expansion of x in terms of the applied field, E. Alternatively, we can perform this expansion in the polarization of the atom in the form:

$$P = \chi^{(1)}E + \chi^{(2)}EE + \chi^{(3)}EEE + \cdots \tag{40}$$

where $\chi^{(n)}$ is a tensor of rank $n+1$ and tensoral multiplication is implied. Each tensor element also exhibits dispersion. The effect of this field dependence can be categorized as follows:

(i) Production of fields at different frequencies.

(ii) Alteration of the macroscopic parameters, n, and α.

For each order both of the above cases occur with a strength dictated by the dispersion dependence of the tensor elements. For example, $\chi^{(2)}$ tensor accounts for both, second harmonic generation and the linear electro-optic effect. The $\chi^{(3)}$ term gives rise to third harmonic generation and the Optical Kerr effect. Table I list some of the common processes in nonlinear optics and the order of the process [13].

Waves in a Nonlinear Medium

Here we focus on the effects of field dependant polarization on the macroscopic material parameters. Interested reader can refer to ref. [4] for frequency conversion properties. Furthermore, the field dependent susceptibility formalism is used since in this case we can retain all the information obtained in the linear optics section with a simple modification to the susceptibility,

$$\chi = \chi^{(1)} + \chi^{(2)}E + \chi^{(3)}EE + \cdots \tag{41}$$

which implies that

$$\tilde{\varepsilon} = 1 + 4\pi\tilde{\chi} = 1 + 4\pi(\chi^{(1)} + \chi^{(2)}E + \chi^{(3)}EE + \cdots) \tag{42}$$

since χ is complex,

$$\begin{aligned} \varepsilon_R &= 1 + 4\pi(\chi_R^{(1)} + \chi_R^{(2)}E + \chi_R^{(3)}EE + \cdots) \\ \varepsilon_I &= 4\pi(\chi_I^{(1)} + \chi_I^{(2)}E + \chi_I^{(3)}EE + \cdots) \end{aligned} \tag{43}$$

To write this in terms of the refractive index, we recall that while ε and χ are tensors, $1/n$ has tensoral properties. Full tensoral treatment of the problem can be greatly simplified with proper choice of the principle axis. In this case, the refractive index and the dielectric function can be treated as constants and are related by, using Eq. 42,

$$\frac{1}{n^2(E)} = \frac{1}{\varepsilon} = \frac{1}{\varepsilon}\left(1 + \frac{4\pi\chi^{(2)}E}{\varepsilon} + \frac{4\pi\chi^{(3)}EE}{\varepsilon} + \cdots\right)^{-1} \tag{44}$$

Since $\varepsilon \gg \chi^{(n)}E^{(n-1)}$, field dependence of the index components are:

TABLE I Nonlinear optical processes and their order.

Process	Order n	$-\omega_\sigma;\omega_1,\ldots,\omega_n$	K
Linear absorption/emission and refractive index	1	$-\omega;\omega$	1
Optical rectification (optically-induced d.c. field)	2	$0;\omega,-\omega$	$\frac{1}{2}$
Pockels effect (linear electrooptic effect)	2	$-\omega;0,\omega$	2
Second-harmonic generation	2	$-2\omega;\omega,\omega$	$\frac{1}{2}$
Sum- and difference-frequency mixing, parametric amplification and oscillation	2	$-\omega_3;\omega_1,\pm\omega_2$	1
d.c. Kerr effect (quadratic electrooptic effect)	3	$-\omega;0,0,\omega$	3
d.c.-induced second-harmonic generation	3	$-2\omega;0,\omega,\omega$	$\frac{3}{2}$
Third-harmonic generation	3	$-3\omega;\omega,\omega,\omega$	$\frac{1}{4}$
General four-wave mixing	3	$-\omega_4;\omega_1,\omega_2,\omega_3$	$\frac{3}{2}$
Third-order sum- and difference-frequency mixing	3	$-\omega_3;\pm\omega_1,\omega_2,\omega_2$	$\frac{3}{4}$
Coherent anti-Stokes Raman scattering	3	$-\omega_{AS};\omega_P,\omega_P,-\omega_S$	$\frac{3}{4}$
Optical Kerr effect (optically-induced birefringence), cross-phase modulation, stimulated Raman scattering, stimulated Brillouin scattering	3	$-\omega_S;\omega_P,-\omega_P,\omega_S$	$\frac{3}{2}$
Intensity-dependent refractive index, optical Kerr effect (self-induced and cross-induced birefringence), self-focusing, self-phase and cross-phase modulation, degenerate four-wave mixing	3	$-\omega;\omega,-\omega,\omega$	$\frac{3}{4}$
Two-photon absorption/ionisation /emission	3	$-\omega_1;-\omega_2,\omega_2,\omega_1$ or $-\omega;-\omega,\omega,\omega$	$\frac{3}{2}$ $\frac{3}{4}$

$$\frac{1}{n^2(E)} \simeq \frac{1}{n^2(0)} - \frac{4\pi\chi^{(2)}E}{\varepsilon^2} - \frac{4\pi\chi^{(3)}EE}{\varepsilon^2} + \cdots \tag{45}$$

Using $d(n^{-2}) = -2dn/n^3$ we get

$$\Delta n = \frac{2\pi}{n_o}(\chi^{(2)}E + \chi^{(3)}EE + \cdots) \tag{46}$$

Therefore an incident light undergoes additional phase and amplitude modulations. So, using Eq. 24:

$$\begin{aligned} \frac{\partial\phi}{\partial z} &= k_o(n + \frac{2\pi}{n}\chi_R^{(2)}E + \frac{2\pi}{n}\chi_R^{(3)}EE + \cdots) \\ \frac{\partial\mathcal{E}}{\partial z} &= -\tfrac{1}{2}(\alpha + \frac{4\pi k_o}{n}(\chi_I^{(2)}E + \chi_I^{(3)}EE + \cdots))\mathcal{E} \end{aligned} \tag{47}$$

and therefore,

$$\begin{aligned} n &= n_o + \frac{2\pi}{n_o}(\chi_R^{(2)}E + \chi_R^{(3)}EE + \cdots) \\ \alpha &= \alpha_o + \frac{4\pi k_o}{n_o}(\chi_I^{(2)}E + \chi_I^{(3)}EE + \cdots) \quad . \end{aligned} \tag{48}$$

At this point two types of applied fields are considered:

(i) *d.c. field with amplitude* E_1. A d.c. field (external, internal or induced by other nonlinear processes) alters the refractive index, $\tilde{n}$, through $\chi^{(2)}$ and $\chi^{(3)}$ tensors. Changes due to $\chi^{(2)}$ through the linear electrooptic coefficient are known as the Pockel effect. Changes due to $\chi^{(3)}$ through the quadratic electrooptic coefficient are known as the d.c. Kerr effect. In the presence of both terms, Pockel effect usually dominates those due to Kerr effect. Quantitatively, we represent these effects as:

$$\begin{aligned} n &= n_o + \frac{1}{2}n_o^3 rE_1 + \cdots \\ \alpha &= \alpha_o + \frac{1}{2}n_o^3 r' E_1 + \cdots \end{aligned} \tag{49}$$

where r and r' are the linear electro-optic and electro-chromatic coefficients and are related to $\chi^{(2)}$, (see appendix B). In the above we have omitted the d.c. Kerr effect which is not used in this work.

(ii) *Oscillating field with amplitude E_2 and frequency ω.* In the event of an oscillating field, the average (over an optical cycle) of first order changes due to $\chi^{(2)}$ is zero. Second order changes can occur through optical rectification followed by electrooptic effect. However, these effects are of order of $\left[\chi^{(2)}\right]^2$ which are in general negligible. Therefore, the first dominant nonlinear terms is due to $\chi^{(3)}$. In this case, the index of refraction is altered by the intensity of the field which has nonzero average over one optical cycle. Therefore, in this case we have:

$$\begin{aligned} n &= n_o + n_2 I_2 \\ \alpha &= \alpha_o + \beta I_2 \end{aligned} \tag{50}$$

Where n_2 and β are the Kerr and two photon absorption coefficients respectively. They can also containing all the terms arising from $\chi^{(3)}$, including the d.c. Kerr and the third order photo-chromatic coefficients.

Therefore, we can write the index in terms of a d.c. field and an intensity as follows:

$$\begin{aligned} n &= n_o + \tfrac{1}{2} n_o^3 r E + n_2 I \\ \alpha &= \alpha_o + r' E + \beta I \end{aligned} \tag{51}$$

Origins of refractive index changes

Thusfar, we have focused on the results of nonlinearities in the susceptibility tensor of a material. At this point we present the role of the material in the magnitude of the changes. The role of different constituents is divided in to categories based on their response time.

Bound Electrons. By far the fastest rise and decay time for optical nonlinearities are those due to bound electrons. By bound electrons, we are referring to the electrons which do not participate in conduction. In particular, we use the valence band electrons as the model for the calculations. This problem has been studied extensively[14], [15], [16], [17] and has more recently been invoked to a wide range of solids. We follow, closely, the works of these authors which use the same method for the determination of the nonlinear parameters. The basic approach is to determine the material parameters involved in the two photon absorption process. A Kramer-Kronig transformation of the result yields the corresponding index changes. For two, co-linearly polarized beams with polarization, $\hat{\mathbf{n}}$, with vector potential of

$$\mathbf{A} = \hat{\mathbf{n}}(A_{01}\cos(\omega_1 t) + A_{02}\cos(\omega_2 t + \phi)) \tag{52}$$

the interaction with the bands is given by[18]:

$$H_{int} = -\frac{e}{m_e c}\mathbf{A}\cdot\mathbf{P} \tag{53}$$

Here, m_e, and $\mathbf{P}$ are the electron mass and momentum operator, respectively. Using 'Dressed' states which are the system's eigenstates comprises of the atom *and* the field, the transition probability is given by the S-matrix[18]:

$$S = -\frac{i}{\hbar}\int dt \int d^3x\,\psi_f^* H_{int}\psi_i \tag{54}$$

We use a Valkov-type wavefunction[19]:

$$\psi_i(\mathbf{k},\mathbf{r},t) = u_i(\mathbf{k},\mathbf{r})\exp\left[i\mathbf{k}\cdot\mathbf{r} - \frac{i}{\hbar}\int E_i(\tau)d\tau\right] \tag{55}$$

where i is used to designate a band with E_i given by[17]:

$$\begin{aligned} E_c &= E_g + \frac{\hbar^2k^2}{2m_c} - \frac{e\hbar}{m_c c}\mathbf{k}\cdot\mathbf{A}(\tau) + \triangle E_{cv} \\ E_v &= \frac{\hbar^2k^2}{2m_v} - \frac{e\hbar}{m_v c}\mathbf{k}\cdot\mathbf{A}(\tau) + \triangle E_{vc} \end{aligned} \tag{56}$$

with $\triangle E_{ij}$ designating the time independent ac Stark shifts. The resulting S-matrix is:

$$\begin{aligned} S = \tfrac{i\pi}{\hbar} \frac{e\hat{\mathbf{n}} \cdot \mathbf{P}_{vc}}{m_o c} \textstyle\sum J_m(\eta_1) J_n(\eta_2) \\ \times [A_{01}\{\delta((m+1)\omega_1 + n\omega_2 + \omega_{vc}) + \delta((m-1)\omega_1 + n\omega_2 + \omega_{vc})\} \\ + A_{02}\{\delta(m\omega_1 + (n+1)\omega_2 + \omega_{vc}) + \delta(m\omega_1 + (n-1)\omega_2 + \omega_{vc})\}] \end{aligned} \tag{57}$$

where

$$\begin{aligned} \mathbf{P}_{vc} &= \tfrac{i}{\hbar} \textstyle\int d^3x u_c^*(\mathbf{k}, \mathbf{r}) \nabla u_v(\mathbf{k}, \mathbf{r}) \\ \hbar\omega_{vc} &= E_g - \triangle E_{vc} + \triangle E_{cv} + \tfrac{\hbar^2 k^2}{2m_{cv}} \\ \frac{1}{m_{cv}} &= \frac{1}{m_c} - \frac{1}{m_v} \\ \eta_i &= \frac{eA_{oi}\mathbf{k} \cdot \hat{\mathbf{n}}}{m_{vc} c \omega_j} \end{aligned} \tag{58}$$

At this point, we consider the different processes resulting in two photon absorption. For simplicity, a two parabolic band model with $m_v = -m_c$ with a spin degeneracy of 2 for each band is used for the calculations. First, for degenerate two photon absorption we have, $A_{02} = 0$, $m = -1$, and $n = 0$. Ignoring changes due to optical stark effect (assuming $J_n(x) \simeq x^n/2^n n!$), the change in the transition rate due to this process is[17]:

$$\begin{aligned} \triangle W &= \textstyle\sum \int \frac{d^3k}{(2\pi)^3} \left[\frac{\pi e^2 A_{01}^2}{2m_o m_{cv} c^2 \omega_1} \right]^2 |\hat{\mathbf{n}} \cdot \mathbf{P}|^2 \\ &\times |\hat{\mathbf{n}} \cdot \mathbf{k}|^2 \frac{1}{2\pi\hbar} \delta \left(E_g + \frac{\hbar^2 k^2}{2m_{vc}} - 2\hbar\omega_1 \right) \\ &= \frac{2^4\pi}{5} \frac{e^4}{n_1^2 c^2} \frac{E_g}{2\sqrt{m_c}} \frac{I_1^2}{(\hbar\omega)^6} (2\hbar\omega_1 - E_g)^{3/2} \end{aligned} \tag{59}$$

In the above we have assumed that $\mathbf{P}_{vc}$ is parallel to $\mathbf{k}$ resulting in factor of $1/5$ for the angular integration and used $I_1 = n_1\omega_1^2/8\pi c$ and $|\mathbf{P}_{vc}|^2 / m_o^2 \approx E_g/2m_c$. Using $\triangle W = \beta I^2/2\hbar\omega$, we get

$$\beta(\omega) = 2K \frac{\sqrt{E_p}}{n_1^2 E_g} F_2 \left(\frac{\hbar\omega}{E_g} \right) \tag{60}$$

where

TABLE II Functional forms of F(x)

Contribution	$F_2^i(x_1; x_2)$
Two-Photon Absorption	$\frac{(x_1 + x_2 - 1)^{3/2}}{2^7 x_1 x_2^2} \left(\frac{1}{x_1} + \frac{1}{x_2}\right)^2$
Raman	$\frac{(x_1 - x_2 - 1)^{3/2}}{2^7 x_1 x_2^2} \left(\frac{1}{x_1} - \frac{1}{x_2}\right)^2$
Linear Stark	$-\frac{(x_1 - 1)^{3/2}}{2^6 x_1 x_2^2} \frac{1}{x_2^2}$
Quadratic Stark	$-\frac{1}{2^{10} x_1 x_2^2 (x_1 - 1)^{1/2}} \left[\frac{1}{x_1 - x_2} + \frac{1}{x_1 + x_2}\right]$

$$\begin{aligned} F_2(x) &= \frac{(2x-1)^{3/2}}{2(2x)^5} \\ E_p &= \frac{m_o}{m_c} E_g \simeq 21 \text{ ev} \end{aligned} \tag{61}$$

$$K = \frac{2^9 \pi}{5} \frac{e^4}{\sqrt{m_o} c^2}$$

resulting in β with units of cm/GW. The scaling parameter for K deviates with different approaches. A value of 3100 has been shown to yield the best fit to the empirical data obtained[17]. The above solution is a special case of the nondegenerate two photon absorption coefficient with

$$F_2^{TPA} = \frac{(x_1 - x_2 - 1)^{3/2}}{2^7 x_1 x_2^2} \left(\frac{1}{x_1} + \frac{1}{x_2}\right)^2 \tag{62}$$

Other calculations using other methods have resulted in similar expressions with the different value of K. Including other two photon processes of Raman transitions, linear and quadratic Stark effects, we obtain the same expression as Eq. 60 but different $F_2(x)$. Table II is the resulting F_2 expressions taken from ref. [17] for each of the processes. The total two photon absorption coefficient is thus,

$$\beta = 2K \frac{\sqrt{E_p}}{n_1^2 E_g} \left(F_2^{TPA} + F_2^{RAM} + F_2^{LSE} + F_2^{QSE}\right) \tag{63}$$

TABLE III Functional forms of G(x)

Contribution	$G_2(x)$
Two-Photon Absorption	$\frac{1}{(2x)^6}\left[-\frac{3}{8}x^2(1-x)^{-1/2}+3x(1-x)^{1/2} -2(1-x)^{3/2}+2\Theta(1-2x)(1-2x)^{3/2}\right]$
Raman	$\frac{1}{(2x)^6}\left[-\frac{3}{8}x^2(1+x)^{-1/2}-3x(1+x)^{1/2} -2(1+x)^{3/2}+2(1+2x)^{3/2}\right]$
Linear Stark	$\frac{1}{(2x)^6}[2-(1-x)^{3/2}-(1+x)^{3/2}]$
Quadratic Stark	$\frac{1}{2^{10}x^5}\left[(1-x)^{-1/2}-(1+x)^{-1/2} -\frac{x}{2}(1-x)^{-3/2}-\frac{x}{2}(1+x)^{-3/2}\right]$

Having found the frequency dependence of absorption changes $\triangle\alpha = \beta I$ we can determine the corresponding nonlinear refraction coefficient, n_2, via Kramers-Krönig relation[13]:

$$\triangle n(\omega_1;\omega_2;I) = \frac{c}{\pi}\int d\omega' \frac{\triangle\alpha(\omega';\omega_2;I)}{\omega'^2-\omega_1^2} \tag{64}$$

The above is strictly valid if the optical intensity is kept constant[13] but can be used to a good accuracy to determine the Kerr coefficient. In this case we obtain

$$\begin{aligned} n_2 &= 2K\frac{\hbar c^2\sqrt{E_p}}{20\pi n_o E_g^4}G_2\left(\frac{\hbar\omega}{E_g}\right) \\ &= K'\frac{\sqrt{E_p}}{n_o E_g^4}G_2\left(\frac{\hbar\omega}{E_g}\right) \end{aligned} \tag{65}$$

With K' having values in the range of $0.8-1.5\times10^{-8}$. Table III lists the functional forms for $G_2(x)$.

Free Carriers. Upto this point we have neglected any contribution due to free carriers. This, in general is a good approximation for a widegap semiconductors and insulators. Particularly, contributions to the index of refraction due to free carriers are more than 1000 times smaller than those due to bound electrons in these materials. However, variations in the spatial positions of these carriers can result in significant alteration of the behavior of a light in that medium. For example, if carriers are placed in a sinusoidal nature within a sample, an incident light undergoes diffraction as discussed earlier.

To include the contributions due to free carriers, we need merely to replace the complex dielectric constant, $\tilde{\varepsilon}$, with the more general complex dielectric coefficient, $\tilde{\epsilon}$. In doing so, we are introducing the effects of the free carriers through the complex conductivity, $\tilde{\sigma}$. In this case, using Eq. 12

$$\begin{aligned} \sqrt{\varepsilon_R} &\rightarrow \sqrt{\epsilon_R} = \sqrt{\varepsilon_R - 4\pi\sigma_I/\omega} \\ \varepsilon_I &\rightarrow \epsilon_I = \varepsilon_I + 4\pi\sigma_R/\omega \end{aligned} \tag{66}$$

In terms of the index of refraction, n, and absorption coefficient α, we have:

$$\begin{aligned} n &= \sqrt{\epsilon_R} = \sqrt{\varepsilon_R}\sqrt{1 - 4\pi\sigma_I/\omega\varepsilon_R} \\ \alpha &= \frac{\omega\epsilon_I}{c\sqrt{\epsilon_R}} = \frac{\omega}{c\sqrt{\epsilon_R}}(\varepsilon_I + 4\pi\sigma_R/\omega) \end{aligned} \tag{67}$$

Using the fact that the changes in the index of refraction due to free carriers is much smaller than the background index, n, the above reduces to

$$\begin{aligned} n &= n_o - \frac{2\pi\sigma_I}{\omega n_o} \\ \alpha &= \alpha_o + \frac{4\pi\sigma_R}{n_o c} \end{aligned} \tag{68}$$

where n_o, and α_o are given by Eq. 23. The above equation states that the additional free carriers *decrease* the index of refraction. We can use the Drude-Lorentz model for conductivity by ignoring the ω_o term in Eq. 1 and using $J = \sigma E$, to get:

$$\tilde{\sigma} = \frac{N f_o e^2}{m(\gamma - i\omega)} = \frac{e^2 N_{free} f'}{m(\gamma - i\omega)} \tag{69}$$

where for sake of completeness, we have included an oscillator strength, f'. Defining $\tau = 1/\gamma$, we have,

$$\tilde{\sigma} = \sigma_R + i\sigma_I = \frac{e^2 N_{free} f''}{m}\left[\frac{\tau}{1+\omega^2\tau^2} + i\frac{\omega\tau^2}{1+\omega^2\tau^2}\right] \tag{70}$$

Combining Eq. 68 and Eq. 70, in the high frequency limit, $\omega\tau \gg 1$, we have

$$\begin{aligned}\Delta n &= -\frac{2\pi e^2 N_{free} f'}{nm\omega^2} = -\gamma N_{free} \\ \Delta\alpha &= \frac{4\pi e^2 N_{free} f'\tau}{ncm\omega^2} = \kappa N_{free}\end{aligned} \tag{71}$$

The above is a simplified version of the results obtained from a band filling model. In this model, the change in the real part of the dielectric function is calculated directly. Such a quantum mechanical calculation yields[20]

$$\Delta n = -\frac{2\pi e^2 N_{free}}{nm\omega^2} \frac{E_{gap}^2}{E_{gap}^2 - (\hbar\omega)^2} \tag{72}$$

This theory has all the same features as the classical analog with $f' = E_{gap}^2/[E_{gap}^2 - (\hbar\omega)^2]$. This difference is due to the fact that in the classical case we set $\omega_o = 0$ which ignores any coupling to higher lying bands.

<u>Photorefractive effect</u>. In addition to changes brought about directly, free carriers can also contribute to changes in the refractive index through interaction with ionized impurities or oppositely charge carriers. Such interaction is only possible in electro-optic crystals (no center of inversion) and is known as the photorefractive effect. This effect is most commonly associated with laser induced grating experiments and as such we focus on its behavior in these experiments.

Let us assume that two σ-polarized, plane wave beams propagating in the z-direction are crossed at an angle, θ, in a crystal . The interference of the beams results in an intensity distribution given by:

$$\begin{aligned}I_{tot} &= I_A + I_B + 2\sqrt{I_A I_B}\cos(\overrightarrow{q} \cdot \overrightarrow{r}) \\ &= 2I\{1 + \cos(2k_x x)\}\end{aligned} \tag{73}$$

where

$$\overrightarrow{q} \cdot \overrightarrow{r} = (\overrightarrow{k}_A - \overrightarrow{k}_B) \cdot \overrightarrow{r} = 2k_x \tag{74}$$

with k_i being the wave vector for the i beam. We have also assumed that they have equal wave vector magnitudes, k and intensity, I. Absorption of light through single and/or two photons results in generation of free carriers with a spatial profile of I_{tot}, i.e.

$$N = 2N_o\{1 + \cos(2k_x x)\} \tag{75}$$

The generated carriers migrate from the highly concentrated region of the peak to the less concentrated valleys of the light induced grating. This motion may arise due to diffusion, drift, photovoltae or a combination of these process[11]. To get a better intuitive understanding we assume that the carrier motion is dominated by electrons.

Immediately after the generation, each region is still neutral. Once the electrons initiate their motion from the bright regions to the dark regions, a charge distribution builds up. In particular, the bright regions lose electrons and become slightly positive (leftover holes and ionized donors) and the dark regions become slightly negative (excess electrons). This leads to a charge distribution given by

$$\rho_{sc} = \rho_o \cos(2k_x x) \tag{76}$$

Using Gauss's law $\nabla \cdot E = 4\pi\rho/\varepsilon$ we get an electric field of the form

$$E_{sc} = E_o \sin(2k_x x) \tag{77}$$

Figure 8, from ref. [21], summarizes the buildup of a space-charge field. This field can now interact with the material through the linear (or quadratic electro-optic) coefficients to produce an index change of the form:

$$\begin{aligned} \triangle n &= \frac{1}{2} n_o^3 r_{eff} E_{sc} \\ &= \triangle n_o \sin(2k_x x) \end{aligned} \tag{78}$$

The periodicity of this index change is $\pi/2$ out of phase from the instantaneous change arising from the generation of the free carriers. A probe beam incident on such a grating diffracts in the Bragg direction as discussed before.

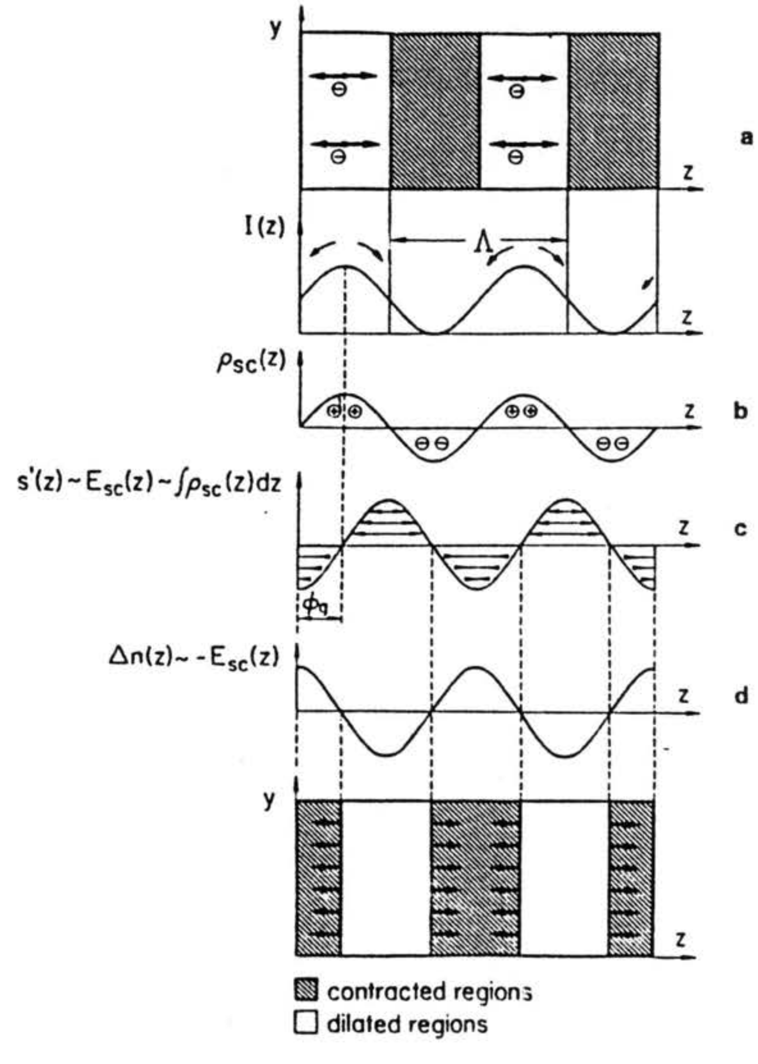

Figure 8. Schematic of the buildup of a space charge field from an laser induced grating.

Other Mechanisms. In terms of the basic Lorentz model, any changes in the electronic cloud of atoms results in a change in the polarizability and subsequently, the refractive index. There are several mechanism that may induce this change. Below we consider a few of them relevant to this work.

In materials with dopants, transitions within a dopant can lead to significant index changes[22]. In terms of our model, this means that the responsible electron is in an orbital which may have a significantly different "cloud" from the ground state. The significance is determined by the host as well as the dopant[22]. In this case the susceptibility is given by:

$$\chi = \chi_o^{(1)} + \{\chi_1^{(1)} - \chi_o^{(1)}\}N_1/N + \cdots \tag{79}$$

where, χ_o and χ_1 are the susceptibility of the material with the dopants in the ground and excited states, respectively. The population of the excited ions, N_1, is directly related to the intensity of the exciting beam and is, therefore, quadratic in the field amplitude. This means that changes due to population changes are third order susceptibility changes. A detailed analysis of the derivation of this contribution and typical magnitude for certain ions is found in ref. [22], [9].

Alternatively, it is possible to alter the cloud by introduction of an electric field or a temperature change. Here, the interaction of the atomic orbitals with the surrounding atoms is modified. This, inturn, modifies the index of refraction. In terms of the macroscopic quantities, density and temperature, we can represent this as:

$$\triangle n = \left(\frac{\partial n}{\partial \rho}\right)_T \triangle\rho + \left(\frac{\partial n}{\partial T}\right)_\rho \triangle T \tag{80}$$

Where the origin of the changes is irrelevant. Changes in the density occur in the presence of an electric field, a structural change or temperature changes. Changes in temperature are a result of heating, either directly or indirectly such as optical absorption.

An applied field alters the electronic cloud of a material and thereby changing the macroscopic density of the medium. Therefore, the first term in the above equation is the responsible term for index changes. This effect is known as electrostriction and for a CW beam is represented as [9]

$$\triangle\rho(E) = \frac{\gamma}{2\pi v^2}|E(\omega)|^2 \tag{81}$$

In the above γ is the Electrostrictive coefficient and v is the velocity of sound. We have also assumed that the responsible field is the optical field itself.

In the presence of absorption additional changes are present due to an increase in the local temperature. Ignoring the effects of diffusion, the temperature change is given by:

$$\triangle T(r) \simeq \rho c \int I(r,t)dt \tag{82}$$

where, ρ, c, and I are the density, heat capacity and the input intensity respectively. This change in the temperature results in a change in the index by (i) changing the density of the material and (ii) changing the polarizability of the atoms. Assuming that density is a function of temperature only, the total change in the refractive index in the presence of absorption is[23]:

$$\begin{aligned} \triangle n(\rho,T) &= \left(\frac{\partial n}{\partial \rho}\right)_T \triangle\rho(T) + \left(\frac{\partial n}{\partial T}\right)_\rho \triangle T \\ &= \left(\frac{\partial n}{\partial \rho}\right)_T \left(\frac{\partial \rho}{\partial T}\right) \triangle T + \left(\frac{\partial n}{\partial T}\right)_\rho \triangle T \end{aligned} \tag{83}$$

The two terms can be combined to give:

$$\triangle n(\rho,T) = \frac{dn}{dT}\triangle T \tag{84}$$

In the above dn/dT is known as the thermo-optic coefficient. To obtain a quantitative measure of this coefficient we use the Lorentz-Lorenz model for the macroscopic index of refraction;

$$\frac{n^2-1}{n^2+2} = \frac{4\pi}{3}\frac{N\alpha'}{V} \tag{85}$$

Where N, α', and V are the number of atoms, polarizability of each atom and volume respectively. Using

$$\frac{\partial \rho}{\partial T} = \beta \rho$$

and

$$\frac{\partial \alpha'}{\partial T} = \Phi \alpha'$$

we get:

$$\frac{dn}{dT} = -\frac{(n^2-1)(n^2+2)}{6n}(\beta - \Phi) \tag{86}$$

Note that changes in the index arising from an increase in the density are negative while those due to polarizability are positive. The contribution of each term depends on the material used and the time scales involved. In general, the effects due to density changes are slower and smaller than temperature changes in polarizability. However it is possible to select materials with zero or negative thermo-optic coefficients[23].

Part B

MATERIALS FOR FAST SWITCHES

CHAPTER III

DILUTED MAGNETIC SEMICONDUCTORS

Introduction

Dilute magnetic semiconductors (DMS) have been the subject of numerous investigations in the recent years. Most popular are $A^{II}MnB^{VI}$, where Mn^{2+} ions are embedded in a $II - VI$ semiconductor host. Structurally, in $A^{II}B^{VI}$ semiconductors, the group II cations (A) have 2 valence electrons and the group VI anions (B) have 6 valence electrons in the outer shells. It is the formation of bond between these atoms which gives rise to the semiconducting behavior of the host material. From an ionic bonding approach bonds are formed by transfer of the 2 valence electrons of the cation to the electron deficient orbital of the anion. Therefore, in the band formation view point, the valence band extremum is due to the filled outer shell of the anions. Similarly the minimum of the conduction band is due to the empty outer shell of the cations. For example in CdTe the valence band is composed of the p-type orbitals of Te and the conduction band, the s-type orbitals of Cd. From a molecular orbital approach, the 2 valence electrons of the cations and the 6 valence electrons of the anions hybridize to form a pair of bonding and antibonding s-p^3 orbitals [24]. The overlap of the bonding orbitals results in the p-type valence and the overlap of antibonding orbitals results in the s-type conduction bands.

The s-p^3 orbital formation means that the cation and the anion are bonded tetrahedrally, i.e. each having 4 nearest neighbors in a tetrahedral coordination leading to the zincblend and wurtzite structures found in $A^{II}B^{VI}$ semiconductors. Recall that zincblend consists of two interpenetrating fcc sublattices shifted along the (111) axis and wurtzite consists of two interpenetrating hcp sublattices shifted along (001) axis [10].

By far the most popular magnetic ions in DMS is Mn^{2+} ions. Apart from the fact that Mn^{2+} ions have a high spin angular momentum (S=5/2) and are electrically neutral in the $II-VI$ host, $A^{II}MnB^{VI}$ with high concentration of Mn can be grown without significant alteration of the crystallographic nature of the host [25]. This is a unique property most commonly associated with the presence of filled d-orbitals in Mn ions. The high solubility leads to several interesting physical properties.

First, the addition of Mn results in alteration of the lattice parameter and the band gap of the host in a continuous way. This allows the customization of the semiconducting and optical properties of these materials where needed such as in quantum wells.

Second, depending on Mn concentration, DMS can exhibit paramagnetic, antiferromagnetic and spin glass behaviors in the same host. This allows the study of the effects of spin-spin correlation and the role of super exchange on the magnetic properties observed.

Third, interactions among the Mn ions and the conduction band electrons lead to effects which are unique to the DMS. These include giant Faraday rotation, giant negative magnetoresistance and large Zeeman splittings. These are referred to as sp-d exchange interactions since it is believed that they arise from interaction between the Mn d-electrons and the sp band.

Although numerous investigations have been performed on the nonlinear optical properties of $II-VI$ semiconductors, a relatively few experiments on the nonlinear optical properties of DMS have been reported. With this in mind, experiments were performed to determine the nonlinear optical and carrier dynamics of $Cd_{1-x}Mn_xTe$ and $Cd_{1-x}Mn_xSe$ samples with several Mn concentrations.

TABLE IV Physical parameters of the DMS used

Sample	x	Bandgap (eV)	Thickness (mm)
CdSe	0.0	1.7	0.7
	0.1	1.8	0.7
	0.2	1.9	0.7
+In	0.3	2.0	0.7
	0.4	2.1	0.7
CdTe	0.0	1.5	0.9
	0.1	1.6	1.0
	0.25	1.8	0.7
	0.45	2.0	2.4

Nonlinear Optical Properties

The nonlinear optical properties of semiconductors can be categorized as those arising from the bound electrons and free carriers. The nonlinearities due to the bound electrons are instantaneous and follow the temporal shape of the pulse. In the case of the third order susceptibility tensor, these result in the two photon absorption, β, and the bound electron nonlinear refraction, n_2, coefficients. In the last chapter we should that these parameters are band gap dependant and have been estimated for a variety of materials. Nonlinearities due to free carriers, however, have been less investigated. We shall focus on the effects of free carriers on the optical nonlinearities. To utilize the bulk properties of the material, two photon absorption is used to generate the free carriers. Therefore, it is necessary to determine this coefficient in order to estimate the number of generated carriers. The experiments were designed for simultaneous determination of these properties.

Experimental Setup

Table IV lists the characteristics of the CdMnSe and CdMnTe samples used for the experiment. The CdMnSe samples were cut and positioned with their c-axis parallel to the polarization of the incident light. In the CdMnTe samples the (111) crystal direction was set parallel to the propagation direction of the incident beams.

For this investigation we used a mode-locked, Q-switched, Nd:YAG laser operating at 1.06 μm with a FWHM of 27 ps. Since photon energies of the laser are less than the band gap of the DMS studied, free carrier generation takes place primarily via two photon absorption (TPA). The generated carriers, then, modulate the absorption coefficient and index of refraction of the material. In particular, if the excitation pulse has a Gaussian intensity profile, the spatial profile of the generated electrons would be radial causing the material to behave as an absorptive lens. The absorptive nature of the material is due to two photon absorption of bound electron and the subsequent single photon absorption of the generated carriers. The effects due to free carriers persist while they remain in the conduction band. Therefore, it is possible to isolate their effects by introducing of a weak probe beam delayed long enough to insure no interaction with the pump beam yet much shorter than the carrier lifetime to avoid errors due to their recombination. Changes in the post sample spatial profile of a delayed probe beam are, then, solely dictated by the free carriers. If the number of these carriers were known, it would be a relatively simple task to determine the changes induced by them.

Figure 9 shows the experimental setup used to study the third order nonlinearities in our samples. The probe beam is delayed 100 ps from the pump beam to insure that there are no interactions between the beams. Both beams are passed through a $1m$ focal length lens and have the same beam radius of $590\mu m$ at the front surface of the sample. Each sample was placed 29cm behind the focal plane of the lens. The samples were 'thin' compared to the Rayleigh range of the beams ($\sim$30 times smaller) to insure applicability of the thin medium formalism[26,27]. The energy of the pump beam was varied by a waveplate-polarizer combination and that of the probe was kept fixed at a level where no self-induced optical nonlinearities were measurable. The apertures placed in front of the detectors are to

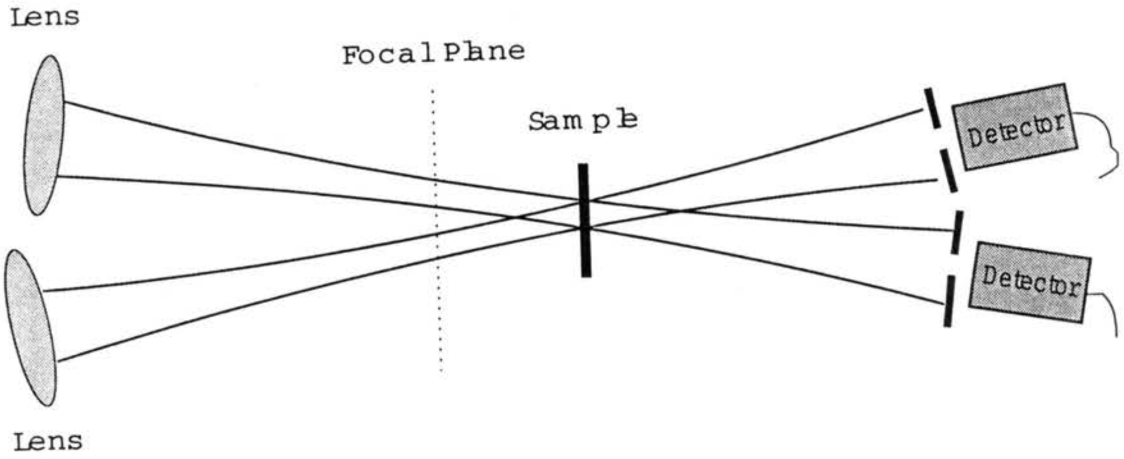

Figure 9. Experimental setup for measuring the nonlinear optical properties.

monitor the total and the on-axis transmission of each beam. The detected energy at each meter was stored in a computer as a function of the input energy of the pump beam.

Theoretical

We can use the formalisms developed in the previous chapter to put the above in a more quantitative bases. Using Eqs. 51 and 71 , the amplitude, I_1, and the phase changes, ϕ_1, of the post sample incident pump beam are given by:

$$\frac{dI_1}{dz} = -\alpha I_1 - \beta I_1^2 - \sigma N I_1 \tag{87}$$

$$\frac{d\phi_1}{dz} = k(n_2 I_1 + \sigma_r N) \tag{88}$$

where for the laser photon energies ($\hbar\omega < E_{gap}$) the carrier concentration, N, is given by:

$$\frac{dN}{dt} = \beta \frac{I_1^2}{2\hbar\omega} \tag{89}$$

Here, k is the wave vector of the incident pump beam, α is the absorption coefficient of the material, σ is the free carrier absorption cross section (FCA), and σ_r is the nonlinear refraction coefficient of the free electrons (FCN). In Eq. 89 any recombination of the carriers is neglected since the lifetime of the carriers are much greater than the 27 ps pulsewidth of the laser. In the above we have also ignored any losses due to second harmonic generation (SHG) of the pump beam. This is valid since phase matching condition is not satisfied for our crystal orientation. Furthermore, second harmonic of the pump beam has photon energy greater than the band gap and is, therefore, absorbed by the valence electrons. This SHG followed by single photon absorption leads to a small correction in the value of the two photon absorption coefficient and is ignored here. Separate experiments investigating the SHG signal emerging from the back surface of these materials show that the above assumption is valid.

A similar set of equations can be used for the delayed probe beam, I_2. However, any changes of the probe beam amplitude and phase are a result of the pump beam generated free carriers only. In other words:

$$\frac{dI_2}{dz} = -\alpha I_2 - \sigma N I_2 \tag{90}$$

$$\frac{d\phi_2}{dz} = k\sigma_r N \tag{91}$$

But the number of generated carriers is still determined by the pump beam intensity:

$$\frac{dN}{dt} = \beta \frac{I_1^2}{2\hbar\omega} \tag{92}$$

The field at any plane past the sample can, then, be calculated by a zeroth order Hankel transform of the field at the exit plane. The above equations were solved numerically and the field at the aperture was determined for a number of input pump beam intensities.

Results and Discussion

Two photon and free carrier absorption.

To determine the values for two photon and free carrier absorption the *total* energy of the pump and the probe were measured versus their energies incident on the sample. Experimentally, this means that the aperture in front of the detector was fully open. In this case, all of the light from the two beams is collected and changes in the phase front resulting in the lensing behavior of the material do not play a role. The transmission coefficients, hence, are solely determined by the two photon and free carrier absorption coefficients. For the probe beam, these changes are a result of the free carrier absorption only. Mathematically, we need to solve Eqs. 87 89 and 90 to determine the transmittivity of the samples. In these equations the two unknowns are β and σ. Since we are employing two separate beams, it should be possible to determine their magnitude exactly.

Figure 10 (a) and (b) shows the transmission coefficients of the pump and probe beams obtained in a fully open aperture experiment performed on CdTe. The lines in the graphs correspond normalized transmission of the pump and probe beams for various values of β and σ. While it is apparent that a "fit" to the pump beam transmission can be obtained for a number of different β and σ combinations, use of both graphs uniquely determines each coefficient. This procedure was repeated for all the samples.

Figure 11 (a) shows the magnitude of two photon absorption coefficient in $Cd_{1-x}Mn_xSe$ and $Cd_{1-x}Mn_xTe$ for different x values. Both hosts exhibit similar features, a decrease in the TPA coeff. with an increase in the Mn concentration, x. As stated earlier, an increase in x results in an increase in the band gap. Therefore, the figure shows a decrease in the TPA coeff. with an increase in the band gap. This is to be expected from the discussions in the origin of optical nonlinearities section. Figure 11 (b) shows the magnitude of the free carrier absorption for

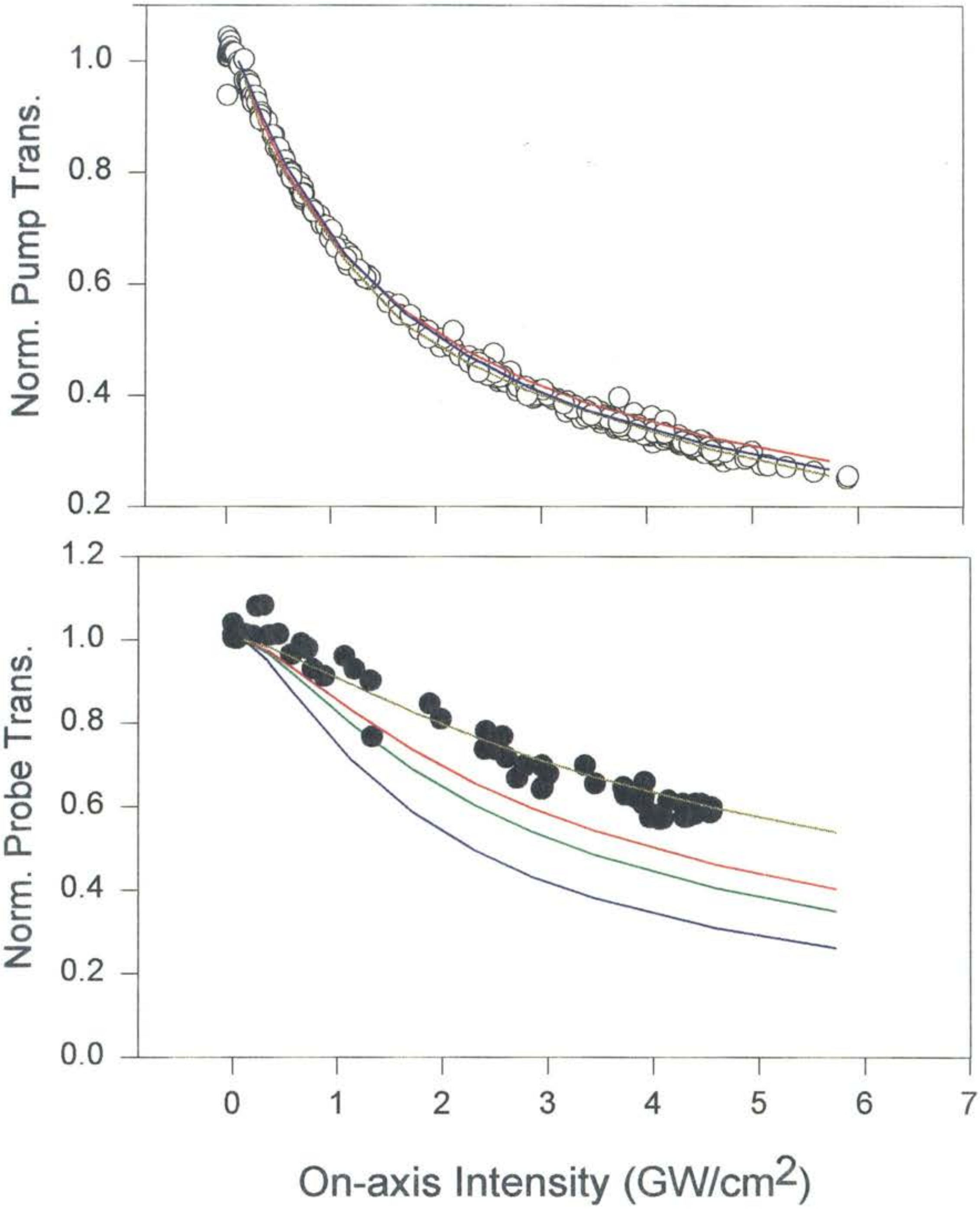

Figure 10. Results of the open aperture experiment on CdTe for (a) Pump beam and (b) Probe beam. The circles are the data points and the lines are the solutions of Eqs. 87, 89 and 90 at the detectors.

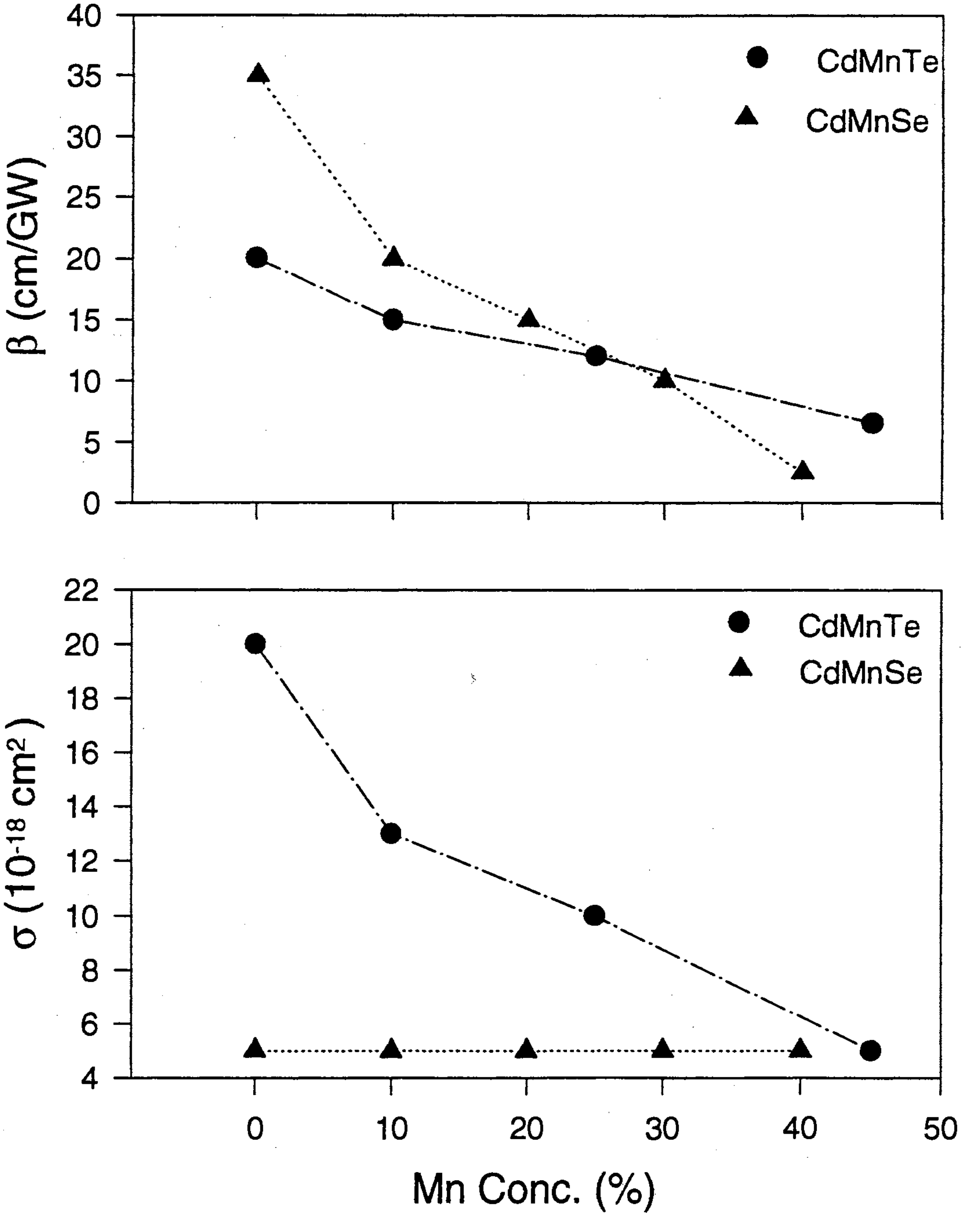

Figure 11. Parameters obtained for the (a) two photon and (b) free carrier absorption coefficients for different Mn concentrations.

various Mn concentrations. Here, we see different behavior from the two materials. In CdMnSe, free carrier absorption cross-section remains constant for all values of x. In CdMnTe, however, the cross-section decreases with an increase in the Mn concentration. The origin of this is not understood and warrants further investigation.

With these parameters determined, we can used Eq. 89 to determine the number of carriers generated by the pump beam. This is an important parameter in determination of the free carrier absorption cross-section or nonlinear refractive index changes. Figure 12 (a) and (b) are the total number of carrier per unit length generated by the pump beam. For CdMnSe the number of generate carriers decrease with increase in Mn concentration. This is to be expected since the FCA coefficient in this material remains constant while the TPA coefficient decrease with addition of Mn. For the CdMnTe, however, number of free carriers in pure CdTe is the same as that with 10% Mn. The number increases for the 20% Mn conc. before decreasing for the 45% concentration. The reason for this behavior is associated with the non-constant behavior of the FCA cross-section. Since both the TPA and FCA are decreasing with increase in Mn concentration, the total number of carriers generated depends on both coefficients. It is, therefore, possible for a higher Mn concentrated sample with smaller TPA coefficient to have greater number of free carriers.

Nonlinear refraction. Having determined the TPA and FCA coefficients we focus on the nonlinear refraction of the samples. Nonlinearities can arise from bound and free electrons. In the presence of free carriers, changes in the refractive index are dominated by the electrons. This means omission of the n_2 terms in the phase changes described earlier. Including the phase change equations, there are three parameters to be considered; β, σ, and σ_r. The first two were determined earlier, so all that is left is the free carrier nonlinear refraction (FCN) coefficient, σ_r. This terms causes the phase of the wave front to experience a change proportional to the number of generated carriers. Since the generation takes place via two

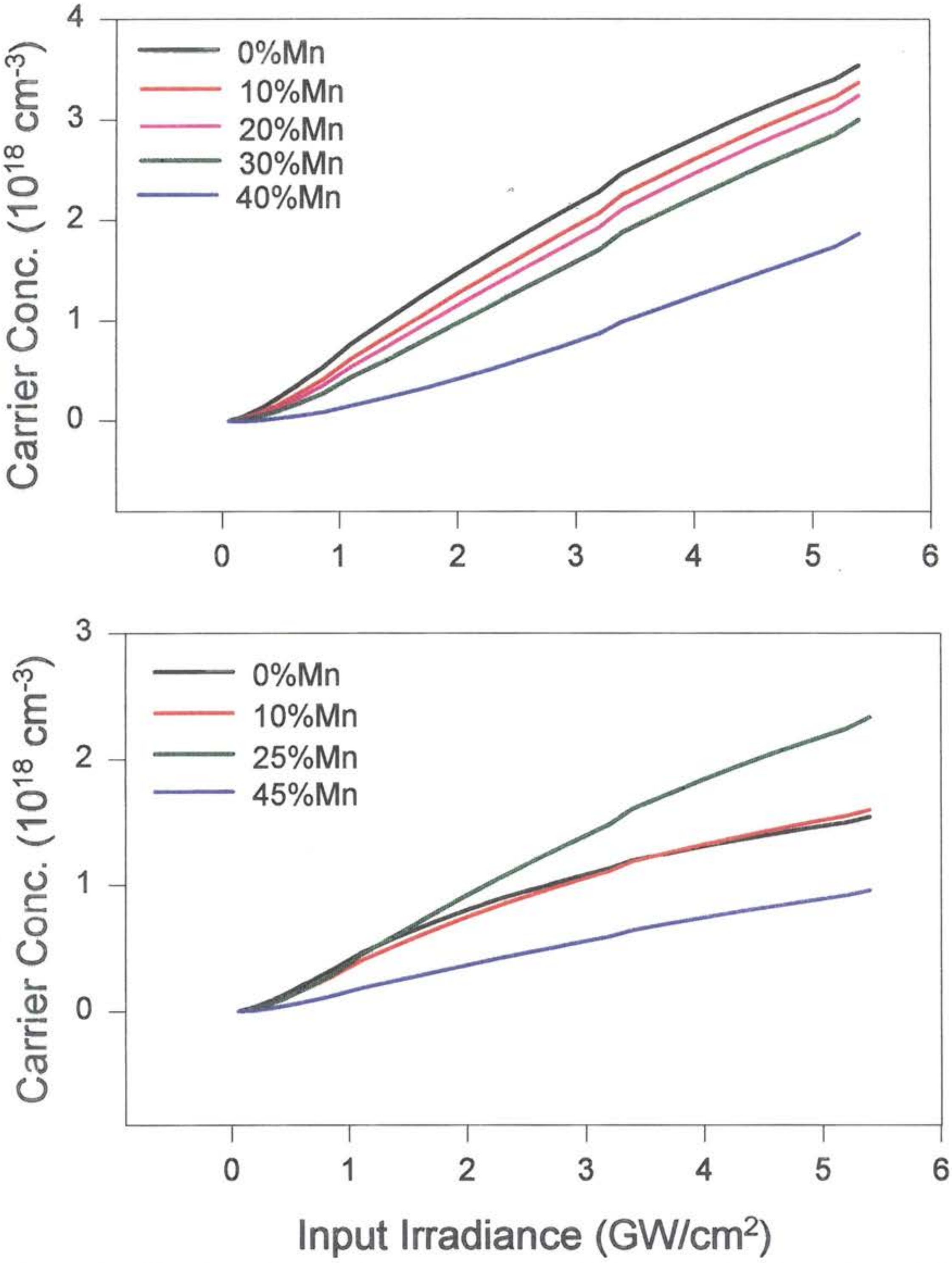

Figure 12. Number of generated carriers per unit length using Eq. 89 for (a) CdMnSe and (b) CdMnTe.

photon absorption of the pump beam, the phase changes have a radial distribution, $\phi(r)$. This radial phase change is similar to that experienced by a beam passing through a lens. Therefore, the FCN can be viewed as inducing a lensing behavior in the sample. In our experiment, this means that the radius of the beam at the detector changes with an increase in the pump beam generated free carrier concentration. In other words, the on-axis intensity of the beams would be different in the presence of material lensing from its value where no lensing is present. We can determine the on-axis intensity by monitoring the energy of the transmitted beam through a small diameter aperture placed in front of the detectors.

If the sample behaves as a negative lens, the on axis intensity shows a decrease greater than a purely absorptive sample. Figure 13 shows the normalized

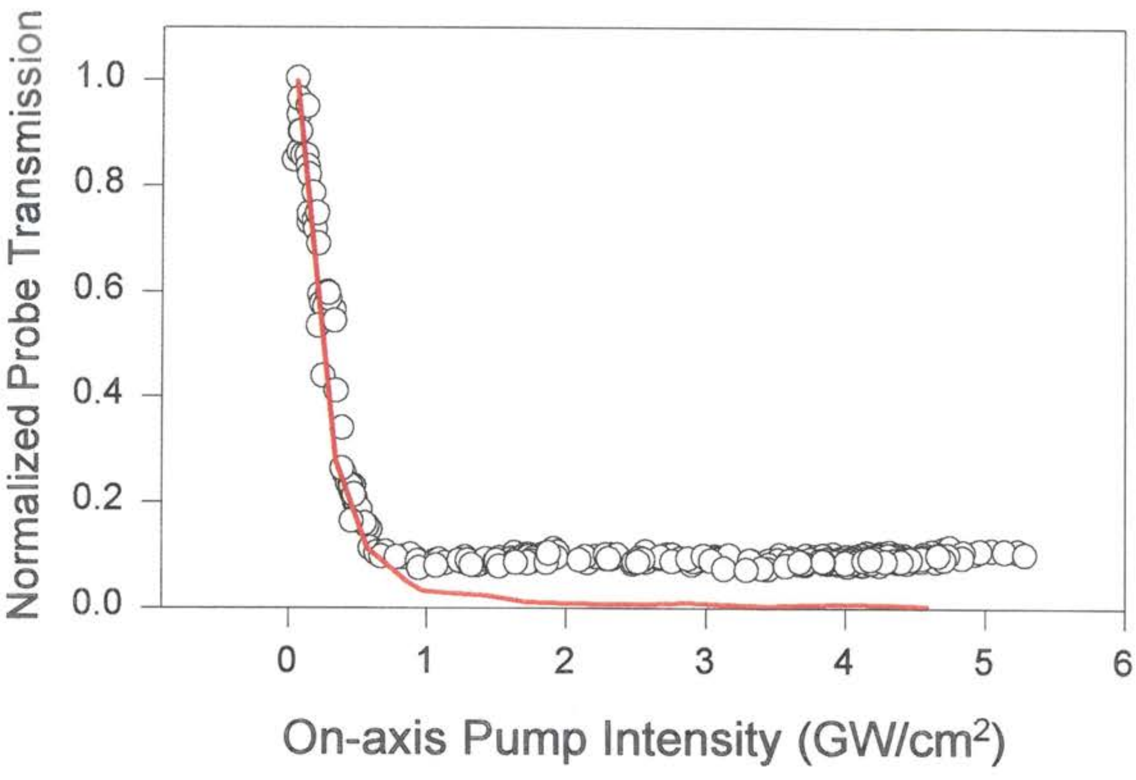

Figure 13. Results of the closed aperture experiment on CdTe for the probe beam. The fit was obtained using Eqs. 90, 91 and 92.

transmission coefficient of the probe beam obtained in a small aperture experiment performed on CdTe. The solid line is the best fit using the old values of β and σ found earlier and σ_r as an adjustable parameter. We observed a decrease in probe beam transmittivity followed by a sharp saturation at higher pump beam intensities. Comparing the probe transmissions in figures 10 and 13 , we see that it decreases more rapidly in the small aperture experiment than in the case of an open aperture experiment. This suggests that the free carriers induced lensing behaves as a negative lens, as expected from the discussion in chapter 2. The sharp saturation in the transmission coefficient, however, could not be fitted or described by Eq. 90 - 92. In particular, a fit could only be obtained if the value of σ_r were to decrease with an increase in the pump beam energy or, in other words with carrier concentration.

In the theories considered so far we had neglected nonlinearities in the free carrier concentration. In trying to keep most of our previous features, we look at concentration dependence of each factor in the FCN coefficient. From Eq. 72

$$\sigma_r = -\frac{2\pi e^2}{n_o \omega^2 m^*} \frac{E_g^2}{E_g^2 - (\hbar\omega)^2} \tag{93}$$

two factors to be considered are E_g and m^*. In the first case we see that an increase in the number of carriers increases the band gap by blocking the possible transition to the bottom of the conduction band. Actually, this band filling model was used to determine the above expression. So This factor is accounted for in the theory. The other factor is the effective mass at the bottom of the band, m^*. At high electron concentrations, states higher than the bottom of the conduction band are occupied. It has been shown that the effective mass of the electrons has an energy dependence given by[28]:

$$m^* = m_o^*(1 + 2\frac{E - E_c}{E_{gap}}) \tag{94}$$

with $E - E_c \approx E_f$, where E_f is the Fermi energy. When carrier concentrations exceed a critical value, N_c, the quasi-Fermi level falls within the conduction band and thus the effective mass of the carriers differs from the dilute case. In general, the location of the Fermi level with respect to the bottom of the band is dictated by the Fermi integral [29] but for our case it can be approximated by $E_f \approx a(\ln(N/N_c))^2$. This means that the effective mass of electrons are given by:

$$m^* = m_o^*(1 + b(\ln(N/N_c))^2) \tag{95}$$

which implies that[30]:

$$\sigma_r = \left\{ \begin{array}{ll} \sigma_{ro} & for\ N < N_c \\ \dfrac{\sigma_{ro}}{1 + b(\ln(N/N_c))^2} & for\ N \geq N_c \end{array} \right\} \tag{96}$$

So, the slope of the transmission coefficient at low pump beam intensities (for $N < N_c$) is dictated by σ_{ro} and the saturation level by b and N_c values.

The calculations were redone with this new FCN coefficient. Figure 14 shows

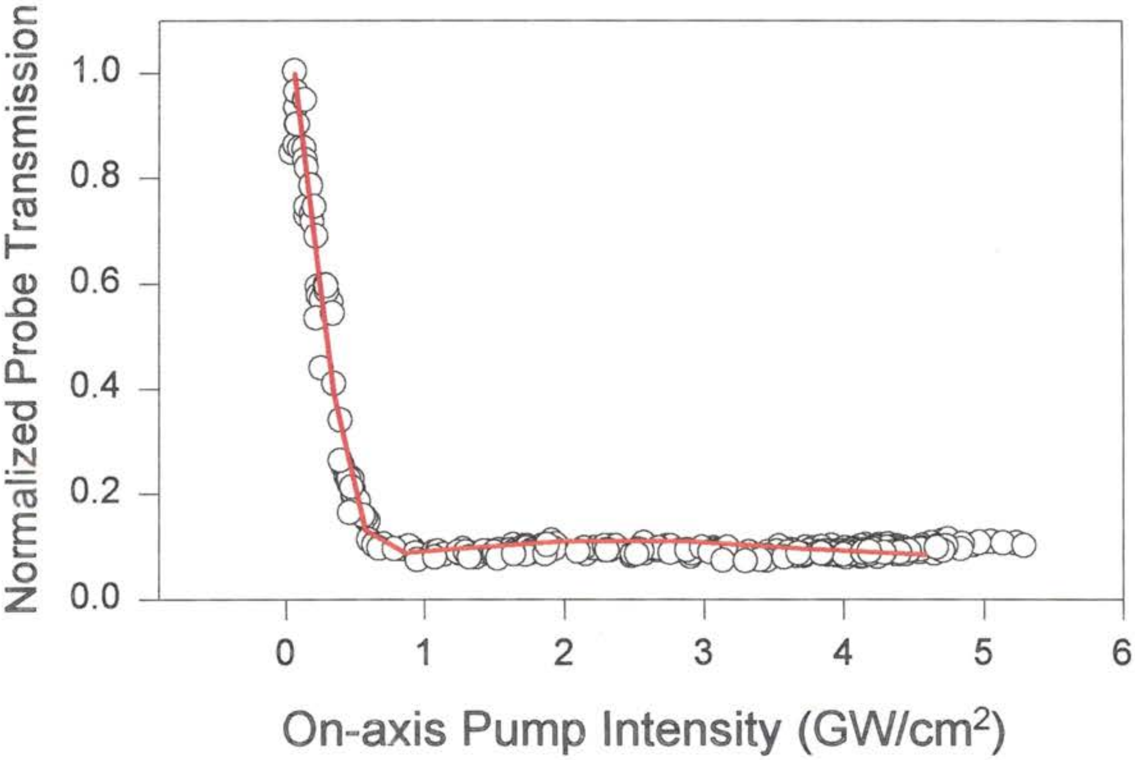

Figure 14. Results of the closed aperture experiment on CdTe for the probe beam. The fit was obtained using Eq. 96 for σ_r.

the result of re-fitting the CdTe results using the above equation with b and N_c as adjustable parameters. The 0.3 and $5\times10^{17}(cm^{-3})$ values used for these parameters are typical values expected for this material.

This was done for all the samples. Figure 15 shows the $|\sigma_{ro}|$ values obtained for different Mn concentrations. We see that for both hosts an increase in concentration results in a decrease in σ_{ro}. Again this is as predicted by the theory presented earlier since a decrease in FCN is to be expected with an increase in E_g. Table V lists the values used for b and N_c for best fits. The values for N_c are $\sim 10^{17}$ and for b are $0.2-0.8$. These are material dependent but have the correct order of magnitude expected from these parameters.

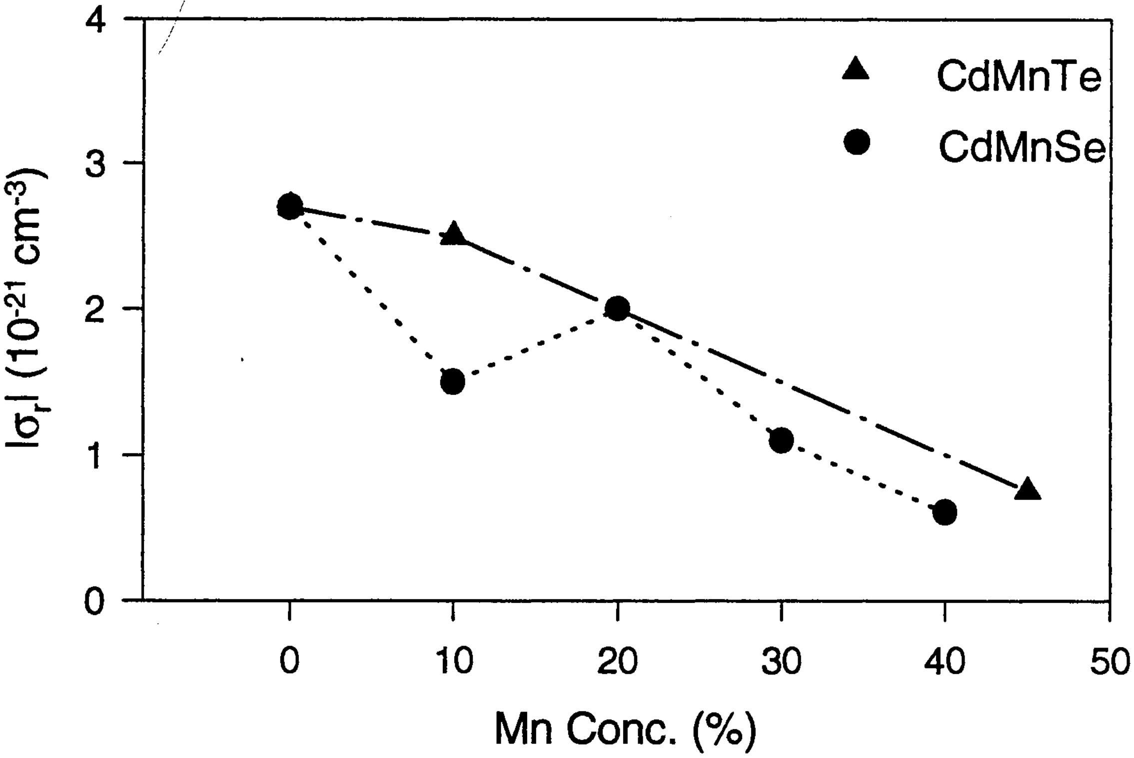

Figure 15. Magnitude of $|\sigma_{ro}|$ as a function of Mn concentration.

In principle, all the relevant parameters have been found. We have an additional set of data, namely the pump beam transmission for small aperture experiment. We can use this as a test for the values found. Figure 16 is the small aperture transmission of the pump and the theoretical prediction using the values

TABLE V Values of b and N_c used for the fit

Sample	x	b coeff.	N_c ($10^{17}cm^{-3}$)
CdSe	0.0	0.3	3.5
	0.1	0.35	6.0
	0.2	0.35	6.0
+In	0.3	0.52	8.0
	0.4	0.3	2.0
CdTe	0.0	0.8	5.0
	0.1	0.6	3.0
	0.45	0.2	1.0

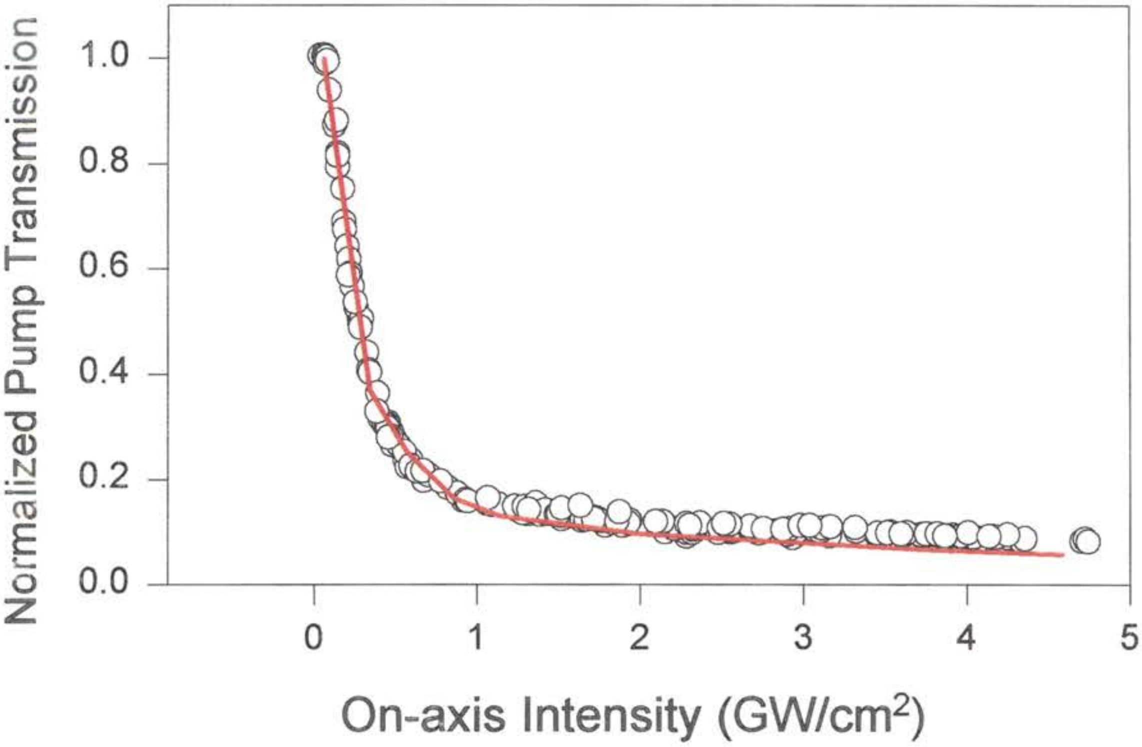

Figure 16. Results of the closed aperture experiment on CdTe for the pump beam. The line is from the parameters obtained from the other data set with no fitting parameters.

determined before. We see an excellent agreement between the data and the fit with *no* adjustable parameters. Similar results were obtained for all samples. A small deviation from the data is observed at higher pump intensities. This corresponds to uncertainties in the b and N_c values. Since the saturation in the small aperture transmission is dependant on two coefficients, and we used probe beam results as the bases for analysis only, more than one set of fitting parameters are possible. Using both pump and probe beam data, however, each of the two parameters can be uniquely determined. The important point is that correct behavior can be predicted with the inclusion of the concentration dependant effective mass.

Carrier Dynamics

The decay of the nonlinear optical behavior described above is dictated by the electron recombination time and diffusion coefficient. This decay time is usually of order of a few nanoseconds. This time is faster than most electronic detection systems. It is, therefore, necessary to use other means for this measurement. By far, the most common technique is pulsed probe degenerate four wave mixing. Basically, two pulses of light are spatially and temporally overlapped in the sample. The interference of the these "write" beams in the sample sets up a grating. The intensity of the light is chosen so that in the light regions of the grating, nonlinearities in the optical properties are present. In the dark regions, of course, this does not happen. We, therefore, have a sinusoidal modulation in the refractive index of the material. A third beam, "probe", incident on this grating undergoes diffraction as discussed in Chapter 2. The lifetime of the grating depends on the lifetime of the source of optical nonlinearity. For the case of bound electrons this lifetime is almost instantaneous. If high photon energy ($E > E_g$) or intensity is used, single or two photon generated carriers will be responsible for index modulation in the grating. Then, the lifetime of the grating is dictated by the carrier recombination and diffusion coefficients. By delaying the arrival time of the probe beam and monitoring its diffraction, we can determine the lifetime of the grating. This gives us an insight into the carrier dynamics of these materials.

Experimental Setup

Figure 17 shows the forward propagating laser induced grating technique used. Single 27 ps pulse from a mode-locked, Q-switched Nd:YAG laser was split into three pulses. Computer controlled optical delay lines were placed in the path of each beam to control its arrival time. The two pump beams passed a waveplate-polarizer combination to allow continuous change in their energies. The energy ratio between the two pump beams was kept at 1:1 and they were focused to a 1 *mm* radius and crossed at the sample. Their crossing angle, 2θ, was 9.5° in air, which corresponds to a grating spacing of 6.5 μm. The plane of probe beam propagation was at an angle of 2° to the plane of the pump beams propagation. Therefore, the scattered and the transmitted probe were out of the plane of the pump beams which allowed for easy detection of the total energy in them. The probe beam energy was kept constant and had a beam radius of 0.3 *mm* at the

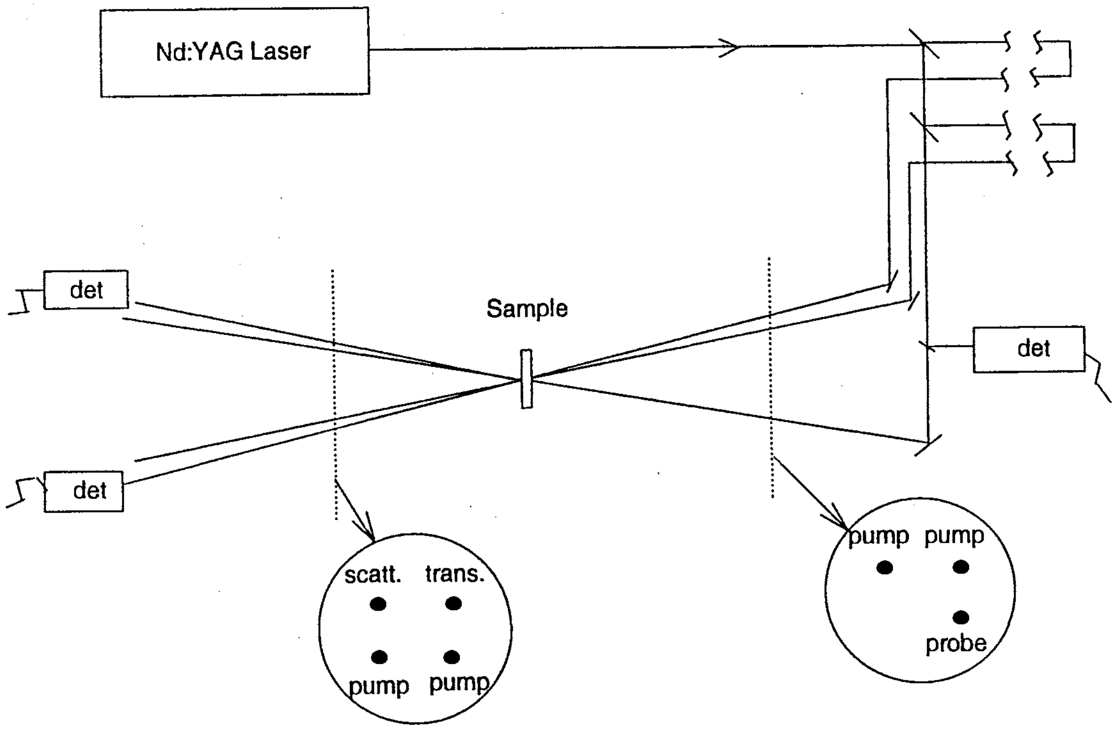

Figure 17. Experimental setup used for pulsed probe degenerate four wave mixing experiment.

sample. The smaller radius of the probe helps minimize effects arising from the Gaussian nature of the pump beam spatial profile. The energy of the transmitted and the scattered probe beam was monitored by two LaserPrecision energy meters. This was done as a function of the pump beam energy and the probe beam delay.

The CdMnSe crystals were positioned such that the polarization of the write beams were parallel to the c-axis. In the case of CdMnTe, the propagation wavevector of the pump beams were parallel to the (111) crystalographic direction. In both materials the probe beam polarization was set at 90^o from the pump beams.

Theoretical

Crossing two beams propagating in the $x - z$ plane, each with intensity, I, and wavelength, λ, polarized in the y-direction results in an interference pattern given by:

$$I(x,t) = I(t)\{1 + \cos(2\pi x/\Lambda)\} \tag{97}$$

where the grating spacing, Λ, is related to the crossing angle, 2θ, by:

$$\Lambda = \lambda/(2\sin\theta) \tag{98}$$

Inside a material, $I(x,t)$ generates free carriers via single and two photon absorption. These free carriers, then, change the refractive index of the material through FCA and FCN coefficients:

$$\begin{aligned} \triangle n &= \sigma_r N \\ \triangle\alpha &= \sigma N \end{aligned} \tag{99}$$

This generated grating scatter a probe beam in the direction satisfied by the Bragg condition. The scattering efficiency, η, is given by:

$$\eta = \frac{I_{scatt}}{I_{input}} = e^{-(\alpha+\langle\triangle\alpha\rangle)z/\cos\theta}\{\sin^2(\frac{\pi z}{2\lambda\cos\theta}\triangle n_o) + \sinh^2(\frac{z}{8\cos\theta}\triangle\alpha_o)\} \tag{100}$$

and the transmitted probe beam efficiency is:

$$T = \frac{I_{trans}}{I_{input}} = e^{-(\alpha+\langle\Delta\alpha\rangle)z/\cos\theta}\{\cos^2(\frac{\pi z}{2\lambda\cos\theta}\Delta n_o) + \cosh^2(\frac{z}{8\cos\theta}\Delta\alpha_o)\} \quad (101)$$

with

$$\begin{aligned} \Delta n_o &= \sigma_r\{N(peak) - N(valley)\} \\ \Delta\alpha_o &= \sigma\{N(peak) - N(valley)\} \\ \langle\Delta\alpha\rangle &= \sigma\frac{1}{\Lambda}\int_0^\Lambda N(x)dx \end{aligned} \quad (102)$$

where $N(peak)$ and $N(valley)$ are the number of electrons in the light and dark regions of the grating, respectively.

The decay of the grating can occur through both, (i) recombination of the carrier and (ii) movement of the free electron from the light region of the generated grating to the dark region. In the latter case, presence of an electron in the dark region reduces the contrast between the light and the dark regions. Since the scattering efficiency is related to the differences between the two regions, this means a decrease in scattering. So any time dependence of the scattering enters the equation through the time dependence of the free carriers. This is determined by the diffusion equation[31]:

$$\frac{\partial N(x,t)}{\partial t} + \frac{N(x,t)}{\tau(N)} - \nabla(D(N)\nabla N) = \frac{\beta}{2\hbar\omega}I^2(x,t) \quad (103)$$

where, in general, the lifetime, τ, and the diffusion coefficient, D, are carrier concentration dependent. The term on the right accounts for carrier generation via two photon absorption. In general, analytical solution to this equation is not possible due to the concentration dependence of the coefficients.

For a first order approximation to Eq. 103, we assume a low power input pulse with a Dirac delta function temporal profile. In this case, we expect low concentrations of generated carrier and can, therefore, ignore any concentration dependence of τ and D. Then, Eq. 103 reduces to:

$$\frac{\partial N(x,t)}{\partial t} + \frac{N(x,t)}{\tau_R} - D\nabla^2 N = \frac{\beta}{2\hbar\omega}I^2(x,t) \quad (104)$$

For a pulse spatial profile given by Eq. 97, this can be solved analytically [32]:

$$\begin{aligned} N(x,t) = \quad & N_o\{3/2 + 2\exp\left(-\frac{4\pi^2 Dt}{\Lambda^2}\right)\cos\left(\frac{2\pi x}{\Lambda}\right) + \\ & \frac{1}{2}\exp\left(-\frac{8\pi^2 Dt}{\Lambda^2}\right)\cos\left(\frac{4\pi x}{\Lambda}\right)\}\exp\left(-\frac{t}{\tau_R}\right) \end{aligned} \tag{105}$$

which is also valid if the pulse duration is much smaller than the lifetime of the carriers. This is certainly true in our case where the pulse width is 27 *ps* in duration and the carrier lifetimes are a few nanoseconds. Using the above solution for N, we see that the time dependence of $\triangle\alpha_o$, $\triangle n_o$ and $\langle\triangle\alpha\rangle$ is:

$$\begin{aligned} & \triangle\alpha_o, \triangle n_o \sim \exp\left(-t\left[\frac{1}{\tau_R} + \frac{4\pi^2 D}{\Lambda^2}\right]\right) \sim \exp(-t/\tau_g) \\ & \langle\triangle\alpha\rangle \sim \exp\left(-t/\tau_R\right) \end{aligned} \tag{106}$$

This is an important result. It states that the grating decay time is different from the increased absorption decay time. This is used later to separate the values of the two parameters, D and τ_R.

As a next approximation, a Taylor series expansion for the coefficients is used:

$$\begin{aligned} \gamma(N) &= \gamma_1 + \gamma_2 N + \cdots \\ D(N) &= D_o + D_1 N + \cdots \end{aligned} \tag{107}$$

where $\gamma = 1/\tau$. So, Eq. 103 becomes:

$$\frac{\partial N}{\partial t} + \gamma_1 N + \gamma_2 N^2 - D_o\frac{\partial^2 N}{\partial x^2} - D_1\frac{\partial}{\partial x}\left(N\frac{\partial N}{\partial x}\right) = \frac{\beta}{2\hbar\omega}I^2(x,t) \tag{108}$$

Next, we define,

$$\begin{gathered} I(x,t) = A\exp(-a^2t^2)\{1 + \cos(2\pi x/\Lambda)\} \\ n = N/N_{\mathrm{max}} \\ t' = \gamma_1 t \\ x' = x/\Lambda \end{gathered} \tag{109}$$

which upon substitution into Eq. 108 results in a dimensionless equation:

$$\frac{\partial n}{\partial t'} + n + \varepsilon n^2 - \delta_o \frac{\partial^2 n}{\partial x'^2} - \frac{\delta_1}{2} \frac{\partial^2 n^2}{\partial x'^2} = \frac{\sqrt{\pi}\gamma_1}{2a} \exp(-2a^2 t'^2/\gamma_1^2)\{1 + \cos(2\pi x')\} \quad (110)$$

where

$$\begin{aligned} \varepsilon &= \gamma_2 N_{\text{max}}/\gamma_1 \\ \delta_o &= D_o/\gamma_1 \Lambda^2 \\ \delta_1 &= D_1 N_{\text{max}}/\gamma_1 \Lambda^2 \end{aligned} \quad (111)$$

The coefficient in front of the generation term is to insure that $n_{\text{max}} = 1$. The effects of the nonlinear terms, ε and δ_1, on the spatial and temporal nature of the carrier concentration can now be investigated by solving Eq. 110 numerically. For realism, values of $2 \times 10^8 (s^{-1})$, 2.5 (cm^2/s), 6.5 μm, and 22 ps were used for γ_1, D_o, Λ, and $1/a$ respectively.

To determine the effects of ε, Eq. 110 was solved with $\delta_1 = 0$. Figure 18 shows the dependence of the spatial profile of generated carriers on ε for three delay times (a) 20 ps (b) 1.11 ns (c) 3.53 ns after the arrival of the pump beams. The solid line corresponds to $\varepsilon = 0.0$, dashed line to $\varepsilon = 0.33$ and dotted to $\varepsilon = 0.67$. We see that as time progresses the number of carriers in the nulls of the grating increase. This is due to the diffusion of the carriers from the highly populated to the less populated areas. In the figure, the overall area underneath each curve represents the total number of carriers and its decreases as a function of time indicates recombination process. Comparison of the area and the values in the nulls of the profiles for different times indicates that the main mechanism of grating erasure is due to recombination.

Next, setting $\varepsilon = 0.0$, Eq. 110 was solved for a number of δ_1 values. Figure 19 shows the dependence of the spatial profile of the generated carriers on δ_1 for the delay times used before. Here, the solid line corresponds to $\delta_1 = 0.0$, dashed line to $\delta_1 = 0.009$ and dotted to $\delta_1 = 0.028$. In this case, we see that the number of carriers in the null of the grating increases as a function of time and value of δ_1. In particular, at any given time, the number of carriers in the null of the grating increases with δ_1. This is to be expected since an increase in δ_1 means an increase

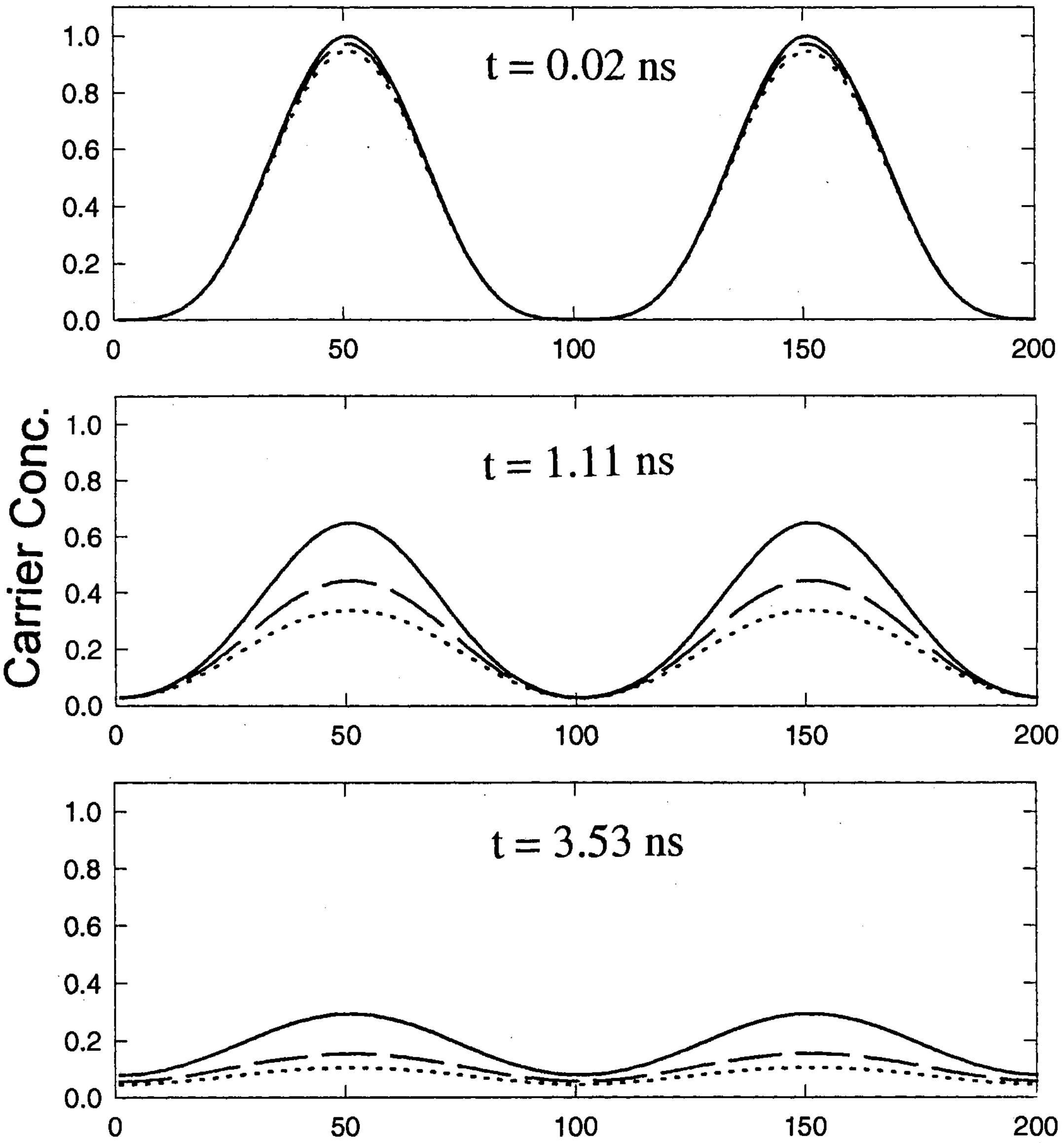

Figure 18. Dependence of the spatial profile of generated carriers on ε for three delay times (a) 20 ps (b) 1.11 ns (c) 3.53 ns after the arrival of the pump beams. In all cases $\delta_1 = 0.0$.

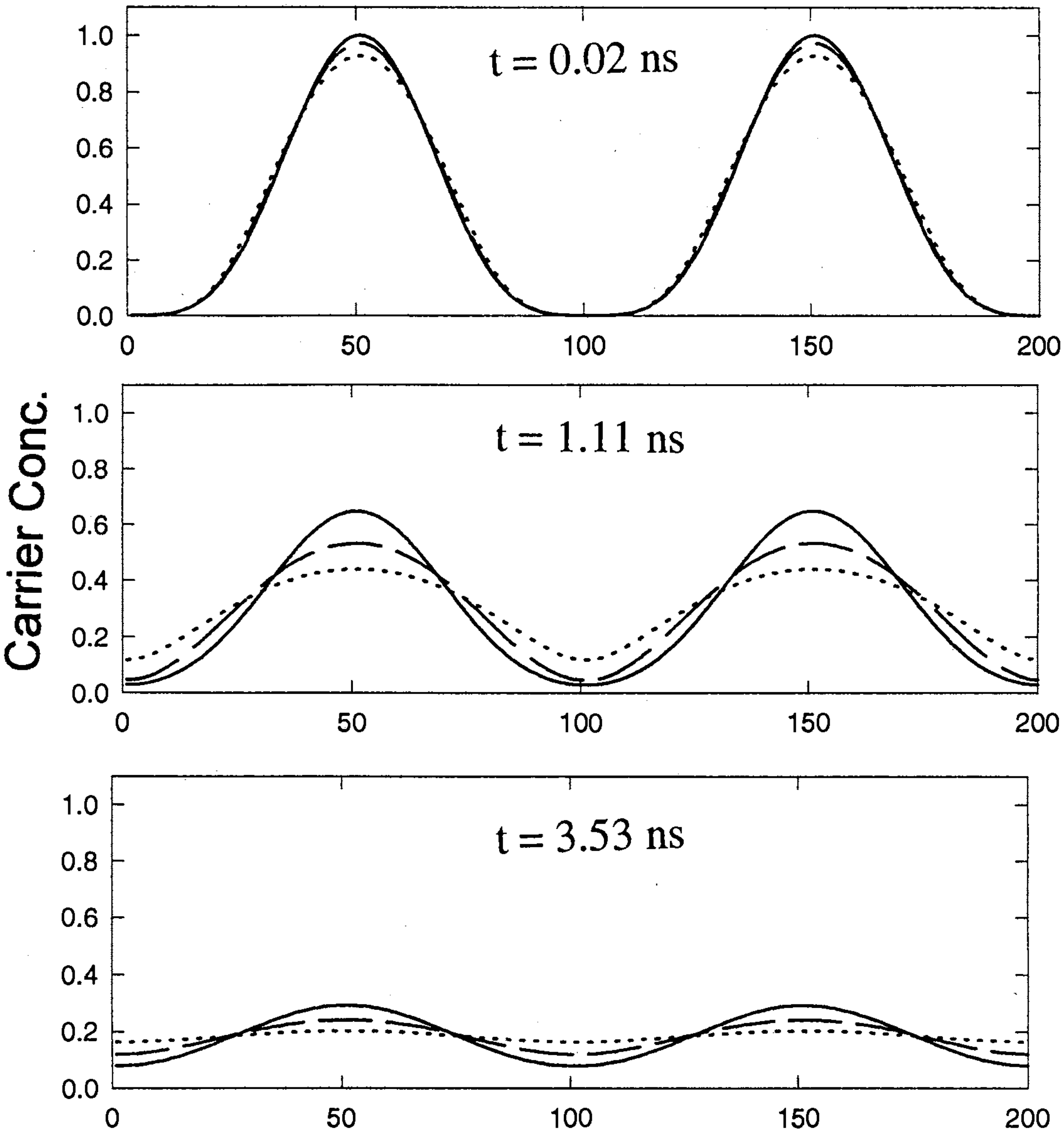

Figure 19. Dependence of the spatial profile of generated carriers on δ_1 for three delay times (a) 20 ps (b) 1.11 ns (c) 3.53 ns after the arrival of the pump beams. In all cases $\varepsilon = 0.0$

in the diffusion. As before, however, we see that the main mechanism for grating erasure remains the recombination process.

From the above and using Eqs. 100 and 102 we can determine the lifetime of the grating. Figure 20 shows the scattering efficiency as a function of the probe beam delay for different (a) ε and (b) δ_1. From the figure it can be concluded that an increase in ε or δ_1 results in shortening of the grating lifetime. Furthermore, the grating decay departs from a single exponential nature observed in the low carrier concentration regime.

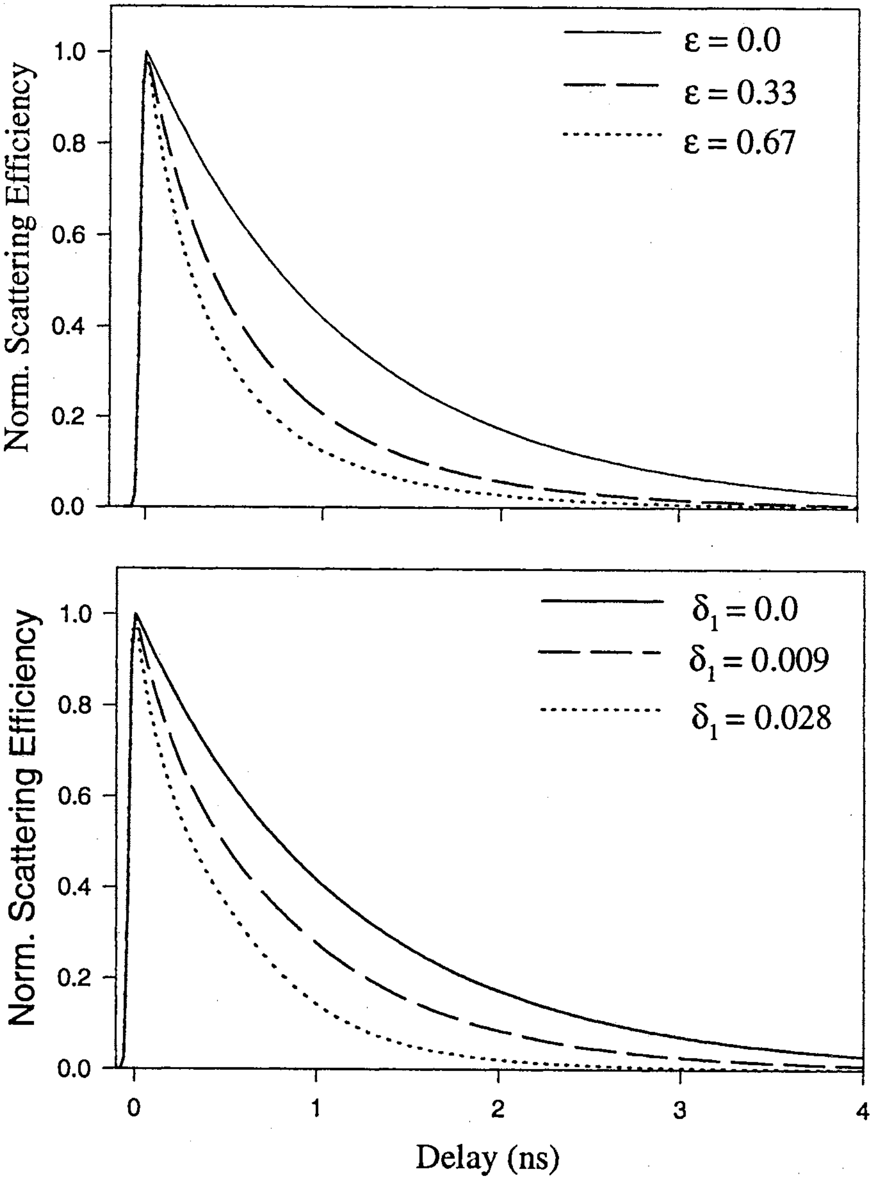

Figure 20. Scattering efficiency as a function of probe delay and (a) ε and (b) δ_1.

Results and Discussion

Figure 21 shows the scattering efficiency of the probe beam as a function of

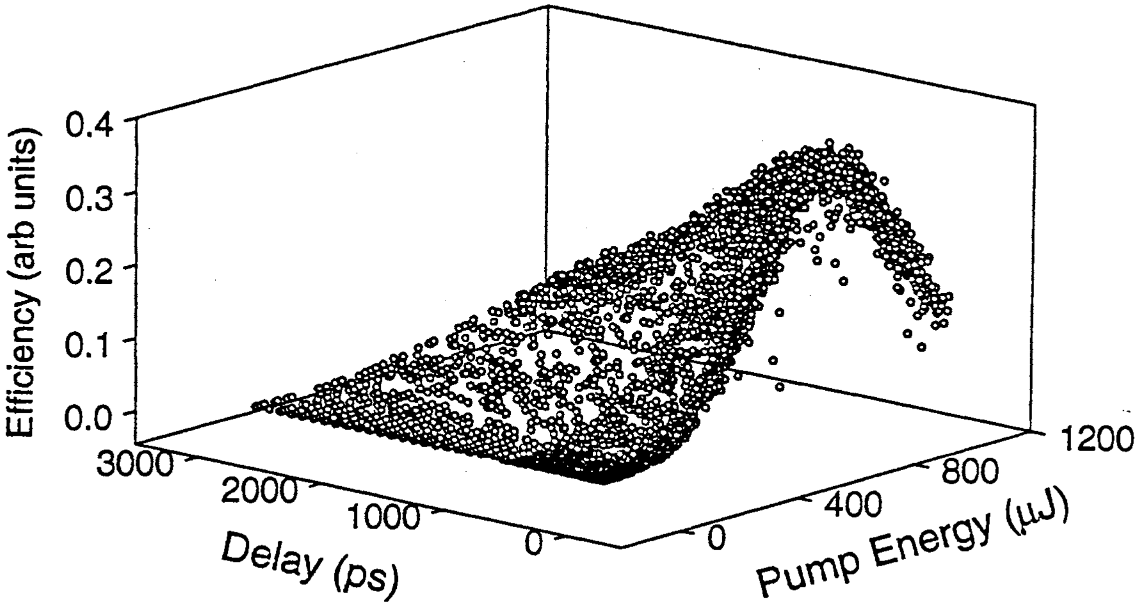

Figure 21. Scattering efficiency of the probe beam as a function of the pump beam energy and probe beam delay.

the delay and the pump beam energy for CdTe. There are two interesting time regimes to be considered, (i) delay=0 and (ii) delay > 0.

In the first case, we see that the scattering efficiency increases with the pump beam energy followed by saturation and a subsequent decrease in the scattered signal. This behavior is typical for scattering from a phase grating (first term in Eq. 100). In a highly degenerate semiconductor, however, the contributions from the absorption grating (second term in Eq. 100) can be significant. Furthermore, these contributions may oppose those due to a pure phase grating[31]. To elucidate the significance of the absorption grating, using Fig. 12 carrier concentrations in the peaks of the grating were determined for this geometry. A maximum concentration of 4×10^{17} cm^{-3} suggests that any contribution from the absorption grating can be neglected. Figure 22 shows the scattering efficiency for different carrier concentrations at zero delay. As before, Fig. 12 was used for the conversion. The fit to the zero delay efficiency of CdTe was obtained using a value of 2.6 for the magnitude of σ_r, in excellent agreement with the result found earlier.

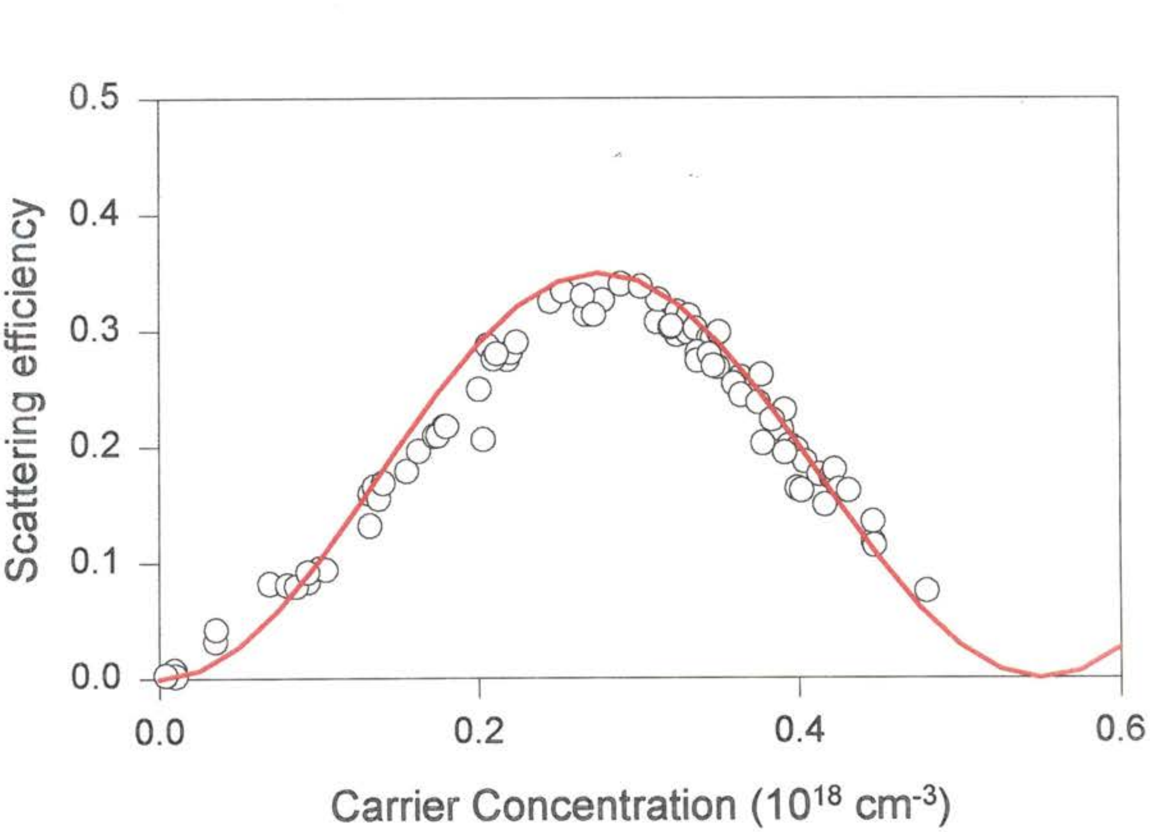

Figure 22. Scattering efficiency of the probe beam at zero delay as a function of carrier concentration.

The behavior at times greater than zero delay is dictated by the time behaviors of $\triangle n_o$ and $\langle \triangle \alpha \rangle$. We can focus on the time response from $\triangle n_o$ by re-defining the scattering efficiency as:

$$\eta = \frac{I_{scatt}}{I_{trans} + I_{scatt}} \tag{112}$$

We can do this since the energy of both, scattered and transmitted probe beam were measured during the experiment. From Eq. 106, an exponential decay of $\triangle n$ and $\triangle \alpha$ is expected with the decay time, τ_g, dictated by the recombination lifetime of the carriers and the ambipolar diffusion coefficient. Substitution of this result into Eqs. 100, 101 and 112 predicts a time dependence for the scattering efficiency of the form $\eta(t) \sim \sin^2(a\exp(-t/\tau_g))$. For small values of a, this reduces to $\eta(t) \sim \exp(-2t/\tau_g)$. Figure 23 is a plot of the time dependence of the scattering efficiency for a number of pump generated carrier concentrations. The single exponential response means that the concentration dependence of the D and τ_R can be neglected here.

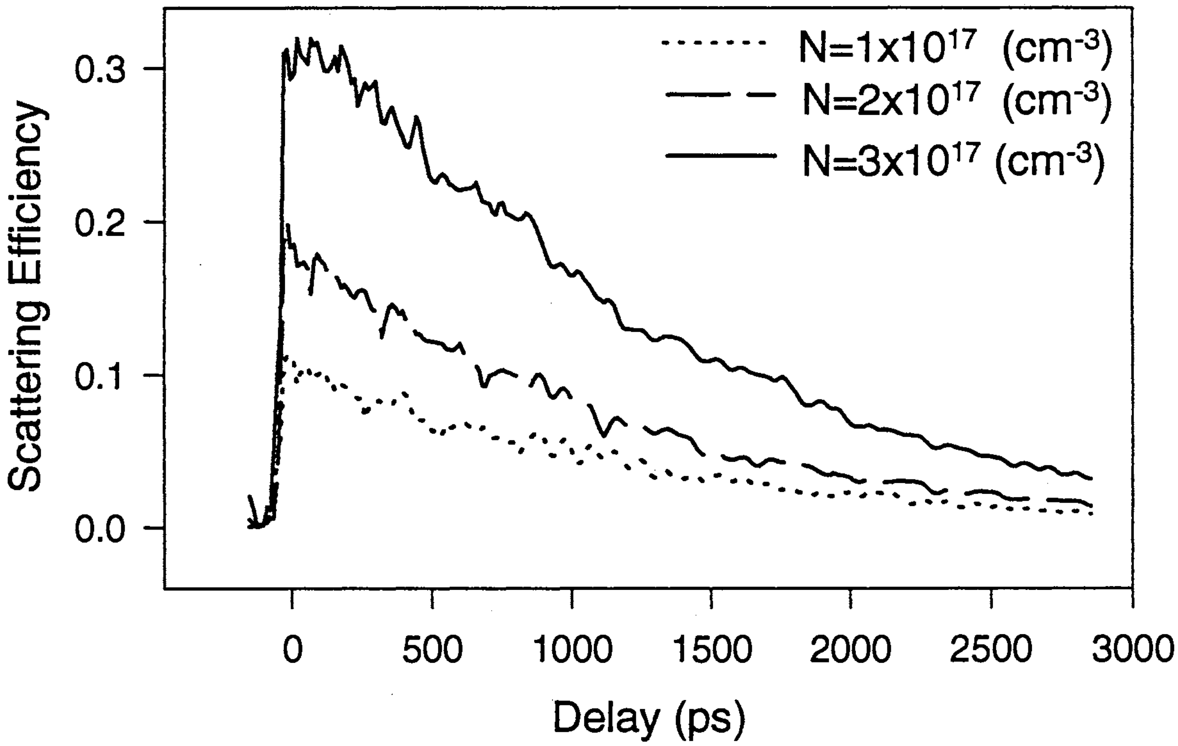

Figure 23. Scattering efficiency of the probe beam as a function of the delay for a number of pump generated carrier concentrations.

A fit to the time delay results was done for all of the samples using a single exponential function. This results in a value for τ_g which contains the ambipolar diffusion coefficient and the recombination lifetime. Therefore, another measurement is needed to uniquely determine the relative contributions of each parameter.

It is possible to determine the recombination lifetime of the carriers from the time dependence of the total probe beam energy emerging from the sample. From Eq. 100 we see that attenuation of the probe beam can occur by (i) scattering in the Bragg direction and (ii) absorption by the carriers. The latter is present for the scattered beam also, and is insensitive to the spatial nature of the carrier concentration. Furthermore, this absorption persists throughout the duration that the electrons are in the conduction band. Therefore, by monitoring the total energy of the post sample probe beam, scattered + transmitted, as a function of time, it is possible to determine the carrier lifetime. In terms of the parameters stated earlier, we now look for $I_{out} = I_{trans} + I_{scatt}$. In this case, the time response is dictated by $\langle \Delta\alpha \rangle$ which, from Eq. 106, depends on the recombination lifetime only. Figure 24 shows the total probe energy after the sample vs. time for different carrier concentrations for CdTe. The time dependence of the signal has no saturation effects, which further emphasizes that the saturation observed in the FWM

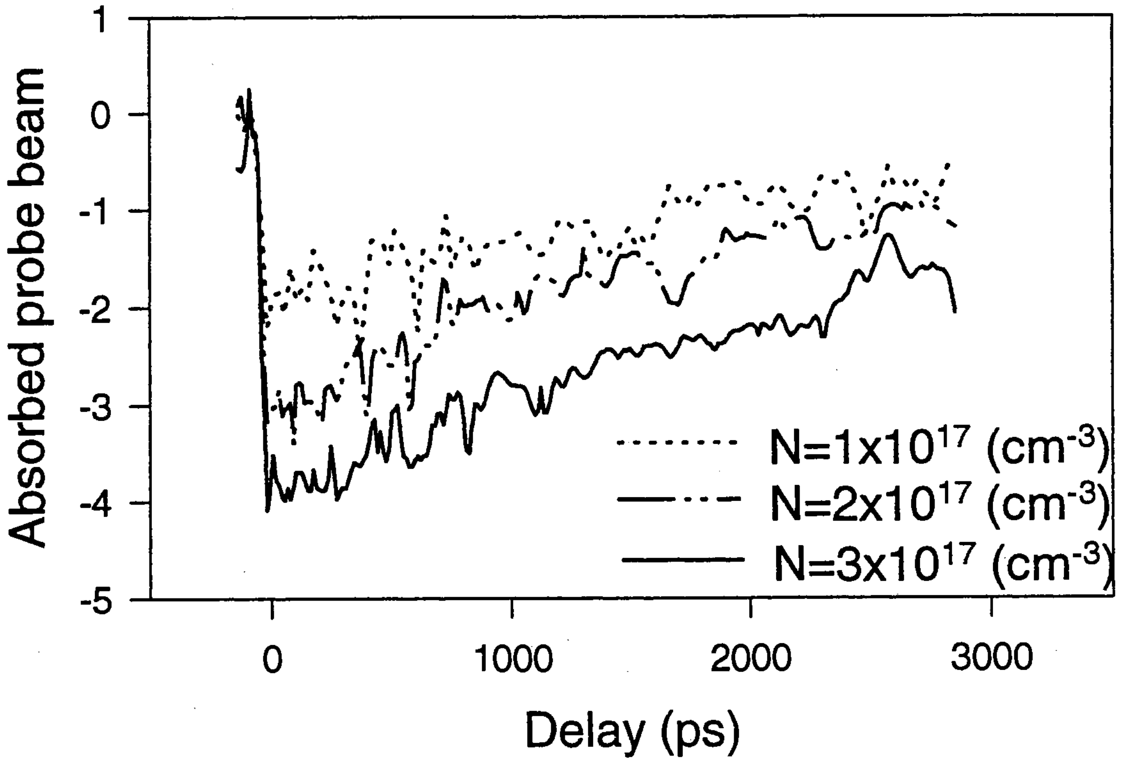

Figure 24. Loss in the probe beam energy vs delay for different carrier concentrations.

scattering efficiency was not caused by a saturation in the generated free carriers. This graph was used to determine the lifetime of the electrons in the band. It was found that for the concentrations reached the decay, τ, was a constant.

Figure 25 shows the lifetime of the electrons as a function of Mn concentration. The lifetimes of CdTe decreased with addition of Mn while for CdSe, with an exception of 30%, there was a dramatic increase. This increase is expected since addition of Mn increases the band gap which, inturn, reduces the coupling between the conduction and valence bands and, therefore, increasing the lifetime of carriers[29]. The decrease in the 30% concentration is thought to be related to the Indium doping of this sample. Doping increases the number of traps and defects which increase the coupling between the bands. In the case of CdMnTe, it is thought that the decrease in the lifetime is due to an increase in the Te defect caused by addition of Mn. This also results in a scattering of light in CdMnTe sample which was not observable in the CdMnSe samples.

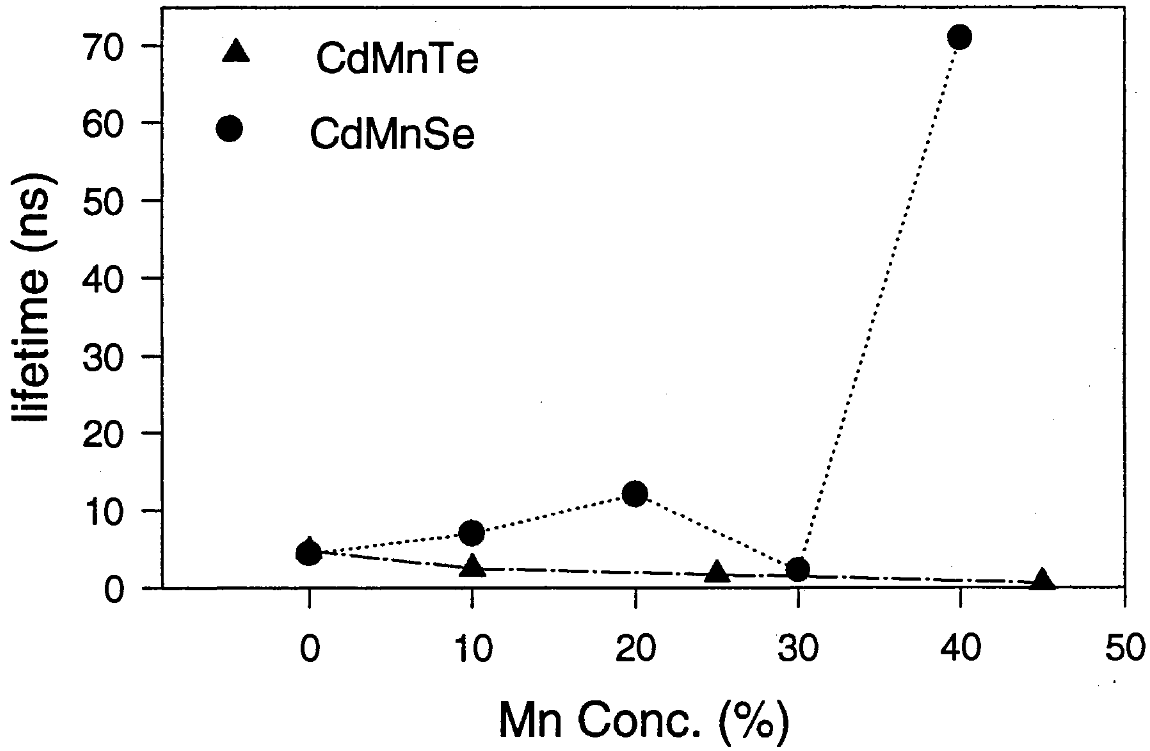

Figure 25. Life time of the electrons as a function of the Mn concentration in CdMnSe and CdMnTe.

TABLE VI Nonlinear optical parameters of DMS.

Material	$\beta(cm/GW)$	$\sigma(10^{-18}cm^2)$	$\sigma_{ro}(10^{-21}cm^3)$	$\tau(ns)$
CdSe	35	5	-2.7	4.4
$Cd_{0.9}Mn_{0.1}Se$	20	5	-1.5	7.0
$Cd_{0.8}Mn_{0.2}Se$	15	5	-2.0	12.0
$Cd_{0.7}Mn_{0.3}Se$:In	10	5	-1.1	2.2
$Cd_{0.6}Mn_{0.4}Se$	2.5	5	-0.6	71.4
CdTe	20	20	-2.5	4.8
$Cd_{0.9}Mn_{0.1}Te$	15	13	-2.5	*
$Cd_{0.6}Mn_{0.4}Te$	6.5	5	-0.75	*

Finally, with the two lifetime, τ_R and τ_g, it should be possible to determine the magnitude of the ambipolar diffusion coefficient. This was done for CdTe and a value of 2.5 cm^2/s was estimated which is in good agreement with previous measurements. This results means that it is possible to determine both coefficients from the same experiment. This is an important point since the general method for this determination was to perform the experiment for several grating spacings. This increases the error in the numerical value of this coefficient since a change in the crossing angle alters the interaction length which can not be accounted for in the simple theory used. Unfortunately in the other samples the value of D could not be determined since τ_g was dictated by the lifetime of the carriers, τ_R. The reason for this is believed to be the decrease in τ_R with an increase in Mn for CdMnTe samples. In the case of CdMnSe, the presence of the superimposed photorefractive grating maybe responsible for this.

Conclusions

Table VI is a summary of the measured parameters for each samples. There are a few points of interest. First, the two photon absorption, β, and the nonlinear refraction, σ_r, coefficients decrease with an increase in the Mn concentration. This is to be expected, since addition of Mn increases the band gap of the DMS and these coefficients are inversely proportional to the band gap. Secondly, the free carrier absorption cross section remained constant for $Cd_{1-x}Mn_xSe$ but decreased for $Cd_{1-x}Mn_xTe$. The origin of this is not known but it may be related to the strain present in $Cd_{1-x}Mn_xTe$ due to addition of Mn. Finally, the recombination lifetime of $Cd_{1-x}Mn_xSe$ increased with the Mn concentration with the exception of $x = 0.30$ value, which may be due to presence of In in these samples. Furthermore, from the fits it was concluded that for the carrier concentrations achieved ($\sim 10^{17}\ cm^{-3}$), the concentration dependence of the recombination lifetime plays an insignificant role in the recombination process.

CHAPTER IV

FULLERENES IN SOLUTION

Introduction

As early as 1977 presence of a graphitic-like particle was predicted from interstellar absorption [33]. Laser ablation of graphite surfaces demonstrated a stable 60-atom cluster with icosahedral symmetry[34]. Recently, large quantities of C_{60} were produced in a graphite arc in 100 Torr He atmosphere [35]. Spectral studies of these compounds suggested a soccerball-type, truncated icosahedral geometry. These compounds have become to be known as Bucky balls or fullerenes after the inventor of geodesic dome, Buckminster Fuller[36]. Figure 26 is the proposed structure for the two most common multicarbon structures, C_{60} and C_{70}.

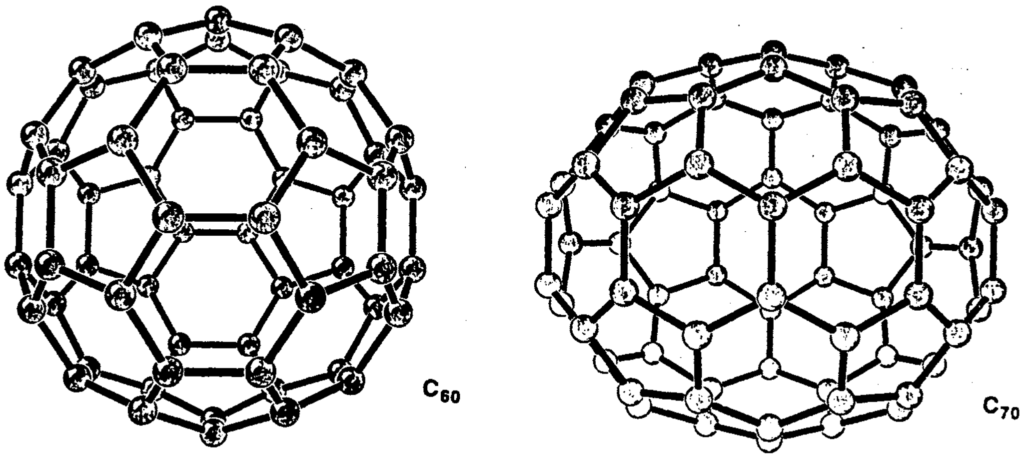

Figure 26. Proposed structures of C_{60} and C_{70}.

Indications of high degree of optical nonlinearity in C_{60} and C_{70} compounds due to their delocalized, π-conjugated electrons [37] have resulted in numerous experiments. The symmetry of these materials suggests that the greatest nonlinearity should arise from third order susceptibility tensor $\chi^{(3)}$ [9]. Therefore experiments have focused on the real part of third order susceptibility of these material using a variety of techniques such as the third harmonic generation [38], EFISH [39] and degenerate four-wage mixing. The latter has been performed with a variety of pump wavelengths and with nanosecond [40], picosecond [41–43]and femtosecond [44]pulses. The pulsed probe experiments performed have suggested two types of time responses. These responses have been associated with an instantaneous response due to $\chi^{(3)}$, and a long lived component due to excited state population. The instantaneous response, however, is shown to dominate the nonlinear optical properties during the duration of the pump beams.

Discrepancies in numerical estimations of $\chi^{(3)}$ in these material have resulted in a number of discussions. Using DFWM, Blau et al [41] estimated a relatively large $\chi^{(3)}$ of $\sim 10^{-8}$ (esu). This value was refuted by Kafafi et al [42] whose measurements resulted in a much smaller value of $\sim 10^{-12}$ (esu). They, however, did not report any contributions due to toluene. More recently, femtosecond DFWM [44]and THG [38] experiments have resulted in values of $\sim 10^{-10}$ (esu).

Nonlinear Optical Properties

Experimental

A single pulse from a mode-locked, Q-switched Nd:YAG laser operating at 10 Hz were frequency doubled to λ=532 nm with a e^{-1} width of 13 ps. It was passed through a waveplate-polarizer combination to allow for a continuous change in its energy. The pulse was then focused using a 1m focal length lens with a Rayleigh range of 30 cm. The samples were filtered and poured into a 2mm thick cuvette which was placed 30 cm behind the focal plane of the lens. The samples were 'thin' compared to the Rayleigh range of the beams ($\sim$15 times smaller) to insure applicability of the thin medium formalism[26]. The e^{-2} radius of the beam at the front surface of the cuvette was 500 μm. An aperture was placed in front of the detector to monitor the total and the on-axis transmission of the beam. The detected energy was stored in a computer as a function of the input energy of the beam. Two experiments were performed. In the first, the aperture was fully open allowing the detectors to record the total energy of the post sample beam. In the second, the aperture radius was at its smallest value to allow only the on-axis intensity of the beam to be monitored by the detector.

Theoretical

To estimate the nonlinear optical properties of fullerenes we assume that the main contribution to the third order nonlinearities is due to the delocalized π-electrons. This is an instantaneous response compared to the pulse width of 27 ps used here. This states that the recombination time of the excited states or their contribution to the total nonlinearity is very small. In this event the changes in the pump beam as it passes the sample are given by:

$$\begin{aligned} \frac{dI}{dz} &= -\alpha I - \beta I^2 \\ \frac{d\phi}{dz} &= k n_2 I \end{aligned} \tag{113}$$

where all terms have their meaning as defined earlier. These uncoupled equations can be solved independently. For an input Gaussian beam of the form:

$$I(0) = I(z = 0, r, t) = I_o e^{-2r^2/\omega^2} e^{-t^2/\tau^2} \tag{114}$$

the first of these equations results in:

$$I(z, r, t) = \frac{I(0) e^{-\alpha z}}{1 + \beta I(0)(1 - \exp(-\alpha z)/\alpha} \tag{115}$$

This is all that we need to determine the two photon absorption coefficient, β. In the open aperture experiment all of the post sample energy is collected so propagation effects are not important. In this case phase changes can be ignored. Including single reflection from the front and back surfaces of cuvette, the transmission coefficient, T, is:

$$\begin{aligned} T = \frac{E_{out}}{E_{in}} &= \int\int 2\pi r I(l,r,t)drdt \\ = \frac{2\alpha(1-R)\exp(-\alpha l)}{\sqrt{\pi}\beta I_o(1-\exp(-\alpha l))} &\int_0^\infty \ln\left[1+(1-R)\frac{\beta}{\alpha}I_o(1-e^{-\alpha l})\exp(-x^2)\right]dx \end{aligned} \tag{116}$$

where l is the sample thickness, R the reflection coefficient and E_{in} and E_{out} the incident and transmitted energy of the beam. This equation has to be solved numerically with β as a fitting parameter.

For small aperture experiment, propagation is important. Here, the phase changes play an important role and must be included. Using Eq. 115, the phase change experienced is given by :

$$\phi(z,r,t) = \frac{kn_2}{\beta}\ln\left[1+\beta I(0)(1-\exp(-\alpha z)/\alpha\right] \tag{117}$$

To find the transmission through the small radius aperture, the field at the back surface of the sample has to be propagated to the aperture. Then the radial integration in Eq. 116 is over the small aperture radius. Again using a zeroth order Hankel transform of the field at the exit surface of the sample, we can find the field at the aperture. In particular from Eq. 18:

$$E(\rho_2,z_2) = -\frac{i}{Z\lambda}e^{ikZ}e^{i(k/2Z)\rho_2^2}\int E(\rho_1,z_1)e^{i(k/2Z)\rho_1^2}e^{i\phi}J_o(k\rho_1\rho_2/Z)\rho_1 d\rho_1 \tag{118}$$

where ρ denotes the radial coordinate and Z the distance from the sample to aperture. The normalized transmittance through small radius aperture is then;

$$T = A\int\int\left|E(\rho_2,z_2)\right|^2 2\pi drdt \tag{119}$$

The A coefficient is the reciprocal of the aperture transitivity in low intensity limit. A plot of the transmittivity versus input intensity can be used to determine the n_2 coefficient.

Results

Two types of experiments were performed. In the first the aperture was completely open and all of the transmitted energy of the pulse was recorded by the energy meter. This was done for a number of different C_{60} concentrations including pure toluene. The fullerenes have absorption at the laser wavelength of 532 nm. Therefore, the concentration was kept at a level such that linear absorption did not change the effective thickness of the material. Figure 27 shows a typical result obtained for the transmittivity of a beam through a fullerene solution. The solid line is a fit to the data using Eq. 116.

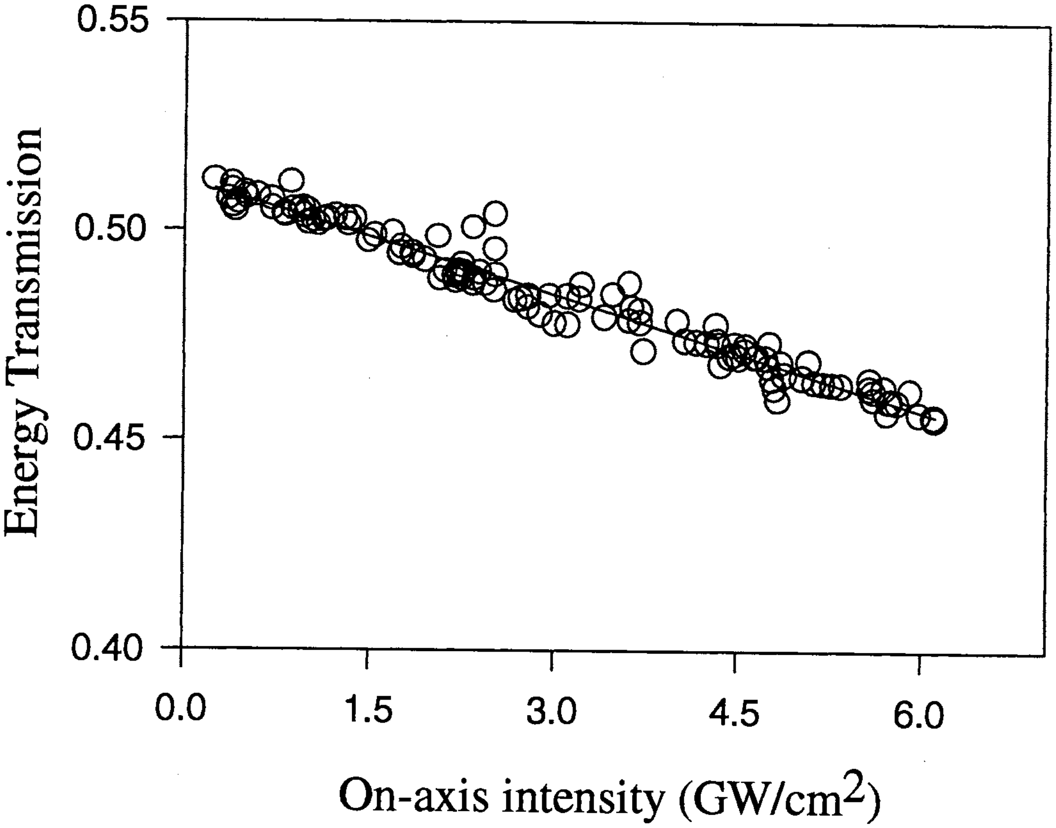

Figure 27. Typical results obtained for energy transmission through fullerene solution.The solid line is the corresponding fit.

Figure 28 summarizes the result obtained for the value of two photon absorption coefficient (TPA) for different C_{60} concentrations. We see a monotonic

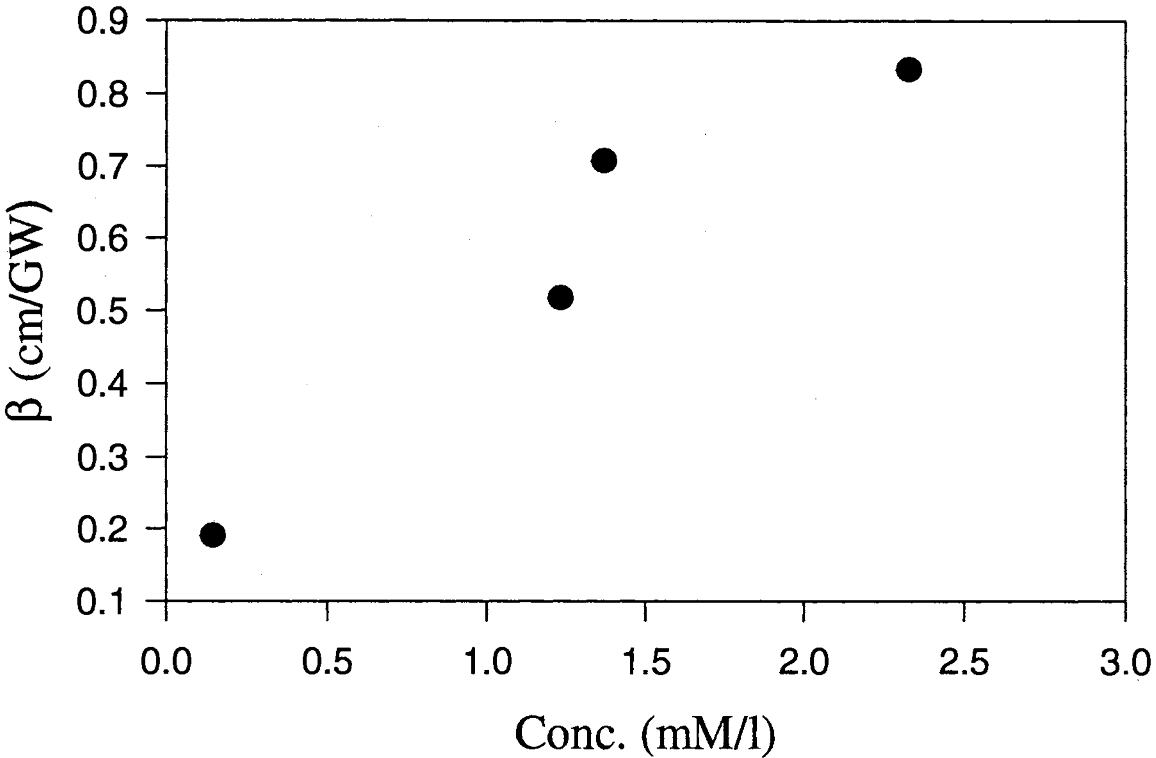

Figure 28. Results of the TPA measurements verus fullerene concentration.

increase in the TPA coefficient with an increase in the concentration. From the slope of the graph and using the definition:

$$\# \text{ of moles}(mM/l) = N/N_{av} \tag{120}$$

we get:

$$\beta(\text{per } C_{60} \text{ atomic concentration}) = 2.4 \times 10^{-25}(cm^4/GW) \tag{121}$$

This can viewed as an intensity dependant two photon absorption cross-section. In other words, the TPA has a cross-section of $2.4 \times 10^{-25} cm^2$ per unit intensity (measured in cm^2/GW).

In the second set of experiments, the radius of the aperture was set an a minimum. Figure 29 is typical results obtained for pure toluene and C_{60} in toluene. From the figure we can see that the sign of the nonlinearity for pure toluene is different from that of C_{60} in toluene. From the experimental geometry we notice

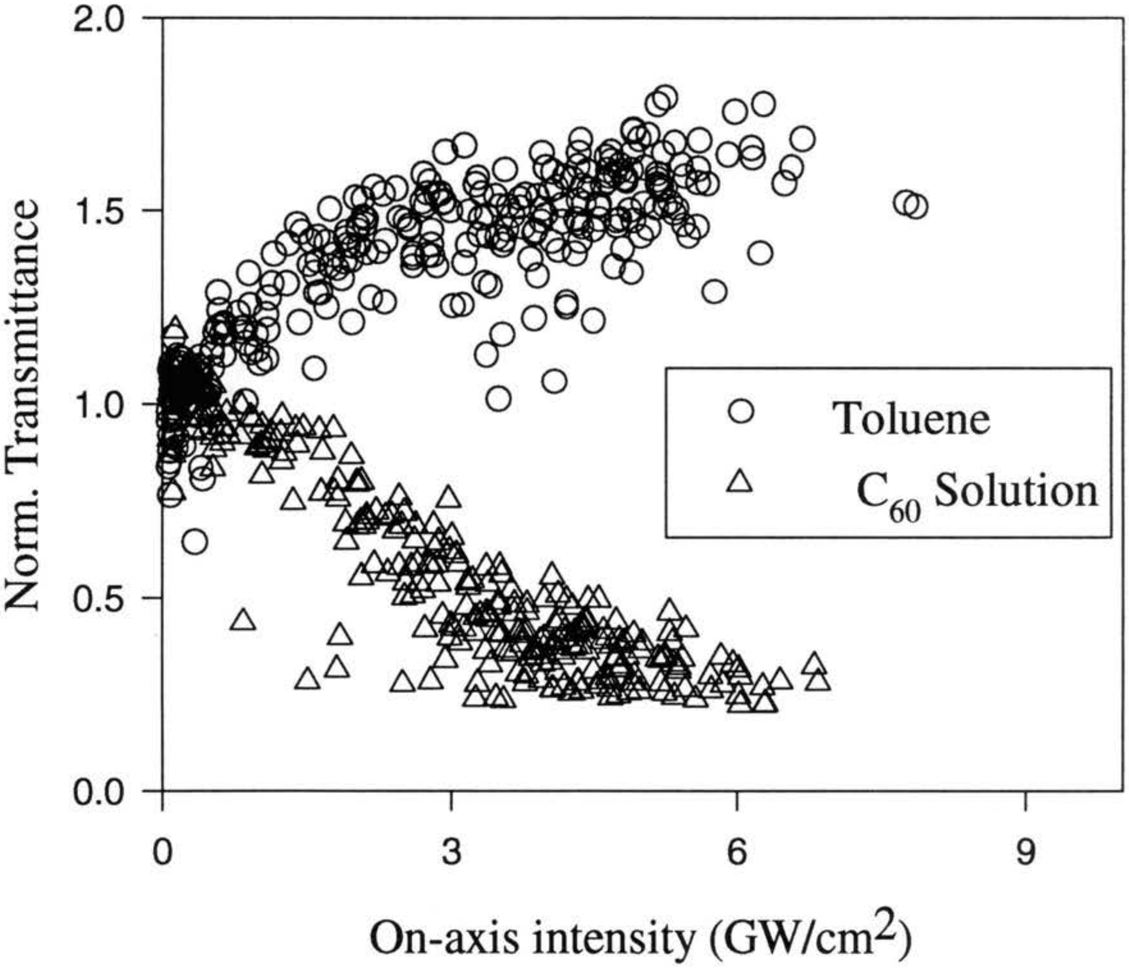

Figure 29. Typical experimental results for the small aperture experiment. The increase in the transmittivity of pure toluene suggests a focusing mechanism in the solvent.

an increase in the small aperture transmission exhibited by pure toluene indicating that the nonlinearity due to the solvent is self-focusing. In other words, as the intensity is increased the sample behaves more like a focusing lens and recollomates the expanding incident beam incident. For C_{60} in toluene, on the other hand, the decrease in the transmission beyond the expected decrease due to TPA suggests a self-defocusing effect. Here, an increase in the intensity results in an increase in the divergence of the incident beam due to presence of the sample.

Figure 30 shows the value for n_2 obtained versus C_{60} concentration. We see a negative slope to this graph which means that the contribution from the C_{60} atoms are self-defocusing as suggested before. From the slope we obtain:

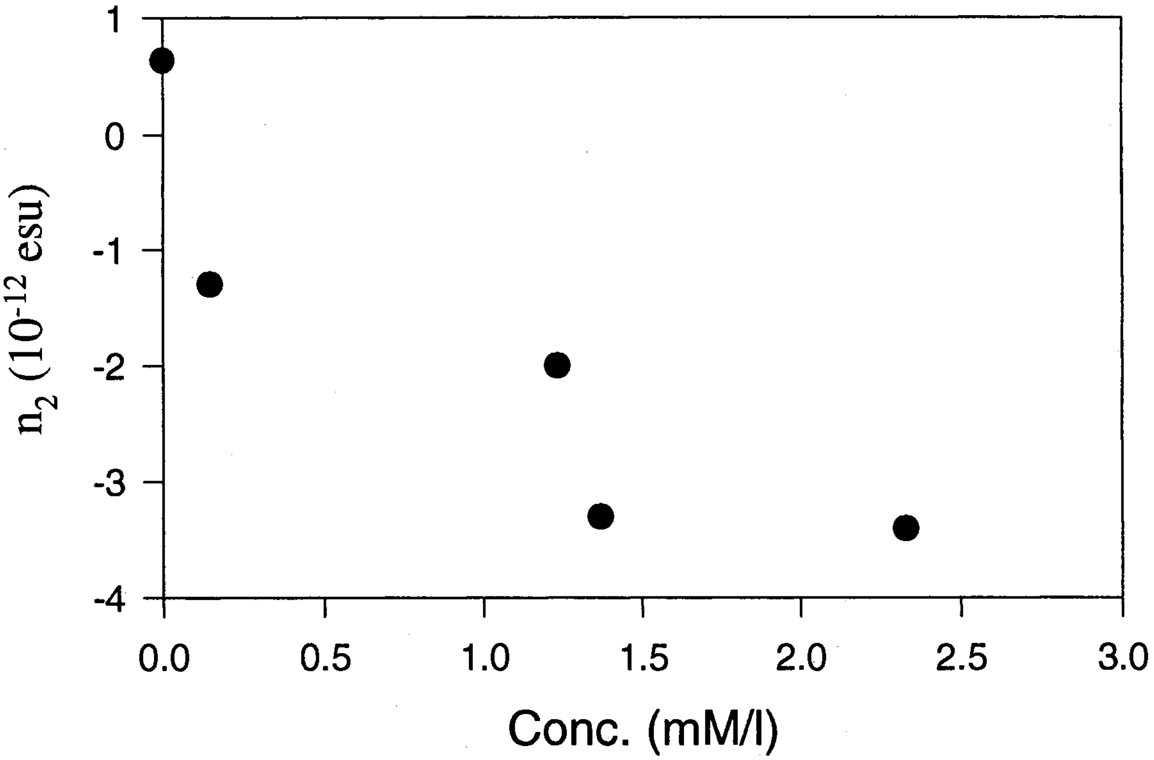

Figure 30. Numerical values for n_2 of a number of different fullerene concentrations. Note that the sign of the nonlinearity for pure toluene is opposite to the sign of the fullerene.

$$n_2(\text{per } C_{60} \text{ atomic concentration}) = -8.5 \times 10^{-24}(cm^5/GW) \qquad (122)$$

This is an important point in that most experiments of these materials are performed in toluene. This lead to erroneous results for the third order susceptibility in these material.

Laser Induced Phonons

Having found the nonlinear optical properties of these materials we look at the results obtained in a four wave mixing experiment. This technique has been extensively used for this material to determine the magnitude of the third order susceptibility tensor in these materials.

Experimental

Figure 31 shows the experimental setup used for the pulse-probe degenerate four-wave-mixing experiment performed. Single 20 ps pulse from a mode-locked, Q-switched Nd:YAG laser operating at 10 Hz was frequency doubled to λ=532

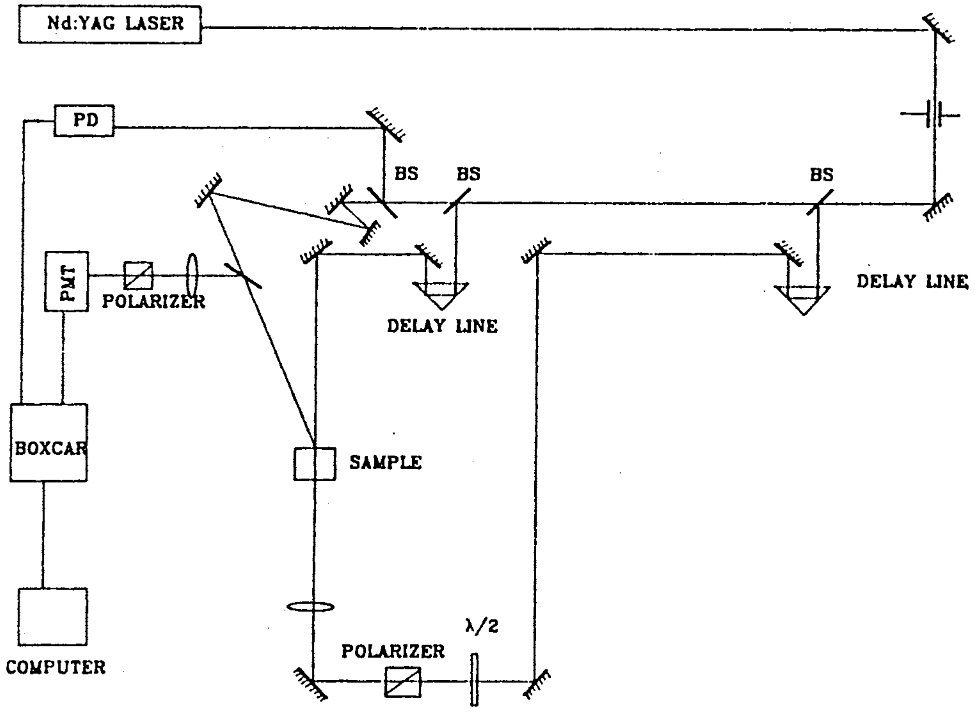

Figure 31. Experimental setup for measuring the Laser Induced Phonons and PPDFWM signal.

nm and split into three pulses. These pulses were then spatially overlapped in the sample in the conventional backward propagating degenerate four-wave mixing geometry with the counter propagating beam acting as the probe. The pulses were co-linearly polarized, with the pump beam/probe beam intensity ratio of 10:1. The scattered light was monitored by a Laser Precision Pico-Joule meter and the output was stored in a computer. The arrival of the probe beam relative to the simultaneously arriving pump beams was controlled by a computer driven optical delay line. At the sample, the three beams had a nearly Gaussian spatial profile with a radius of 250 μm for the pump beams and 200 μm for the probe beam. The smaller probe beam radius reduces effects due to the spatial nature of the induced grating, particularly effects arising from the Gaussian profile of the pump beams and variations due to pump beams crossing angle 2θ. The temporal and spatial overlap of the three beams at zero delay was determined by optimization of the instantaneous response signal from a CS_2 sample. This procedure was repeated for pure toluene solvent and for C_{60} and C_{70} solutions.

Theory

The theory of laser induced grating was discussed in the previous chapters. Here we include other effects that play a role in these materials. The scattering efficiency of a probe beam from a purely real index grating is given by:

$$\eta \propto \sin^2(\pi \triangle n_o/\lambda \cos\theta) \tag{123}$$

where all the terms have been defined previously. We have also ignored any contributions due to the absorption changes.

The time dependence of the diffracted signal reveals information about the origin of different contribution mechanisms to the above equation. For example, changes in the polarizability of the sample through the third order susceptibility tensor, $\chi^{(3)}$, are expected to have an instantaneous response. In the presence of absorption, these changes are expected to be enhanced and exhibit a decay associated with the characteristic lifetime of the excited state. Changes in the absorption coefficients occur only in presence of pump beam absorption and are, thus, non-instantaneous. Furthermore, for most applications, diffraction due to absorption changes are smaller than those due to polarizability changes and are ignored.

In some molecular crystals and liquids, the incident beams can also couple to the acoustic field of the material through effects such as thermally induced acoustic strain and electrostrictive coupling [45–48]. This results in a generation of two counter propagating ultrasonic acoustic waves in the grating wave vector direction. The wavevector of the generated acoustic mode is equal to the grating wavevector and is related to the frequency of the mode through the speed of sound in the material. Changes in the refractive index induced by these acoustic waves cause a temporally periodic scattering of the probe beam in the Bragg direction. The study of these acoustic waves is well known as Laser Induced Phonon Spectroscopy (LIPS) [49,50] and has been applied to a variety of materials. Typically, scattering due to LIPS signal is expected to be much smaller than that of the coherence peak.

Theoretically, the acoustic strain and electrostrictive interactions can be viewed as resulting in changes in the density of the medium. The change in the density results in a change in the index of refraction of the material:

$$\triangle n = \frac{dn}{d\rho} \triangle \rho \tag{124}$$

The different origins of the opto-elastic coefficient was discussed in Chapter 2 and is omitted here.

If the changes in the density of the material are due to thermal expansion, the strain induced is given by [46]:

$$S_{yy} = A \cos ky (1 - \cos \omega t) \tag{125}$$

For changes due to electrostrictive coupling, it is:

$$S_{yy} = -B \cos ky \sin \omega t \tag{126}$$

with k and ω being the grating wavevector and the acoustic frequency respectively. The strain is related to the local density changes by:

$$\triangle\rho = -\rho_o S_{yy} \tag{127}$$

Incorporating the above into the index changes, we have a total index change resulting from the two pump beams as:

$$\triangle n_{tot} = [\triangle n_{01}(I)\cos kx]_{t=0} + \left[\triangle n_{02}e^{-t/\tau}\cos kx\right]_{t>0} + \triangle n_{03}F(t)\cos kx \tag{128}$$

Where τ is the lifetime of the excited state grating similar to free carriers in semiconductors. Also $F(t)$ is the time dependence of S_{yy} and depends on the mechanism of strain induction. The coefficients Δn_{10}, Δn_{20} and Δn_{30} are the pump intensity dependent amplitudes of index changes arising from different interactions. The first term is responsible for the instantaneous (t=0) contribution to the scattered signal, arising from the $\chi^{(3)}$ including resonant enhancements. The second term allows for the scattering of the probe at time delays longer than the autocorrelation of the three beams and arises from changes in polarizability due to excited state population. The last term account for changes in the index of refraction due to laser induced acoustic waves. As stated earlier, the contribution of this term is introduction of a temporally periodic component to the scattered signal. The periodicity of the signal is related to the frequency and the nature of the acoustic mode generation.

Results

The observed scattering signal can be categorized into three probe delay time regions: a sharp scattering peak at zero delay with a FWHM equal to the autocorrelation of the three pulses, a small decaying transient signal and a periodic signal. Figure 32 shows the time dependence of the absolute diffraction efficiency for 0.4g/ℓ C_{60}-toluene solution along with that of pure toluene and CS_2. The measurements were conducted at the pump beam crossing angle of $2\theta = 21.1^o$.

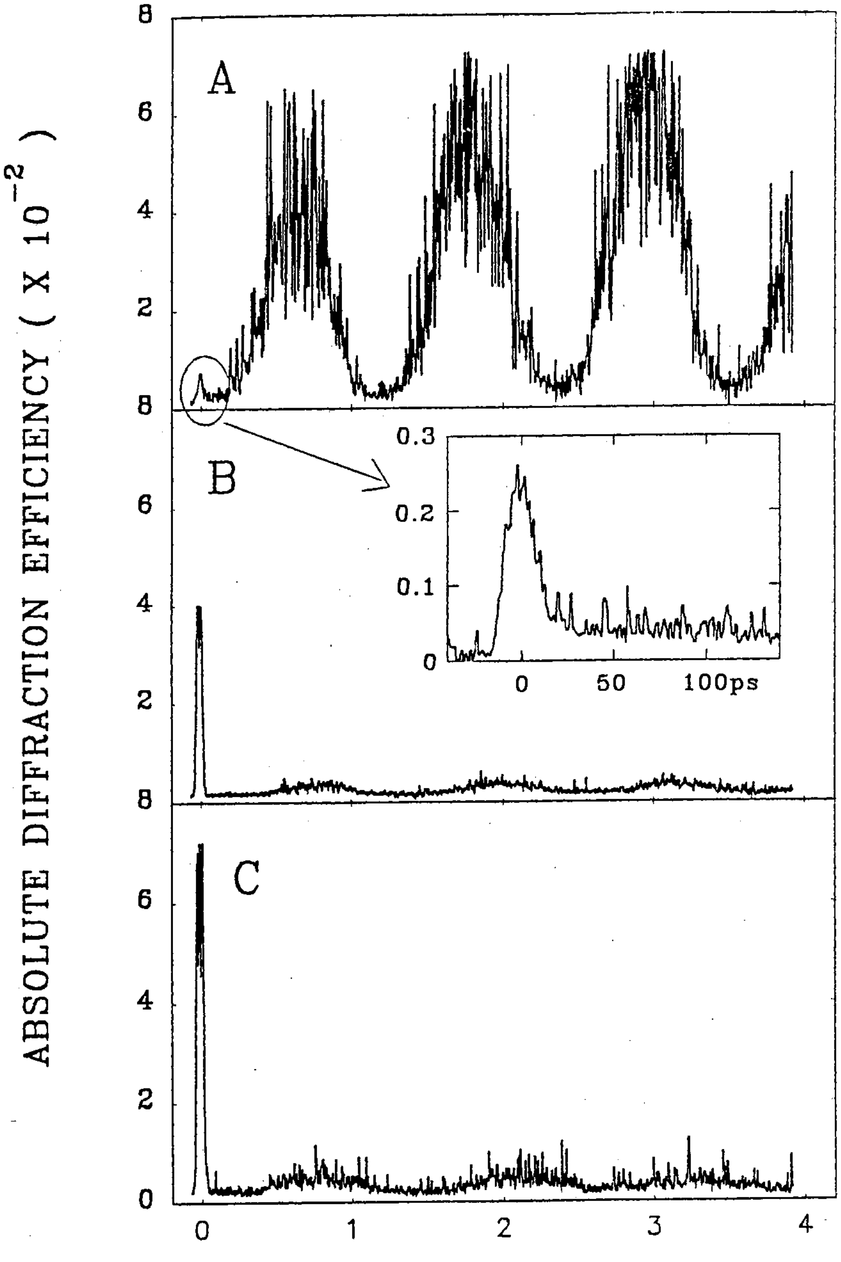

Figure 32. Time dependence of absolute scattering efficiency of (a) C_{60}-toluene, (b) toluene solvent, and (c) CS_2, respectively.

The small coherent peak at zero delay is associated with third order susceptibility while the following is due to generated acoustic waves in liquid. The inset representing the expansion of the coherent peak at zero delay in C_{60}-toluene shows the small transient signal immediately following the peak, which is associated with the excited state population. The signal noise at the peak is enhanced due to the fluctuation of the laser power. From the figure, it is seen that the intensity of each signal is dependent on the sample. In particular, the absolute scattered probe-signal intensity of the peak at zero delay (hereafter referred to as the coherence peak) decreases with addition of C_{60} to toluene. Conversely, the maximum of the periodic signal undergoes a anomalously large increase due to the presence of C_{60} and C_{70}. Therefore, while the coherence peak is the dominant scattering mechanism in toluene with an intensity ratio of I(coherence)/I(periodic)$\sim$20, the periodic peak is the dominant mechanism in C_{60}-toluene samples with a ratio of I(periodic)/I(coherence)$\sim$20. The inset is the expansion of the response at zero delay for C_{60}-toluene. The small transient signal immediately following the coherence peak is only observable in the fullerene doped solutions.

From the discussion in the last section, the periodic signal can be associated with LIPS signal. This signal is usually much smaller than the coherence peak. For example, the small oscillations seen in pure toluene and CS_2 standard (Fig. 32) are associated with the LIPS signal. However, the anomalous oscillations observed in C_{60} and C_{70} solutions are at least an order of magnitude greater than that of the coherence peak which is uncharacteristic for LIPS signals. To confirm that the periodic signal is due to LIPS mechanism, PPDFWM experiments were performed for several pump beam crossing angles. An increase in the grating spacing due to a decrease in the pump beam crossing angle 2θ results in a decrease of the acoustic phonon frequency ω in terms of $v=\lambda_{acoustic}\omega$. This manifests in an increase in the period of the LIPS signal. Figure 33 is time response of C_{60}-toluene sample for the pump beam crossing angles 2θ being 38.8^o, 11.3^o and 6.4^o, respectively, The period of modulations increased with a decrease in a crossing angle. This suggests that the origin of the periodic signal is associated with LIPS scattering.

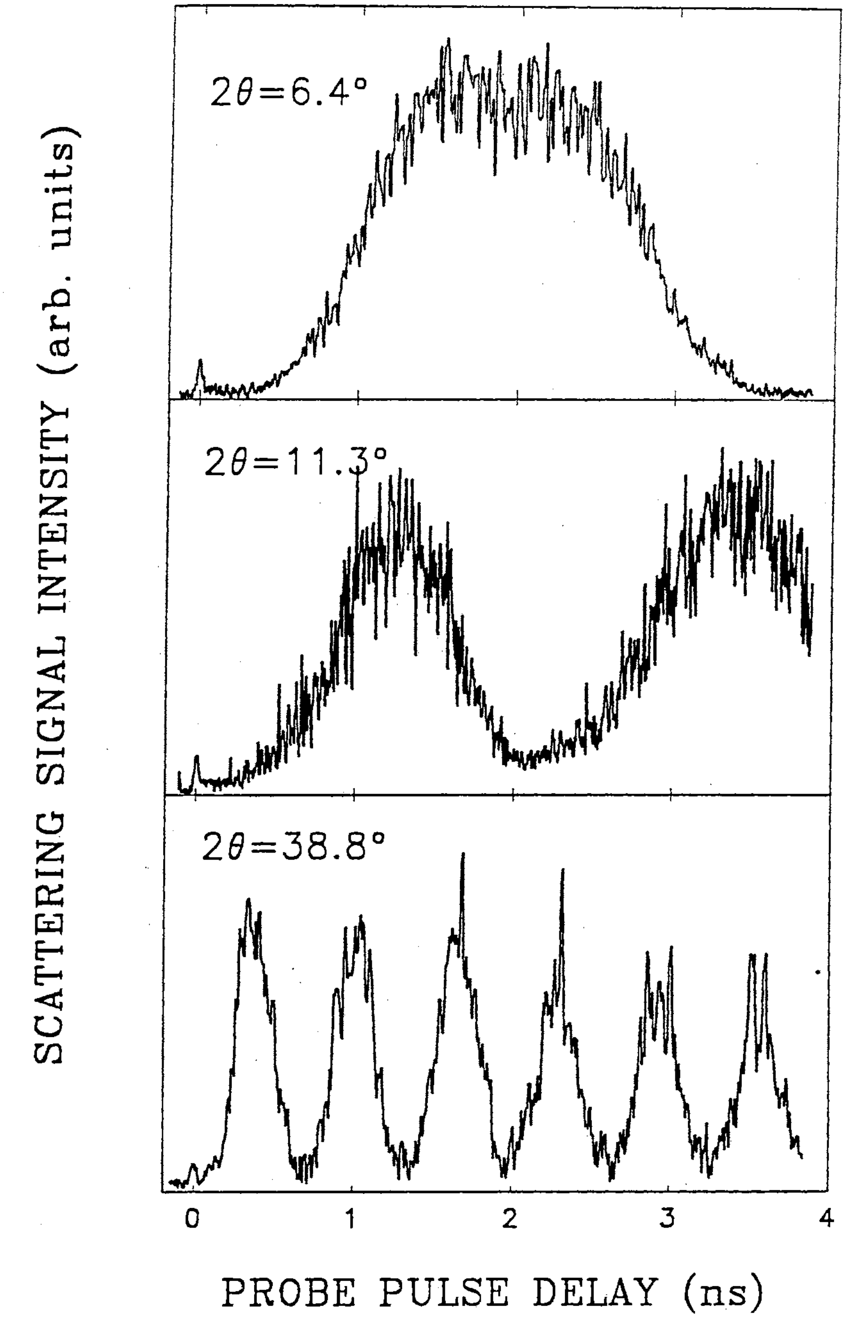

Figure 33. Time reponse of scattering efficiency of C60-Toluene at pump beam crossing angles of 6.4, 11.3 and 38.8 corresponding to oscillation frequencies of 0.25, 0.44 and 1.49 Ghz, respectively.

As pointed out earlier, the origin of LIPS signal could arise from both, the heating mechanism due to optical relaxation, and the mechanism of electrostriction coupling. For high input intensities of the two pump-beams ($>10^8$ W/cm^2), used in most of the $\chi^{(3)}$ measurements of C_{60} [41,42,44,51] using picosecond DFWM technique as well as in our experiment, optical absorption through one or possibly two photons results in heat deposited by non-radiative relaxation giving rise to a periodic temperature distribution along the grating direction. Even small amount of two photon absorption is sufficient to produce a strong LIPS signal. In our experiment the measurement of the scattering efficiency η versus pump-beam fluence F shows a power dependence as $\eta \propto F^{2.7}$, implying that both, one photon and two photon processes were present. Using $v=\lambda_{acoustic}/T$, where T is the modulation period, the speed of sound was determined from the experiment to be $1.19\text{x}10^3$m/s. This compares well to the known value of speed of sound in toluene, 1297m/s [52]. This suggests the presence of a density offset in the solution [50]. in other words, the observed LIPS signal modulates once per acoustic cycle at such a high pumping level, which indicates the dominate contribution arising from the heating mechanism. This is demonstrated in from Eq. 125 where the index changes has a null value once in a periodic cycle.

It can, therefore, be concluded that in these samples: (i) The coherence peak is associated with instantaneous changes in the polarizabilities of C_{60}-toluene through $\chi^{(3)}$. (ii) This effect is enhanced through optical absorption of fullerene from singlet S_0 to S_1 and its subsequent relaxation to T_1. These excited state population are thought responsible for the small post coherence peak signal, with characteristic lifetime of nanoseconds to a few microseconds [53,54]. (iii) The periodic response is due to thermally activated Laser Induced Phonons. From Fig. 32 it is found that scattering due to excited state populations plays an insignificant role compared to the coherent signal and can, thus, be omitted. The main contributions are, therefore, due to $\chi^{(3)}$ and LIPS.

Changes in the refractive index at zero delay can be divided as those arising from toluene and those due to fullerene, i.e. $\Delta n=\Delta n_{toluene}+\Delta n_{fullerene}$. These coefficients are related to $\chi^{(3)}$ and the values estimated through comparison with scattering from CS_2. In the case of pure toluene, this is easily done and a value of 3.7x10^{-14} (esu) was obtained for $\chi^{(3)}$. In C_{60}-toluene such a calculation yields index changes due to both, the dopant and toluene. Since the coherence peak is reduced in the fullerene solutions, it can be concluded that the contributions due to dopants are opposite in sign to those due to the solvent. This is consistent with previous studies in these materials [43]. Numerical estimations of dopant contributions are further complicated by inclusion of scattering due to absorption changes (ignored in Eq. 128). Such changes may arise in these samples since addition of dopants increases absorption at 532 nm [43].

The signal, at longer delays, due to LIPS has two main characteristics. First, the LIPS signal in fullerene-toluene is at least an order of magnitude greater than the LIPS signal due to pure toluene. Secondly, the ratio of scattered signal due to $\chi^{(3)}$ to LIPS undergoes tow orders of magnitude decrease due to presence of fullerene dopants. This reduction was found to be even larger from C_{60} to C_{70} doped toluene samples. It originates from (i) increase in the LIPS signal due to C_{60} or C_{70}, (ii) the decrease in the coherence peak due to presence of oppositely contributing factors.

To summarize the experimental results obtained, addition of C_{60} to toluene increases the LIPS signal by at least an order of magnitude while decreasing the coherence peak by a factor of 3.4 in C_{60}-toluene, and a factor of 5.3 in C_{70}-toluene. Such an effect may result in erroneous calculations of $\chi^{(3)}$ which are based on comparison of the coherence peak with a standard of CS_2.

Conclusions

Single beam experiments were performed on C_{60} solutions in toluene. The results indicate that the nonlinear refraction due to C_{60} has a defocusing effect. This is opposite to the focusing effect of pure toluene and as such care most be taken in experiments utilizing the nonlinear refraction of fullerenes. Transmission experiments on C_{60} solution suggests that single photon absorption is the dominate means of laser beam energy depletion.

Picosecond pulse probed degenerate four wave mixing experiments were performed on toluene, C_{60} and C_{70} in toluene. The time dependence of the probe scattering consisted of a peak at zero delay with a width equal to autocorrelation of the three pulses, small decaying transient signal and followed by a periodic peak. The first was attributed to $\chi^{(3)}$ of the materials, the second, to the excited state population and the third to laser induced phonon in the samples. It was found that addition of C_{60} and C_{70} to toluene results in a decrease in the coherence peak suggesting oppositely contributing factors. The samples containing C_{60} and C_{70} exhibited an anomalously large LIPS signal which is attributed to an increase in optical absorption at the pump wavelength.

Part C

MATERIALS FOR MEMORY STORAGE

CHAPTER V

PHOTOREFRACTIVE CRYSTALS

Introduction

By far the most studied materials used for optical switching and memory storage are the photorefractive crystals. Photorefractive effect relies on the linear electro-optics effect for index changes. Since, linear electro-optic effect is the first order correction to the index with respect to an applied electric field, the index change arising from it is much larger than index changes due to third order susceptibility tensor. The linear electro-optic coefficients in insulating crystals are larger than the in semiconductors[21]. Therefore, focus is placed on insulating crystals with a large electro-optic coefficient, r. Their study is usually done using four-wave-mixing experiments. Two pump beam interfere in the sample producing a periodic pattern of light and dark regions in the sample. Generated carriers in the light region migrate to the dark regions via diffusion or drift. The field setup by the displaced carriers and the site of their generation modulate the index of refraction via the linear electro-optic effect[21]. For insulator with large defect levels, continuous (cw) beam can be used to generate the carriers. Using high intensity pump beams allows band to band generation via two photon absorption (TPA) which can increase the efficiency and rise time of the signal.

The nonlinear optical responses to short laser pulses have previously been reported in photorefractive materials such as $Bi_{12}SiO_{20}$[55–61], $Bi_{12}GeO_{20}$ [61], $BaTiO_3$ [62,63], $KNbO_3$ [64], $LiNbO_3$ [65], $KTa_xNb_{1-x}O_3$[66], and Bi_2TeO_5[67] using nanosecond and picosecond pulses. The time scales for the electrooptic signals in these crystals range from less than 100 ps for $BaTiO_3$ up to 1 ms for $KNbO_3$. Here we present the results of short pulse experiments performed on a number of

Bismuth germanite (BGO), Bismuth tellurite (BTO) and Strontium Barium niobate (SBN) crystals. Since TPA is an important carrier generation mechanism, the two-photon absorption coefficient, β, is determined in these materials. Then, the results of FWM experiments are presented.

Sillenites, with the composition of $Bi_{12}MeO_{20}$ (Me=Si, Ge, Te), crystallize in a T23 cubic structure where the Bi^{3+} and Me^{4+} ions occupy octahedral and tetrahedral sites, respectively. Because of their large photoconductivity, sillenites have the greatest known photorefractive sensitivity of oxide-type crystals[68,21,69,70]. Their large photoconductivity is related to the absorption shoulder on the band edge which is characteristic of the undoped crystals[71]. This shoulder is due to Bi-ions in the Me^{4+} sites (Bi "anti-site")[70,72,73] and it can be suppressed with the addition of 1-5% Al or Ga oxide into the melt[71,74]. Preparing colorless, undoped $Bi_{12}SiO_{20}$ (BSO) crystals by hydrothermal growth, has recently been achieved [75].

The outstanding photorefractive sensitivity of sillenites permits the use of low laser beam intensities to induce refractive index gratings. The high absorption coefficient near the shoulder predicts that one-photon excitation processes are sufficient in low intensity, continuous wave (CW) photorefractive experiments. This should manifest itself in a quadratic dependence of the four wave mixing (FWM) diffraction efficiency on the write beam intensity. All models describing CW FWM use this one photon absorption approximation since the photorefractive efficiency is trap limited in the intensity range where multi-photon absorption is expected[21,76]. Additional shallow traps in Al:BGO which were revealed by thermoluminescence[77] and photochromic[78] investigations may be attractive for photorefractive applications since they predict a fast photorefractive response in these materials. One-photon excitation in Al:BGO, however, is only effective in a narrow energy range in the near UV[78].

The fast photorefractive response of the sillenites has been observed in short pulse laser excitation experiments[79–85,67]. The peak intensity of short pulse lasers is often large enough to induce two photon absorption in photorefractive oxides[86–89]. Despite the expected interest in the topic only one preliminary observation has been reported concerning nonlinear absorption in sillenites[88]. The possibility of nonlinear absorption has been recognized in a picosecond pulse photorefractive process as “enhanced excitation” [84]. The measured write beam intensity dependence of the FWM diffraction efficiency, however, has not been analyzed from this aspect in the nanosecond pulse experiments[79,82].

Bismuth tellurite (Bi_2TeO_5) is a new nonlinear optical material that has recently become obtainable with a quality suitable for optical applications [90]. This material is one of the stable forms among the numerous compositions identified in the phase diagram of the Bi_2O_3-TeO_2 system [91,92]. It crystallizes in an orthorhombic crystal structure (C_{2v}^{15}) with no center of symmetry at room temperature. The early investigations were performed on microcrystallie samples but these observations are questionable since Bi_2TeO_5 is not the only crystallizing composition in the Bi_2O_3-TeO_2 system [92]. The growth of Bi_2TeO_5 single crystals using the Czochralski method has been reported [90,93,94], and some electric [93,95], optical [90,94,96–98], and acoustic [96] data have been published for single crystals. The undoped Bi_2TeO_5 crystal is transparent in the 400-7000 nm range [90,94,98]. The position of the absorption edge exhibits an orientation anisotropy when measured with polarized light [98]. Strong anisotropy has also been observed in the refractive indices [96,97], and the reflectivity spectra [98].

The first nonlinear optical properties of Bi_2TeO_5 were observed on microcrystalline samples [93,94]. Recently, photorefractive effects have been reported in Bi_2TeO_5 single crystals using both continuous wave and picosecond pulse write beams [99–102]. The decay of the photorefractive signal in Bi_2TeO_5 has multiple components with several contributions to the signal already identified. Among others, there is along lived FWM signal which lasts for more than two years without any fixing procedure[101]. FWM experiments with picosecond-duration laser pulses have been performed and indicated the existence of two-photon processes in Bi_2TeO_5 [102]. However, without a direct measurement it was not possible to estimate the contribution of the nonlinear absorption to the creation of photorefractive gratings.

The last ferroelectric material studied is Strontium Barium Niobate ($Sr_xBa_{1-x}Nb_2O_6$), SBN:100x. It has been extensively studied for applications in optical storage and processing in the continuous wave (cw) laser regime[103–105]. SBN crystals are ferroelectric with an open tungsten-bronze structure. The Sr^{2+} and Ba^{2+} ions have a 15- and 12-fold site, respectively while the niobium occupies a 6-fold site. They posses a tetragonal symmetry (point group $4mm$) at room temperature [103]. Proper Sr-Ba ratio can result in a very large Pockel coefficients in these materials namely, r_{33}.

SBN displays excellent nonlinear optical properties, in particular, they are an attractive photorefractive materials because of their large r_{33} electrooptic coefficient. Additionally, SBN is one of only a handful of materials that exhibit self-pumped phase conjugation[105]. Material properties can be tailored by varying the crystal composition and by incorporating impurity ions at open lattice sites.

Two Photon Absorption

Theoretical

When light passes through a crystal, its amplitude is attenuated by surface reflections, absorption, scattering, and absorption of the second harmonic of the incident light. In a non-phase matched, optical quality crystal used here, the losses are primarily due to refection and absorption. Considering only single reflection from the front and back surfaces, the change in the beam irradiance, I, is given by:

$$\frac{dI}{dz} = -\alpha I - \beta I^2 - \sum_i \sigma_i N_i I \tag{129}$$

where α, and β are the single and two photon absorption coefficients and $\sigma_i N_i$ accounts for absorption due to free carriers, excited states and pump beam repopulation of the trap levels (generally termed excited state absorption). Here N_i is the number of absorption centers and σ_i is the cross-section for each center.

If we ignore the last term, excited state absorption, Eq.129 has a solution:

$$I(x,y,z,t)=\frac{I(x,y,0,t)e^{-\alpha z}}{1+\frac{\beta}{\alpha}I(x,y,0,t)(1-e^{-\alpha z})} \tag{130}$$

where we have assumed propagation in the z direction. Including a single reflection from the front and back surface we get:

$$I(x,y,z,t)=\frac{(1-R)^2I(x,y,0,t)e^{-\alpha z}}{1+\frac{\beta}{\alpha}(1-R)I(x,y,0,t)(1-e^{-\alpha z})} \tag{131}$$

where R is the reflection coefficient.

The experimentally determined values is the incident and transmitted energy of the laser. From this measurement, the transmittivity, T, of the material can be determined. For a sample of thickness l, this is given by:

$$T=\frac{\int\int\int I(x,y,l,t)dxdydt}{\int\int\int I(x,y,0,t)dxdydt} \tag{132}$$

We consider two types input pulses (i) spatially and temporally Gaussian beams and (ii) uniform spatial and Gaussian temporal beams. The first case was studied in the previous chapter. It results in:

$$T=\frac{2\alpha(1-R)\exp(-\alpha l)}{\sqrt{\pi}\beta I_o(1-\exp(-\alpha l))}\int_0^\infty \ln\left[1+\frac{\beta}{\alpha}(1-R)I_o(1-e^{-\alpha l})\exp(-x^2)\right]dx \tag{133}$$

For the second case, the radial integration results in the area of the beam and we get:

$$T=\frac{(1-R)^2\exp(-\alpha l)}{\sqrt{\pi}\tau}\int_{-\infty}^{\infty}\frac{dt}{1+\frac{\beta}{\alpha}(1-R)I_oe^{-(t/\tau)^2}(1-e^{-\alpha z})} \tag{134}$$

In both of the above case we assumed that:

$$I_o=\frac{E_o}{\pi^{3/2}\omega^2\tau} \tag{135}$$

where E_o, ω, and τ are the energy, e^{-1} radius, and e^{-1} time of the laser pulse.

Bi_2TeO_5 (picosecond)

experimental. Single crystals of Bi_2TeO_5 were grown by the Czochralski method in the research Laboratory for Crystal Physics, Budapest, Hungary. The details of material preparation and crystal growth can be found in ref. [90]. In these experiments high-purity undoped samples were used. The Fe concentrations of selected samples was measured by atomic absorption spectroscopy to be less than 10^{-5} mole/mole. This resulted in better optical quality and lower linear absorption in the transparent region than found in the crystals used in the earlier investigations [98,100]. The Bi_2TeO_5 single crystals have a (100) cleavage plane along which parallel, mirror-flat surfaces can easily be obtained. In the present measurements the laser beams were incident on such a freshly cleaved (100) surface. the other two edges of the samples were oriented by X-ray diffraction and cut by a diamond saw parallel to the [001] and [010] crystallographic directions. Throughout this section we use the orientation convention from ref. [106] which corresponds to the a=1.16, b=1.646, and c=0.552 nm unit cell parameters.

In the nonlinear absorption experiment a Continuum Model YG671C Q-switched and mode locked Nd:YAG laser was used as the excitation source. The frequency doubled (532 nm) output of the laser has a pulse duration of about 13 ps and a repetition rate of 10 Hz. The laser beam profile in the TEM_{00} mode had a Gaussian intensity distribution. The optical setup for the nonlinear absorption measurements is shown in Fig. 34. For simplification, the lenses and irises that were used are not shown in the figure. Two types of measurements have been conducted. First, the energy transmission was determined by measuring the attenuation of strong (pump) laser pulses through the sample (part a in Fig. 34). The polarization of the pump beam was vertical. The incident and transmitted laser pulse energies were measured by a Laser Precision Corporation Model Rm 6600 two-detector energy meter. The fluence dependence of the signal from the two detectors was calibrated without a sample.

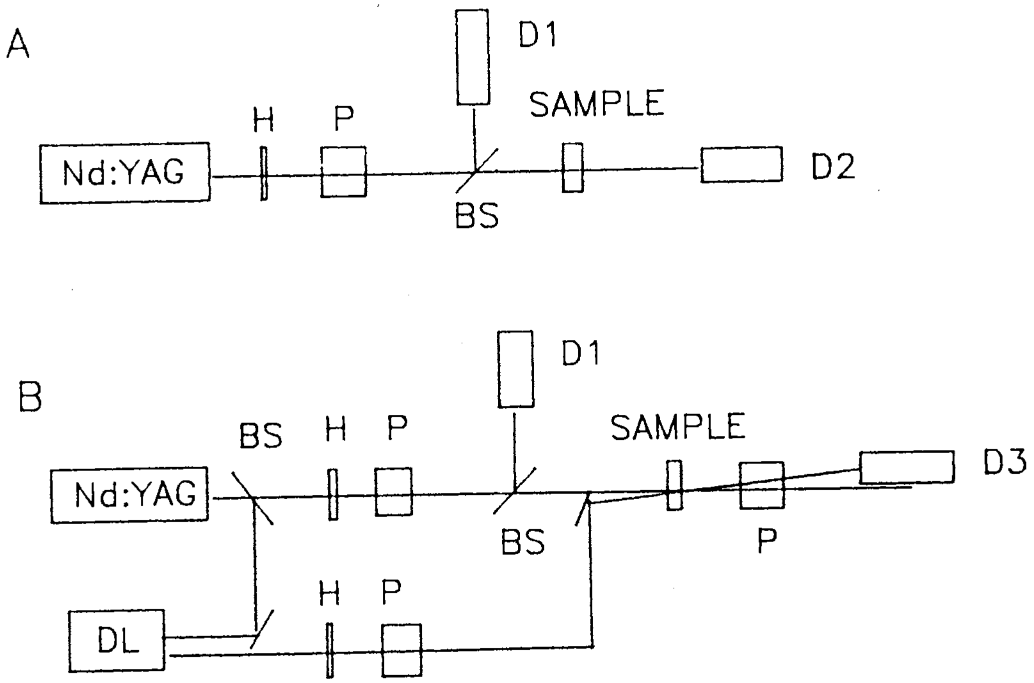

Figure 34. Experimental setups for measuring the nonlinear absorption by (a) Two photon absorption and (b) free carrier absorption.

In another experiment a weak time delayed probe beam was also applied (part b in Fig. 34). Here the probe beam attenuation was detected as a function of the pump beam fluence at different delay times with respect to the pump pulse. The delay time of the probe pulses were controlled by a motor driven optical delay line. The zero delay between pump and probe pulses was determined by adjusting for the maximum intensity of the picosecond FWM signal from a CS_2 sample as was described in ref. [107]. The polarization of the probe beam was horizontal and its incident fluence was kept fixed at 0.5 $\mu J/cm^2$ for each pump beam investigated. The transmitted probe beam was detected by a fast photodiode and analyzed by a TEKTRONIX Model 2440 digital oscilloscope. A polarizer placed after the sample and the 0.4o crossing angle between the pump and probe beams provided good beam separation even when the pump beam was four hundred times stronger than the probe beam.

High fluence (20 mJ/cm^2) write pulses, applied at a frequency of 10 Hz for several minutes, resulted in an observable color change in the illuminated part of Bi_2TeO_5 samples [102]. Typically, a yellow spot appeared which was darker than the practically colorless surrounding area of the undoped sample. In the present experiments this permanent coloration was avoided by only using a short series (16 shots) of laser pulses in the same crystal area. The coloration was checked by examining the transmission of the weak probe beam before and after the pump beam exposure. At the highest pump fluences investigated only a slight coloration was observed but the 532 nm absorption was negligible when a few shots were applied to the same spot. Signal averaging was done by repeating the series of pulses four times using a fresh crystal area for each series. Thus each experimental point in the figures represents the average of 64 individual laser pulses.

results and discussion. Figure 35 shows the energy transmission of Bi_2TeO_5

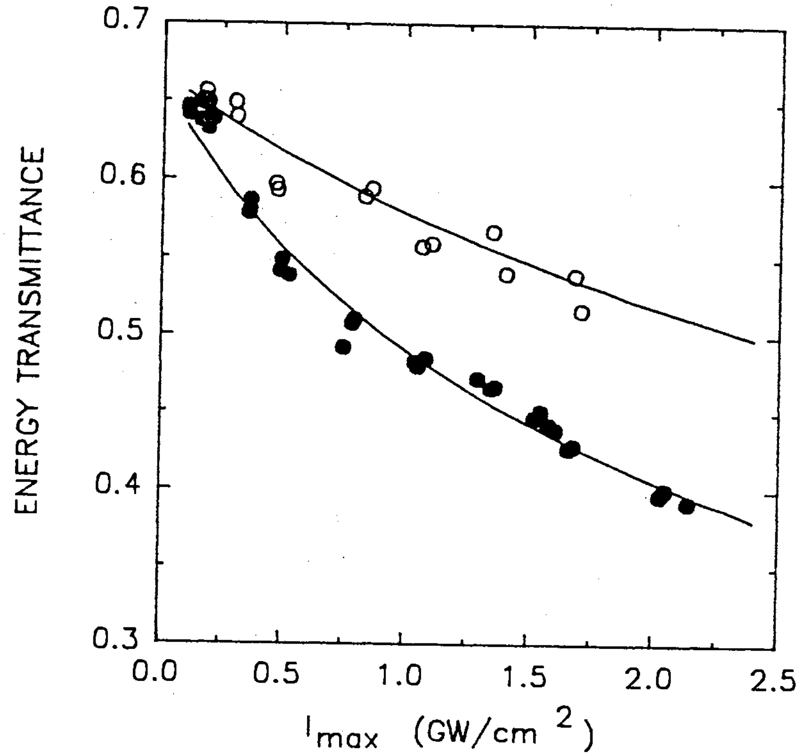

Figure 35. Energy Transmission vs Io with polarization parallel to [001] direction of BiTeO.

as a function of the maximum irradiance of the laser pulses for two different crystal samples. The 4.4 mm thick sample (filled circles) is a crystal of improved quality while the 1.2 mm thick sample (open circles) is from the same standard crystals used in the four-wave mixing experiments. In the experiments presented in fig. 35 the laser beam polarization was parallel to the [001] axis. The data for beam polarization parallel to the [010] axis are shown in fig. 36. The solid line is the fit

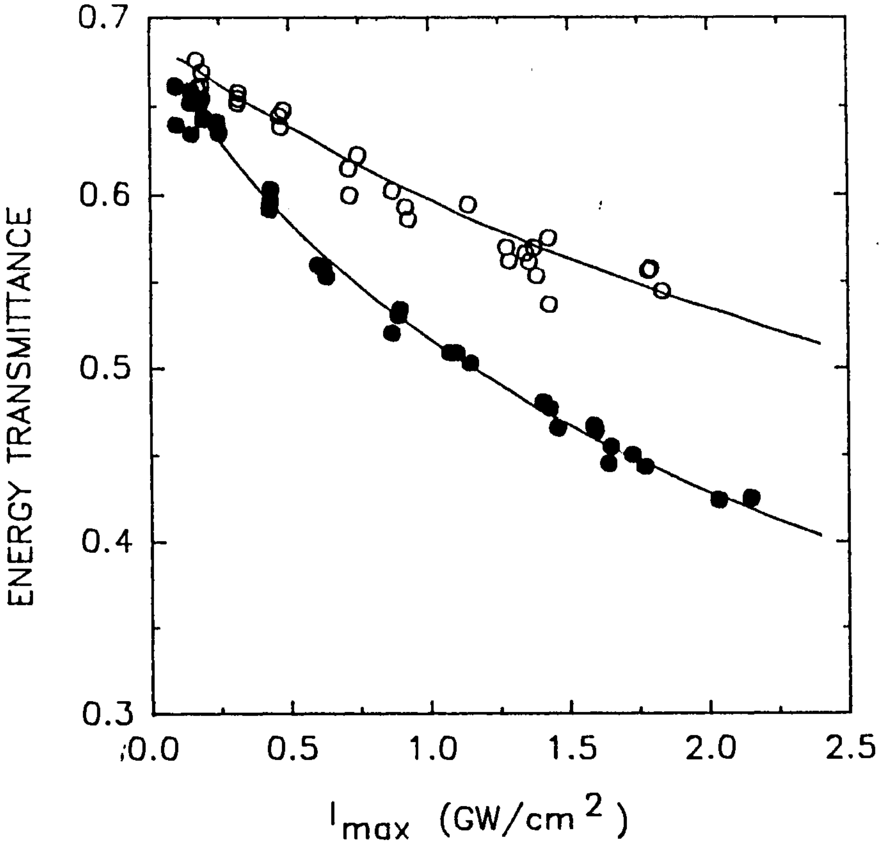

Figure 36. Energy Transmission vs Io with polarization parallel to [010] direction of BiTeO.

to the data obtained using Eq. 133. The fit was done using Mathematica package with β as the only adjustable parameter. The values for the absorption coefficient, α and the reflectivity, R where taken from literature values of these materials published earlier. Table VII shows the optical parameters used in fitting for both polarization directions. As expected α and β depend on the crystal quality. In the 4.4 mm thick sample a slight orientation anisotropy is observed in both α and β for the [001] and [010] polarization directions.

TABLE VII Optical parameters used in the fitting of the TPA measurements.

Parameter	Polarization	Data
Reflectivity [a]	[001]	0.172
	[010]	0.158
Sample from standard quality crystal [b], $d = 1.2$ mm		
Linear abs. coeff. (α)	[001]	0.25 cm^{-1}
	[010]	0.25
Two-photon abs. coeff. (β)	[001]	4.7 cm/GW
	[010]	4.7
Sample from improved quality crystal, $d = 4.4$ mm		
Linear abs. coeff. (α)	[001]	0.09 cm^{-1}
	[010]	0.07
Two-photon abs. coeff. (β)	[001]	3.2 cm/GW
	[010]	3.0

We notice from the results that the TPA coefficient of the thicker samples is lower than the thinner samples. This can be attributed to a number of effects including the excited state absorption neglected in our calculations. To elucidate the effect of excited state absorption, a delayed probe beam was introduced. Figure 37 shows the attenuation of the delayed probe beam as a function of the pump beam intensity for a 4.4 mm thick Bi_2TeO_5 sample. The data in fig. 37 are the ratio of the transmitted probe beam energy with and without the pump beam. Two probe beam delay times were chosen, 30 ps (open circles) which is slightly longer than the duration of the laser pulses and 2 ns (filled circles) which is expected to be longer than the decay time of the free charge carriers [102]. From the data, we see that the exclusion of the excited sate absorption will not result in significant alteration in the values of TPA obtained. In particular, a decrease of <4% in the total transmission was seen at input intensities of 2 $\mathrm{GW/cm^2}$.

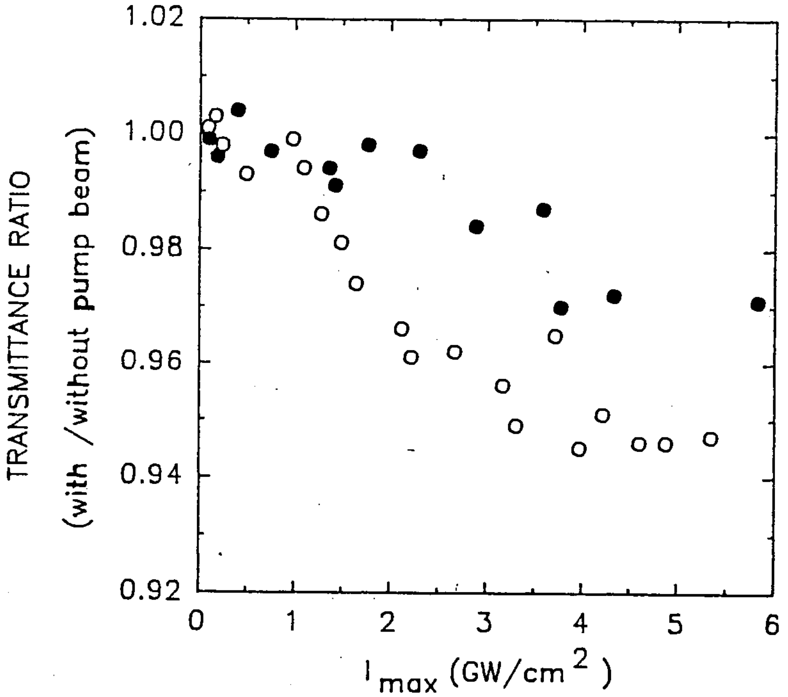

Figure 37. Probe beam attenuation due to the generated carriers at 30 ps (open circles) and 2 ns (filled circles) delay.

Figure 37 also shows that at high pump intensities an absorption induced by the strong pump beam is smaller after 2 ns than after 30 ps. We expect an increase in the excited state absorption if it was due to the retraped electrons by the defects. The decrease at 2 ns suggests that the main contribution to the excited states absorption is from the free carrier absorption.

SBN (picosecond and femtosecond)

experimental. The nominally undoped and iron-doped, optical quality $Sr_{0.60}Ba_{0.40}Nb_2$((SBN:60) single crystals used in the experiments reported here were grown using the Czochralski technique. The iron concentration of the doped crystal was 0.012 weight percent and it is expected that iron is present in both its Fe^{2+} and Fe^{3+} charge states. An automatic diameter control unit was used in the growth of the iron-doped sample to obtain striation free crystals. Individual samples were cut from the boule, optically polished, and completely poled to a single domain using fields less than 10 kV/cm[103]. The dimensions of the samples were $5.0\times5.7\times5.7$ mm^3 and $5.9\times6.1\times6.1$ mm^3 for the undoped and iron-doped respectively.

The subpicosecond source used was the amplified output of a Spectra-Physics model 3500 synchronously pumped femtosecond dye laser. The pump source for the dye laser was a Spectra-Physics model 3800 cw, mode-locked Nd:YAG laser whose pulses were compressed via the standard optical fiber/grating pair method and then frequency doubled to 532 nm. The 580 nm, 350-450 fs duration dye laser pulses were then amplified by a three stage pulsed dye amplifier (PDA). The PDA was pumped by an injection seeded, Q-switched Spectra-Physics model GCR-3 Nd:YAG laser. Single high energy subpicosecond pulses were obtained by operating the amplifier in its single shot mode. For the picosecond laser studies the source was the frequency doubled output of a Continuum model YG571C Q-switched and mode locked Nd:YAG laser producing single 20 ps pulses at 10 Hz. An individual pulse was then separated using a mechanical shutter.

In the experiment to determine the two photon absorption (TPA) coefficient single laser pulses were passed through the sample and the energy transmission coefficient was measured as a function of incident pulse energy. The incident energy was varied using a polarizing beam splitter preceded by a polarization rotator. The polarization was maintained such that it was the same as a write pulse in the FWM experiments described below; perpendicular to the c-axis of the crystal. The incident and transmitted laser pulse energies were measured with a Laser Precision model Rm-6600 universal radiometer with two model RJP-735 probes. The spatial profile of the picosecond laser source at the sample surface was determined using a 15 micron pinhole and a photodiode. A Gaussian profile having a e^{-1} radius of $r_0 = 0.061$ cm was observed. The Gaussian temporal profile was measured via autocorrelations to have a half width $\tau = 13$ ps at the e^{-1} point. The spatial and temporal profiles of the femtosecond laser at the sample surface were such that they were best modeled as uniform (crossectional area=3.14×10^{-2} cm^2) and Gaussian (half width at e^{-1}, $\tau = 240$ fs) respectively.

results and discussion. The energy transmission coefficient was measured for a single 13 ps pulse through a sample by monitoring both the incident and transmitted energies. Data were collected for a range of incident energies and the results for the undoped and iron-doped samples are plotted in Fig. 38. Equation 133 was fit to this data using the commercial program Mathematica while allowing β to vary as free parameters. α was also allowed to vary in the fit but its value was restricted to ±10% of the value determined using a Cary 2400 spectrophotometer. The solid lines in the figure represent the results of the fitting procedure. The parameters for the undoped sample were, $\alpha = 0.05$ cm^{-1} and $\beta = 2.3$ cm/GW, and for the Fe-doped sample they were, $\alpha = 0.1$ cm^{-1} and $\beta = 2.15$ cm/GW. A value for the reflection coefficient was calculated by using the published value for the index of refraction of SBN:60[108]. This value was confirmed to be valid for our samples by a simple Brewster's angle experiment and calculation. The resulting value for the intensity reflection coefficient is $R = 0.16$.

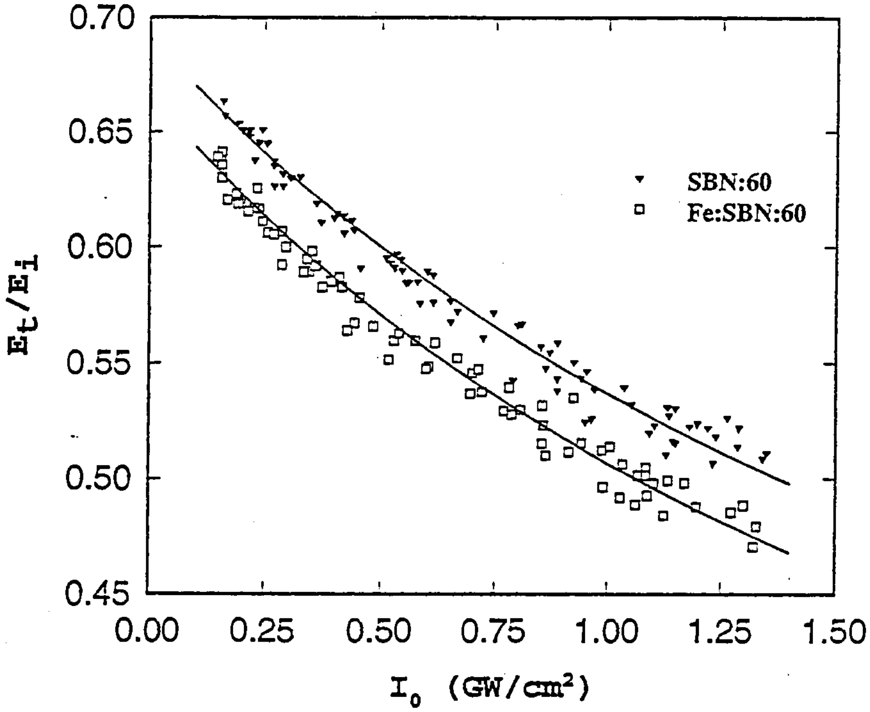

Figure 38. Picosecond two photon absorption of SBN and Fe:SBN and the fit (solid lines).

Figure 40 is a plot of transmission coefficient versus incident intensity for the

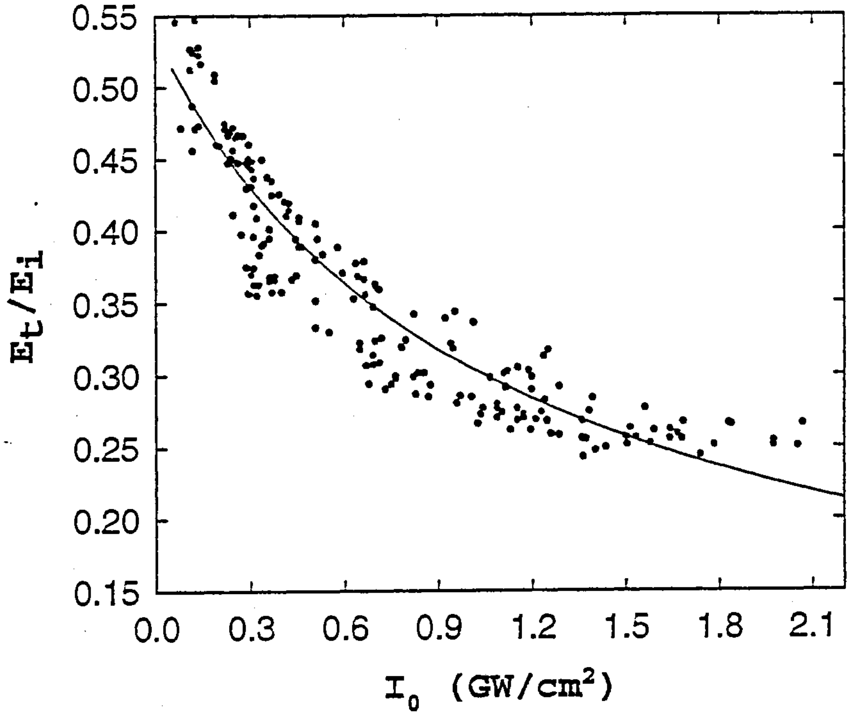

Figure 39. Femtosecond nonlinear absorption in SBN and Fe:SBN with fit (solid lines).

experiment using the subpicosecond laser source. The solid line represents a fit of Eq. 134 to the data where, once again, β is a free parameter. The resulting value for the TPA coefficient is 2 cm/GW, in reasonable agreement with that measured for the shorter wavelength of 532 nm.

Using the subpicosecond laser system we have eliminated the possibility of significant contribution from free carrier absorption by monitoring a weak probe pulse delayed 2 ps behind the original strong one. The probe was a split component of the strong pulse and 1000 times less intense. A mechanical delay line was used to obtain the 2 ps time difference. If there were free carrier absorption, the probe pulse would have been attenuated increasingly as the strong pulse energy is increased. Transmitted probe pulse energies were recorded as a function of incident strong pulse energies. The numbers were compared with the probe transmission recorded when the strong pulse was blocked from entering the sample. Except for a small *increase* in transmission of the probe pulse at the lower energies its transmission was unaffected by the presence of the strong pulse. This result supports, to a good approximation, the exclusion of single photon free carrier absorption in our calculation of β. The increased transmission at low pump pulse energies could be due to an initial saturation of the linear absorption.

$Bi_{12}GeO_{20}$ (picosecond)

experimental. Single crystals of BGO were grown by the Czochralski technique at the Research Laboratory for Crystal Physics in Budapest. The Starting Bi_2O_3 and GeO_2 compounds were obtained by a conversion from 5N purity Bi and Ge metals, respectively. The technical details for the crystal growth can be found in ref.[80]. Three kinds of BGO crystals were prepared:

BGO1 – undoped BGO grown from the standard stoichiometric melt composition.

BGO2 – grown from stoichiometric melt composition with 2 mole % Al_2O_3 added to the melt.

BGO3 – also grown with 2 mole % Al_2O_3 dopant but the Bi_2O_3 content was reduced proportionally to the dopant.

The experimental setup used for the nonlinear absorption measurement was the same as that used in the BiTeO experiment. In this case, however, the delayed probe beam was omitted. The laser used was a frequency doubled (λ =532 nm), mode-locked, and Q-switched Nd:YAG laser operating at 10 Hz with pulse width of 13 ps. Single pulses were focused in the sample using a 1m focal length lens. The lens produced a e^{-1} beam radius of 270 μm at the front surface of the sample and a Rayleigh length of $\sim$ 20 cm. The polarization of the beam was oriented parallel to the c-axis of the crystals and its energy was controlled by a waveplate-polarizer combination. The 6% beam splitter preceding the lens provided a reference pulse for the determination of the incident energy of the laser. The energy of each pulse, transmitted and reference, was monitored by a dual probe Laser Precision RM-6600 energy meter. The calibration of the reference was done by monitoring the transmitted versus reference pulse energies in the absence of a sample. The energy of each individual transmitted and reference pulse was recorded in a computer via GPIB interface.

results and discussion. Figure 40 shows the energy transmission coefficient as a function of maximum irradiance for the BGO1 sample. The circles and triangles are for the sample thickness of 1mm and 5mm, respectively. Figures 41 and 42 show the results obtained for experiments performed on the heavily Al-doped BGO2 and BGO3 samples. Equation 133 was integrated numerically and fitted to

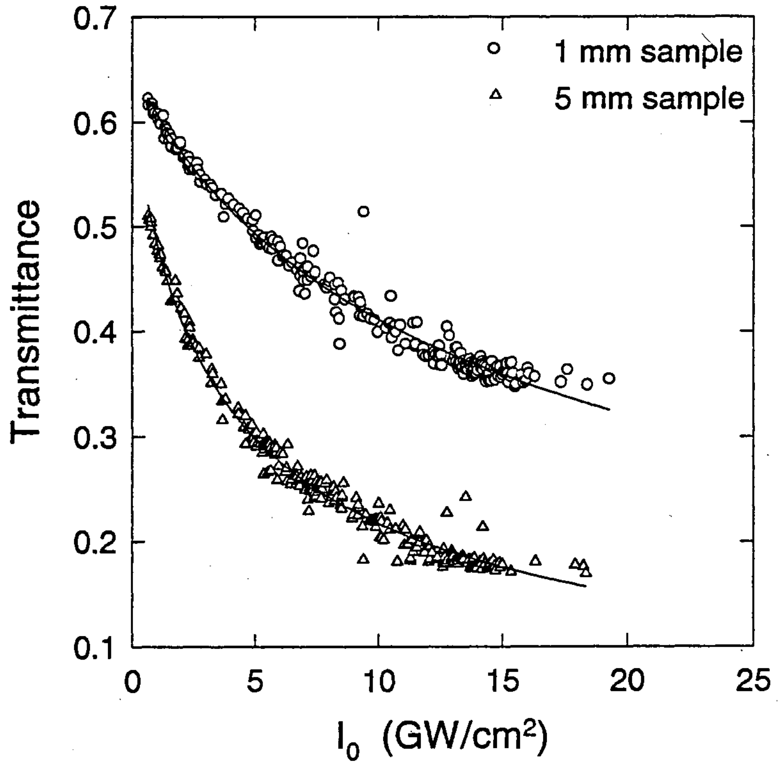

Figure 40. Transmission of light versus input intensity for BGO1 crystal. The solid line is the fit.

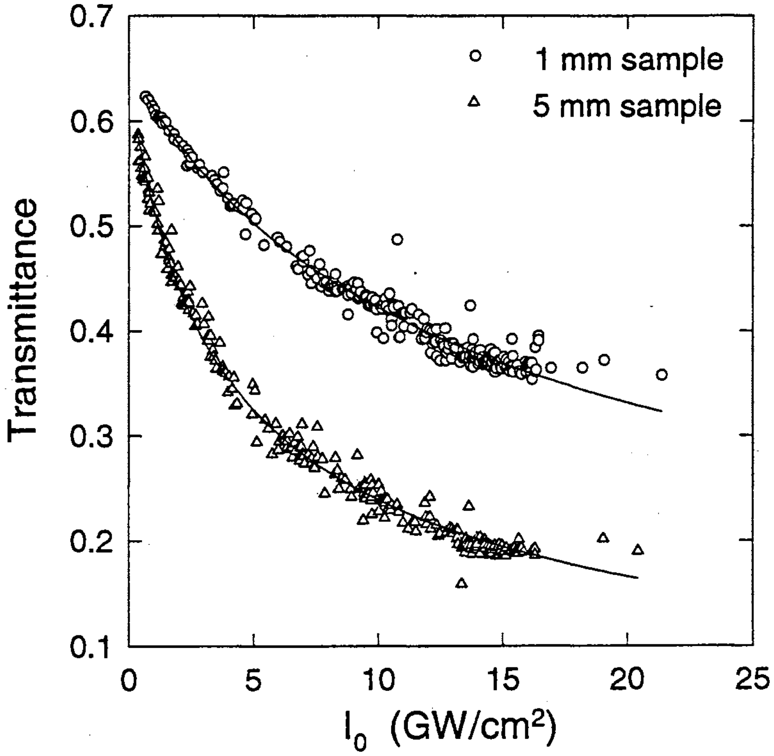

Figure 41. Transmission of light versus input intensity for BGO2 crystal. The solid line is the fit.

the data obtained using the commercial program "PeakFit". α and R were determined by direct absorption measurement using two different sample thicknesses. Therefore, only one adjustable parameter, β, was used in the fitting procedure

Table VIII summarizes the values of the physical parameters measured for these materials. The TPA coefficients of the thicker samples have a smaller numerical value than those for the thinner samples. This difference may be due to the assumptions used in the derivation of Eqs.129-133:

i) It was assumed that the beam radius in the sample remained constant. This assumption is not valid for thick samples or samples which exhibit lens type nonlinearities. For photon energies used ($\hbar\omega/E_{gap} \succ 0.7$), both bound and free electrons result in self defocusing[17]. The reduction in the on-axis irradiance due to this defocusing is greater in the thicker samples. Therefore, the true average on-axis irradiance in the thicker sample is smaller than the

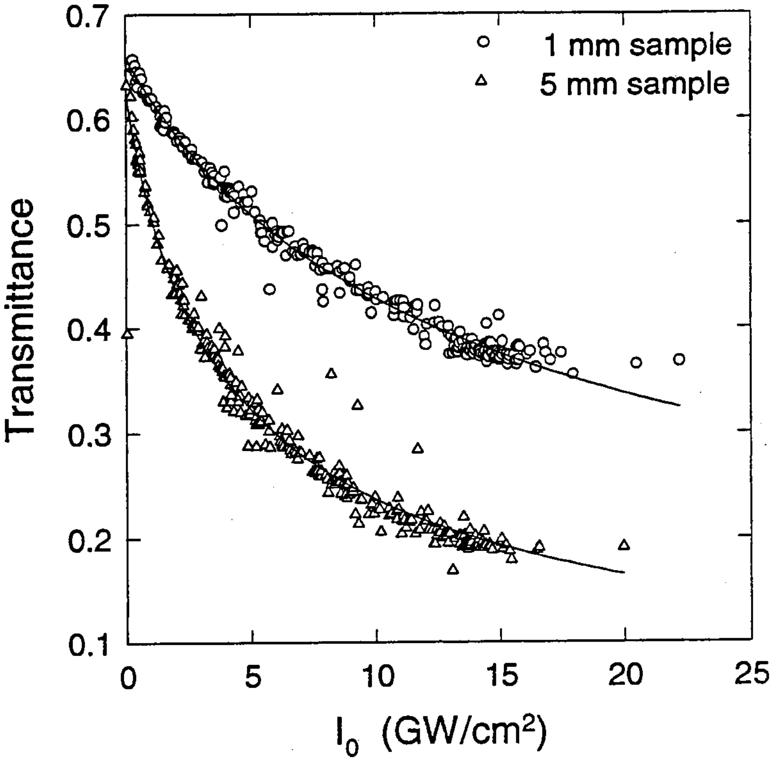

Figure 42. Transmission of light versus input intensity for BGO3 crystal. The solid line is the fit.

TABLE VIII Physical parameters found for BGO crystals

Sample	Dopant	Thickness	α	R	β
		(mm)	(cm^{-1})	(%)	(cm/GW)
BGO1	----	1	0.30	18	2.6
BGO1	----	5	0.30	17	2.2
BGO2	Al	1	0.12	19	2.3
BGO2	Al	5	0.12	18	1.9
BGO3	Al	1	0.12	19	2.3
BGO3	Al	5	0.12	19	1.9

front surface value used in the above calculations. This results in an under estimation of the value of the two photon absorption coefficient for the thicker samples.

ii) Various nonlinear processes which are observable at high input irradiance, such as absorption by the two photon generated free carriers, were ignored. These effects reduce the total transmission coefficient and are less significant in the depth of the crystals where a part of the incident laser light has already been absorbed. Thus, the thinner samples demonstrate a greater decrease per unit length in the transmission coefficient which can be interpreted as an enhancement of the TPA coefficient.

It is thought that the observed dependence of the TPA coefficient on the crystal thickness is due to a combination of the above effects. Such behavior has also been observed in BTeO crystals. In those experiments, the free carrier absorption was monitored and a 3% decrease in the transmission coefficient was found for a 1.2 mm sample while a 4.4 mm sample exhibited a 5% decrease. The nonlinear nature of the thickness dependence of the free carrier absorption in the BTeO crystals suggests that the thickness dependence of β is primarily due to the free carrier absorption rather than self defocusing mechanism. Regardless, for any given sample thickness it can be seen that the Al doping (BGO2 and BGO3) slightly reduces TPA coefficients. It is also of interest to note that the effects of the Bi-Ge Stoichiometry were not quantified by the numerical values of the TPA coefficients.

Photorefractive Properties

SBN (picosecond and Femtosecond)

experimental. In the FWM experiment a single pulse was split into two parts of equal energy (hereafter referred to as 'write' pulses) which were focused such that they overlapped spatially and temporally in the sample ideally producing a spatially harmonic interference pattern. The angle between the paths of the pulses was 3.2° measured in air. A low power, cw He-Ne laser aligned at the Bragg angle for maximum diffraction from the grating was also focused in the sample. The beam geometry and crystal orientation was the usual photorefractive configuration used for FWM studies in SBN[109], i.e. the π-polarized He-Ne laser beam was crossed in the sample with the two σ-polarized write beams which were oriented with respect to the crystal such that they produced a grating wavevector that was parallel to the c-axis (see Fig. 43). To improve the signal-to-noise ratio the probe beam propagation direction was aligned out of the plane containing the write pulses. The diffracted beam was detected using a photomultiplier tube with a rise time of approximately 2 ns and a digital storage oscilloscope. An interference filter at the He-Ne laser wavelength was used to ensure that no stray light from the pulsed laser entered the photomultiplier tube.

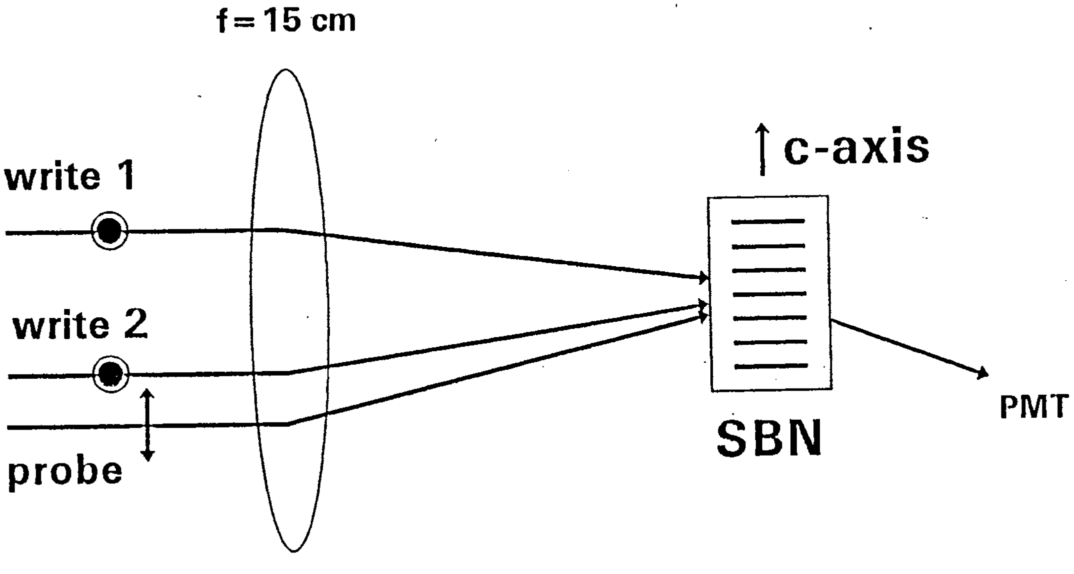

Figure 43. Beam geometry for FWM experiments. π-polarized cw He-Ne probe beam and σ-polarized subpicosecond (λ = 580 nm) or picosecond (λ = 532 nm) write pulses.

results.

Picosecond-pulse excitation With excitation pulses of 20 ps duration and 532 nm wavelength there were two distinct temporal features seen in the FWM signal for both samples. Typical data obtained for the undoped sample are shown in Fig. 44. After the initial unresolved build-up the first decay of the FWM signal is in

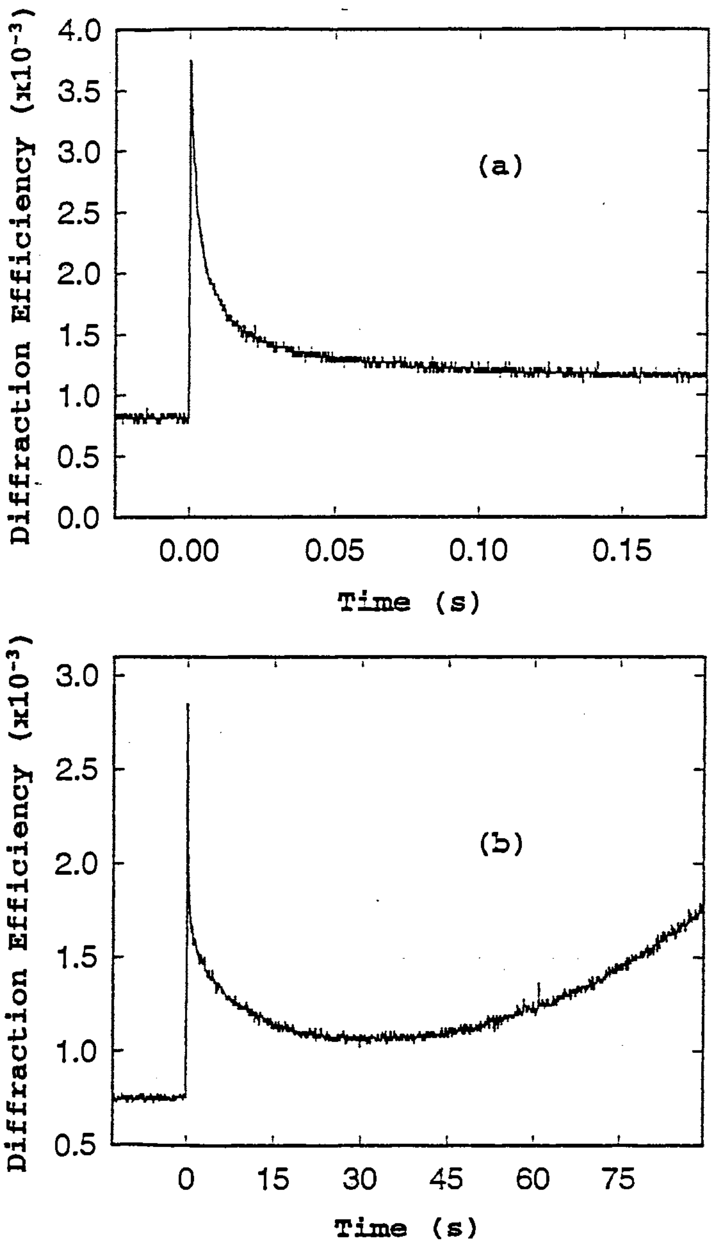

Figure 44. FWM signal following picosecond excitation in SBN:60 with write beam energies of (a) 47 μJ and (b) 46.4 μ J.

the 100 ms time scale. This was followed by a comparatively slow rise that reaches its maximum after a few minutes (Fig. 44(b)). In the case of a total write beam energy of 78 μJ the second rise is complete in approximately four minutes and decays to half the peak height, in the continuous presence of the He-Ne laser, after another fifteen minutes.

Typical FWM data obtained using the Fe:SBN sample are shown in Fig. 45. Similar to the signal from the undoped sample, there exists two stages to the signal in the time frame studied, however the time scales associated with them are very different. The decay of the first signal is complete in less than 25 ms and is followed by a rise of the second signal that is complete in less than 20 seconds. For pulse energies lower than those shown in Figs. 45(a) and 45(b), e.g. Fig. 45(c), the detected signal is observed to drop below the background level in the time regime just after the first signal decay. This means that there must be a process that had decreased the total amount of background light that is randomly scattered from the sample to the detector. For both samples the cross-sectional area of interaction for the two write pulses was 2.7×10^{-5} cm^2.

Subpicosecond-pulsed excitation In a manner similar to that which was seen using the ps pulses, excitation using 400 fs, 580 nm pulses produces two temporal features to the diffracted signal in the time scale of interest in these experiments. Typical data for the undoped sample are shown in Fig. 46. The first feature in Fig. 46(a) is a peak that has a rise time of 300-600 ns which is time resolved in Fig. 46(b). The initial spike in the data seen in Fig. 46(b) is due to gratings formed on the time scale of the temporal overlap of the two write pulses and is not of interest in this work. This signal decays into the microsecond time scale where it competes with the rise of the second signal. The time constants associated with the second peak depend strongly upon the intensity of the write pulses. It has been observed to last as long as thirty seconds or as short as few hundred milliseconds.

Experiments on the Fe-doped samples were not performed using the subpicosecond laser system.

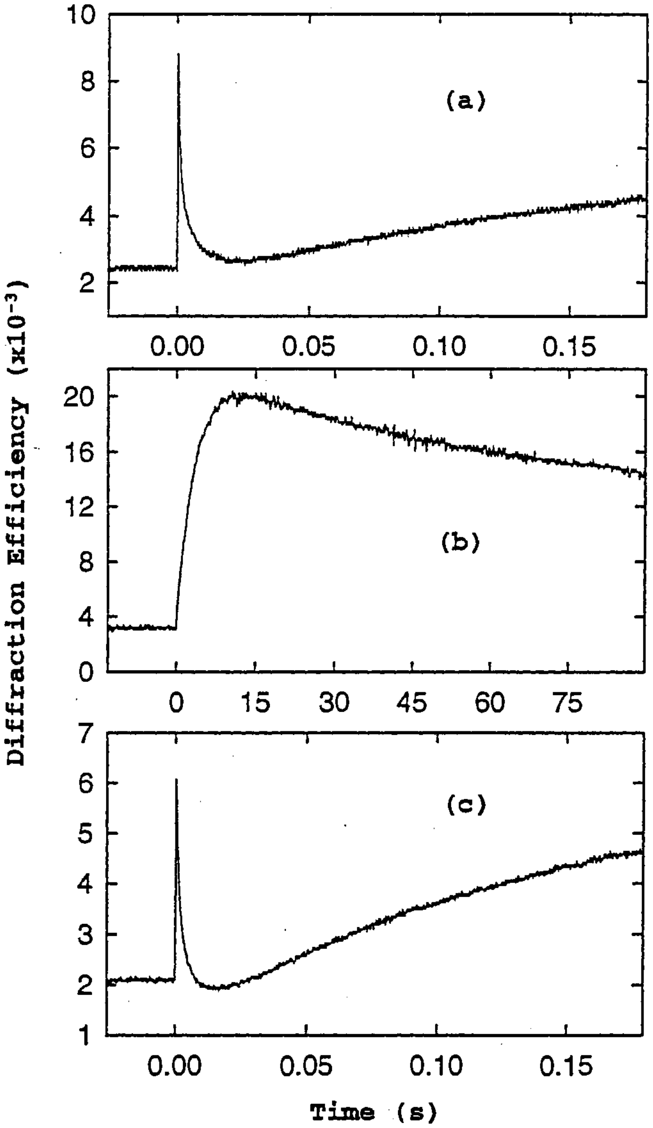

Figure 45. FWM signal following picosecond excitation in SBN:60 with write beam energies of (a) 42.8 μJ (b) 50 μ J and (c) 18.5 μ J.

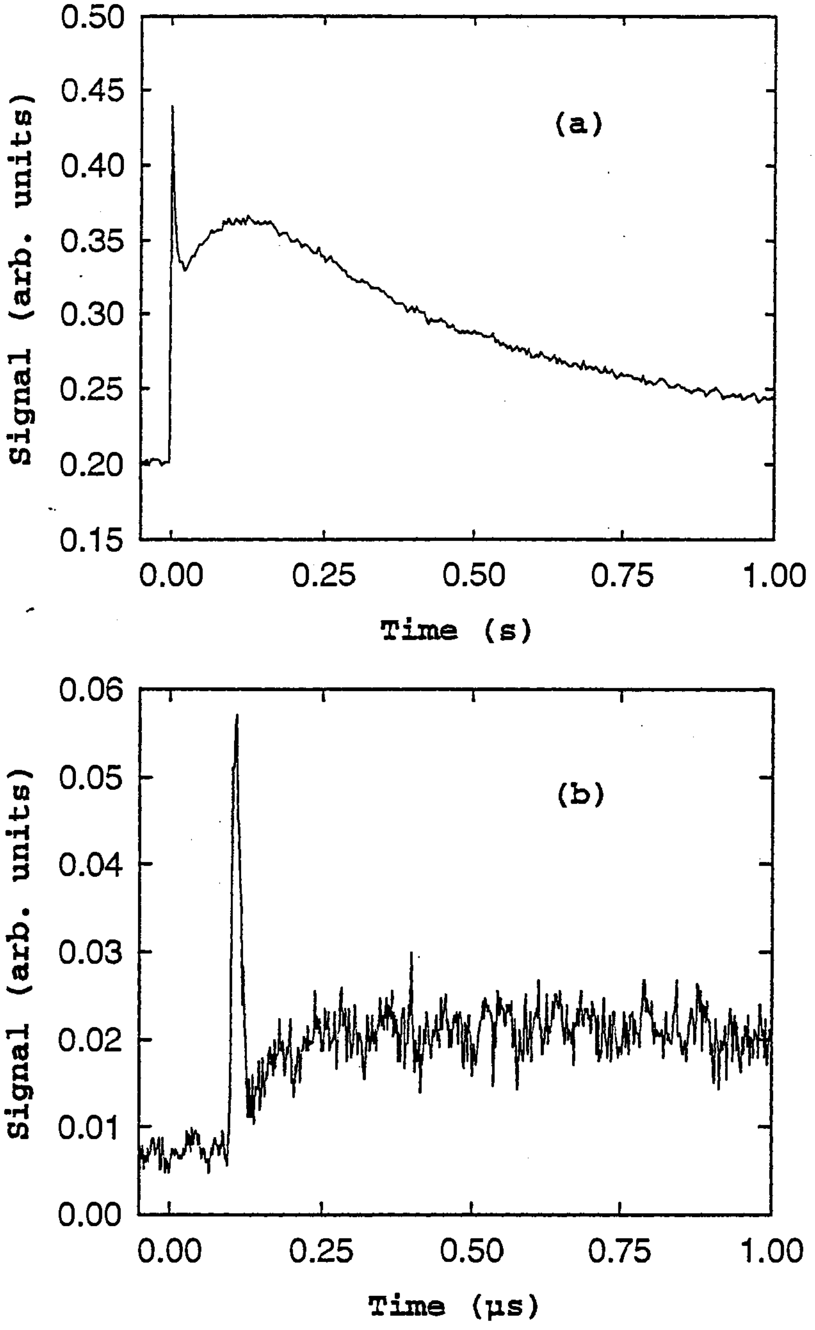

Figure 46. FWM signal following subpicosecond excitaion in SBN:60 in the time scale of (a) seconds and (b) microseconds.

discussion. The first signal in both the picosecond and subpicosecond experiments is associated with scattering from a grating that is set up by an optically induced absorption change in the bright regions of the interference pattern of the two write pulses. In order to demonstrate that intense light at both 580 nm and 532 nm induces absorption at 632.8 nm in SBN:60, one of the write pulses and the He-Ne laser were crossed in the sample and the transmitted He-Ne laser beam was monitored with the same detection scheme as discussed above for FWM. The results of the experiment using the picosecond and subpicosecond laser are shown in Figs. 47(a) and 47(b), respectively. In both cases, the time dynamics of the induced absorption are the same as those of the first signal in the FWM experiments. This suggests that, for the time scales associated with the first peak in the FWM signals, an absorption grating dominates any contribution from a photorefractive index grating.

This experiment was carried out using the iron-doped sample as well and, within our model of induced absorption, since the FWM signal decays more rapidly in this sample it would be expected that the induced absorption decays faster as well. On the contrary, however, the induced absorption experiment showed that the depletion lasted longer (see Fig. 48). This observation helps explain why the decay of the FWM signal is followed by a drop in the signal below the background level for total write pulse energies less than $\sim 40\ \mu$J (not observed at higher intensities because the rise of the second peak begins earlier for increasing intensities and competes with the decay of the first signal). A comparison of the time scales for both experiments in Fe:SBN reveals that the levels responsible for the induced absorption remain populated following the decay of the absorption grating. The grating decay rate is then associated with the rate at which the absorbing level in the dark regions of the interference pattern are populated. This action decreases the contrast ratio of the grating and therefore the diffracted signal. It is this spatially uniform residual absorption that decreases the amount of randomly scattered light that reaches the detector and causes the signal to drop below the background level. Since the absorption grating signal in the undoped sample follows the decay

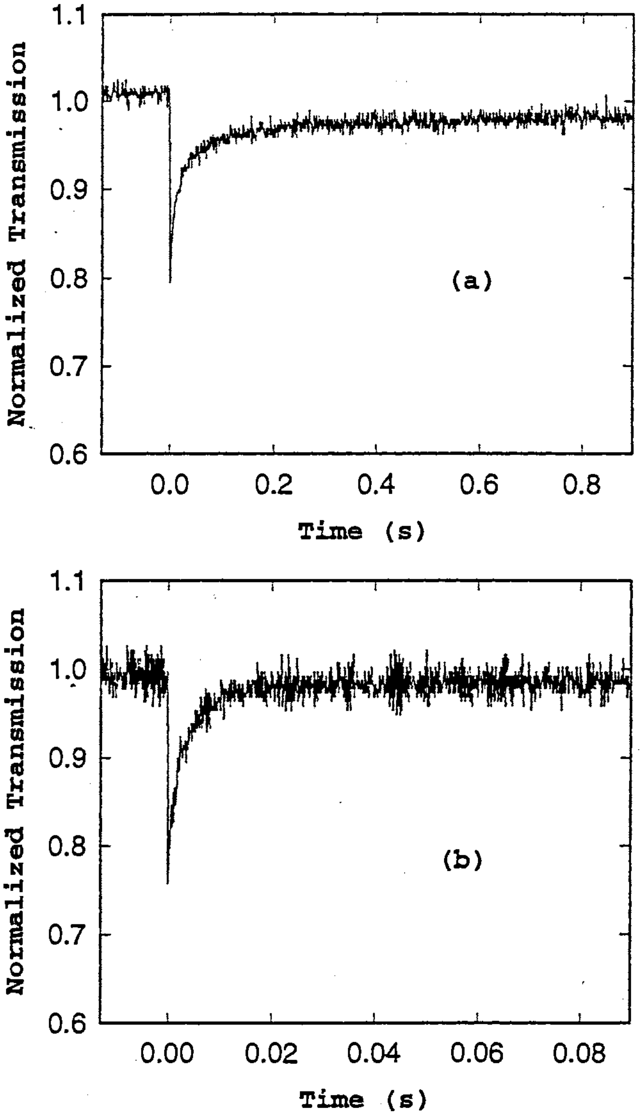

Figure 47. Probe beam depletion following (a) 46.1 μJ picosecond excitation and (b) 1.1 μJ subpicosecond excitaion.

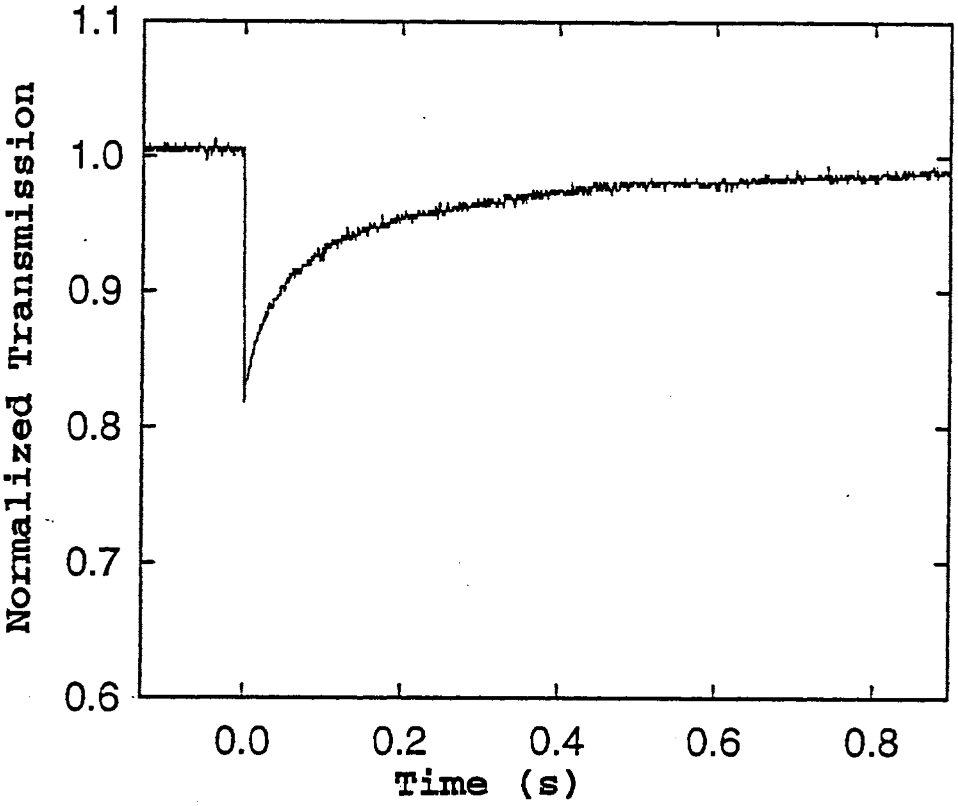

Figure 48. Probe beam depletion following 41.4 μJ picosecond excitaion..

of the absorption, the difference in signal behavior can most likely by attributed to increased carrier mobility associated with iron-doping. Increased mobility is supported by the observation that the photorefractive signal develops an order of magnitude faster in the iron-doped sample.

Kogelnik[12] presented the coupled wave solution for diffraction from thick absorption gratings. With the probe beam incident at the Bragg angle and having its polarization parallel to the plane of incidence, the diffraction efficiency for such a grating is given by[12]

$$\eta = \exp(\frac{-\alpha d}{\cos\theta_0})\sinh^2(\frac{\alpha_1 d\cos(2\theta_0)}{4\cos(\theta_0)}) \tag{136}$$

where α_1 is the average value of the absorption change, d is the interaction length, and θ_0 is the Bragg angle measured inside the crystal given by $\theta_0 = \sin^{-1}(\frac{\lambda_p}{2\Lambda n})$ (isotropic diffraction). λ_p is the vacuum wavelength the probe beam (632 nm), $\Lambda = \lambda_w/2\sin\theta$ is the grating spacing with $\lambda_w \equiv$ write laser wavelength and $\theta \equiv$

crossing angle measured inside the crystal, and n is the dark index of refraction of the crystal. Using the results of the induced absorption experiment where no grating is present, $\alpha_1 d$ is Eq. 136 can be calculated for a given value of incident pulse intensity

$$\alpha_1 d = -Ln(\frac{I_d}{I_a}), \tag{137}$$

where I_d is the depleted value of the He-Ne transmission intensity following the strong pulse and I_a is the He-Ne transmission intensity in the absence of the strong pulse. Since in FWM experiment, the peak intensity in the bright regions of the interference pattern is given by $I=I_t(1+m)$, where m is the modulation index of the grating and I_t is the total intensity of the write pulses, we can estimate the expected contribution of the absorption grating to the total experimental efficiency. The result is that the diffraction efficiency observed can not be fully accounted for by Eq. 136. With the large values of the induced absorption produced, a contribution from the unshifted refractive index grating (according to Kramers-Kronig relation) is needed. For the lowest values of the write intensities used, the diffraction efficiency using SBN approaches that predicted by Eq. 136. However, using the Fe-doped sample, the signal is an order of magnitude larger.

With the experiments described thus far it is not possible to determine the physical mechanisms responsible for the induced absorption. It is proposed that the induced absorption is a result of the population of an impurity or defect site that did not have significant population before excitation. Further, it is thought that significant population of this level is realized with the aid of a large number of two photon band-to-band transitions followed by trapping at the site(s) that absorb near 632 nm. The TPA coefficient at 532 nm, as discussed in the previous section, is 2.3 cm/GW for undoped SBN:60. With an intensity of 2.5 GW/cm^2 the intensity depletion of a laser beam due to TPA is more than an order of magnitude greater than that due to the linear absorption. Below this value of intensity the transient probe beam depletion becomes an unmeasurable effect with our detection system. After excitation the free carriers populate an absorbing level at a rate that is roughly inversely proportional to the rise time of the induced absorption. As discussed the primary physical mechanisms leading to the decay of the grating are different for the two samples. For undoped SBN:60 the decay is thought to be primarily due to the depopulation of the absorbing level either through recombination or trapping at other site(s) that do not absorb at 632.8 nm.

The subsequent rise of the diffracted signal after the decay of the absorption grating is explained as due to the usual charge displacement photorefractive effect[110]. It can only be observed when the beam geometry is such that photorefractive effects are possible. At this time the mechanism of charge transport as well as the sign of the charge carrier is not apparent. In cw FWM experiments electrons have been found to be the dominant carrier[103]. However, competition from holes cannot be ignored in the pulsed regime because the direct band-to-band transitions that are associated with nonlinear absorption create a large number of holes. Their contribution to the grating depends on their relative mobility with respect to the electrons. The physical processes leading to the photorefractive index grating are currently under investigation.

Bi_2TeO_5 (picosecond)

experimental. Single crystals of Bi_2TeO_5 were grown by Czochralski method in the Research Laboratory for Crystal Physics, Budapest, Hungary. The details of material preparation and crystal growth can be found in ref. [90]. For the present experiments undoped, Cr-doped (10^{-4} mole/mole), and Fe-doped (5 x 10^{-5} mole/mole) samples were used. The Cr and Fe impurity concentrations of the undoped Bi_2TeO_5 crystals were 1.0 x 10^{-6} and 1.2 x 10^{-5} and mole/mole, respectively. These built-in dopant concentrations were determined by Atomic Absorption Spectroscopy.

In the pulsed four-wave mixing experiments, a Quantel International Model YG571c Q-switched and mode locked Nd:YAG laser was used as the excitation source. Each frequency doubled (λ =532 nm) pulse had an energy of 18 mJ/pulse, duration of about 18 ps with a repetition rate of 10 Hz. The two write beams were crossed in the sample at various angles creating gratings in the [010] crystallographic direction. The σ-polarized probe beam was either a third weak component of the Nd:YAG laser pulse, or the 632.8 nm cw output of a He-Ne laser. In the first case (degenerate FWM) an optical delay line was used in the probe beam path to follow the evolution of the diffracted signal beam in the time range from 100 ps before to 2 ns after the write pulses. The diffracted signal was detected by a photodiode and analyzed by a boxcar signal averager. When the cw He-Ne probe beam was used, the scanning mode of the boxcar signal averager provided the time evolution of the diffracted signal. In most of the photorefractive measurements the cleaved (100) surface was exposed to the incident laser beams. Throughout this section we use the orientation convention introduced in ref. [106].

results. Figure 49 shows the FWM diffraction efficiency as a function of the probe beam delay for different Bi_2TeO_5 samples. The time evolution of the FWM signal from Bi_2TeO_5 crystals, using 18 ps pulses for write and probe beams, is similar to those published for other photorefractive oxide materials using similar experimental conditions [111,114–117]. Each curve in Fig. 49 consists of a sharp peak positioned at 0 ps delay and a decaying part with a superimposed damped oscillation covering the time scale from about 20 ps to 2 ns. The basic character of the time evolution is the same for the undoped and doped Bi_2TeO_5 samples. Slight differences have been observed in the absolute signal intensity and the lifetime and relative intensities of the three contributing signal components in the different samples.

The time evolution of the FWM signal in the microsecond to millisecond range is shown in Figure 50. These data were obtained by using 18 ps write pulses and a cw probe beam for detection . The FWM diffraction efficiency for undoped Bi_2TeO_5 shows a continuous decrease up to about 50 μs, then a slight increase was observed between 50 μs and 1 ms, followed by another decaying region. The rate of decay for the microsecond range signal is 0.033 μs^{-1} while for the millisecond

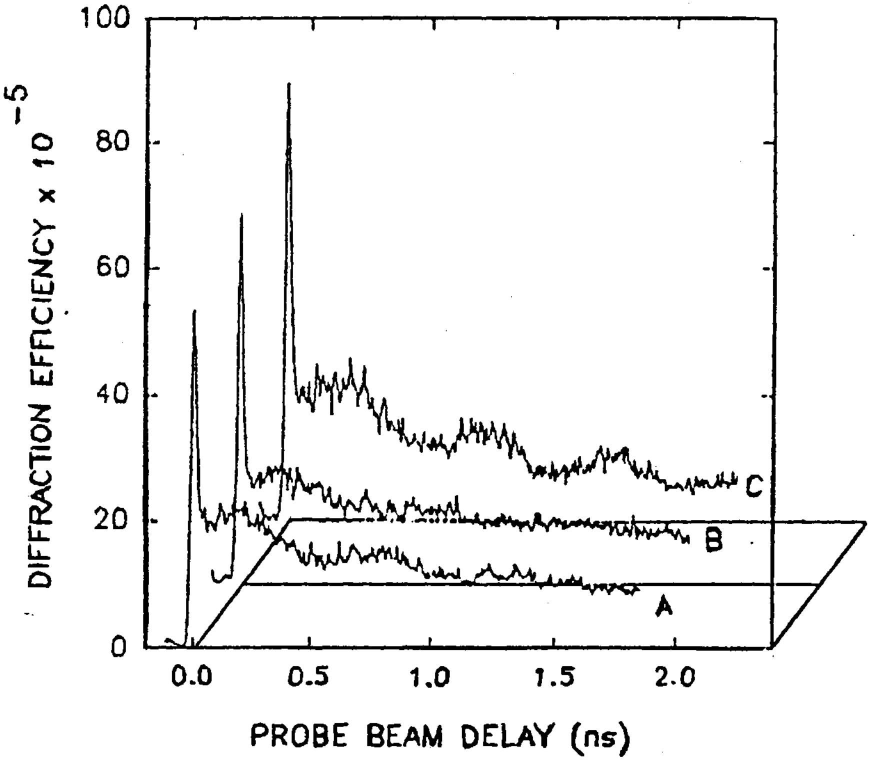

Figure 49. The time evolution of the FWM signal in undoped (curve A), Cr doped (curve B) and Fe-doped (curve C) Bi_2TeO_5.

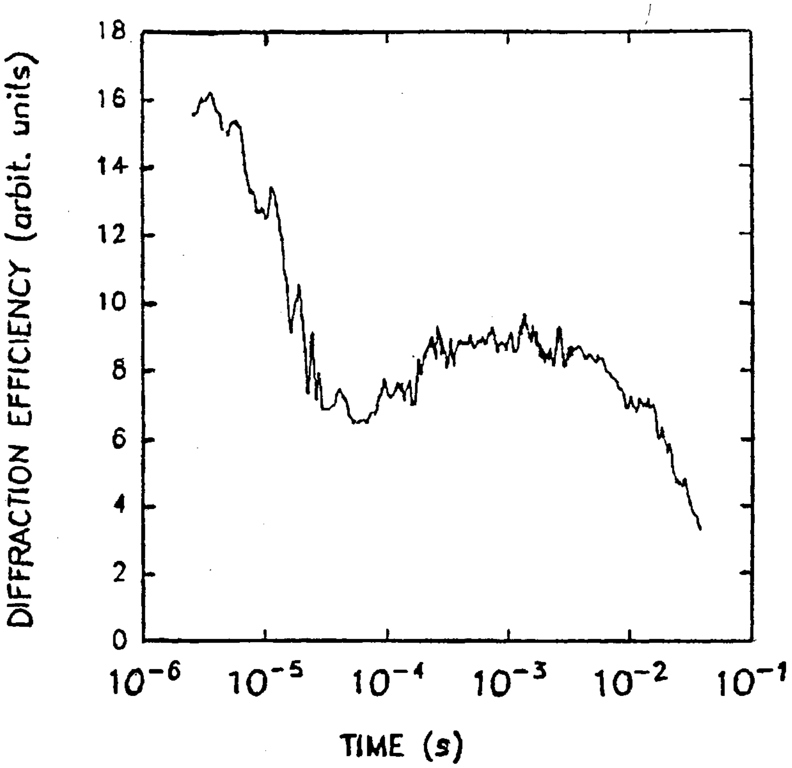

Figure 50. The time evolution of FWM signal from microsecond to millisecond time regimes.

range signal it is 0.026 ms^{-1}. The latter decay rate is in good agreement with the data obtained in the previous CW FWM experiments [101].

discussion. The CW FWM experiments on Bi_2TeO_5 have shown strong photorefractive signal with multicomponent decays [100]. Excited state population grating, refractive index modulation due to the space charge induced electro-optic effect, and a contribution due to ion displacements are identified in the photorefractive process [100]. In the Cr-doped samples, an absorption grating was also detected. The relatively low saturation limit of the observed FWM diffraction efficiency indicates that the photorefractive effect in undoped Bi_2TeO_5 crystals is limited by the charge carrier or charge trap concentrations [100]. This saturation limit is increased by using Fe or Cr dopants in both CW and short pulse induced FWM [100,102].

The characteristic feature of the fast photorefractive response of the crystal have already been analyzed for undoped Bi_2TeO_5 [102]. The detailed analysis based on the dependence of the FWM signal on the write beam intensity, write beam crossing angle, crystal orientation, write- and probe beam polarization [102]. The laser excitation process was also investigated and significant two-photon absorption was observed [102,118].

The interaction of the laser beams with bound charges is the major contribution to the sharp peak at 0-delay. This signal component decays in the picosecond time scale. There is an additional component to the instantaneous signal due to the creation of free carriers. This component persists as long as the free carrier lifetime or the time it takes for the carriers to diffuse to the dark regions of the light interference pattern. The free carrier grating is considered as the main contribution to the signal component decaying in the few nanosecond time scale [102]. The damped oscillatory modulation of the nanosecond FWM signal is attributed to the generation of acoustic phonons by the laser pulse impact. The compression due to the acoustic phonons moves along the refractive index grating and its contribution to the refractive index grating created in the FWM processes is periodically constructive and destructive [102].

The Fe and Cr dopants do not modify the basic character of the FWM signal induced by short laser pulses significantly. However, the amplitude of all three signal components discussed above are larger for the doped crystals than for the undoped one. Also, the damping of the phonon induced oscillations different for the doped and undoped crystals. The decaying factor of the oscillation was found 0.89 ns^{-1} for undoped Bi_2TeO_5 samples under the standard experimental condition, while this factor is 1.24 $ns^{-1}$for the Cr-doped and 0.49 $ns^{-1}$for the Fe-doped samples.

The interpretation of the longer lived FWM signals decaying in the microsecond and millisecond range is more difficult. It was shown for $BaTiO_3$ and $Bi_{12}SiO_{20}$ that the intense short pulse induced FWM signals, decaying in this time interval, are associated with electro-optically induced, phase shifted gratings [111,119,120]. The build-up of the photorefractive grating is much faster in the pulsed writing than in the CW writing process. This was attributed to an enhanced diffusion of the charge carriers in the former case. Two models have been developed to explain tis fast diffusion. In the model of ref. [121] the charge recombination time is short compared to the pulse length, and consequently only the high fluence of the pulsed beams can saturate the charge number density. Under these conditions the diffusion rate is modified. The other explanation is a saturation of the charge traps due to the high irradiance of the write beams. This increases the effective trapping time of the charge carriers [119].

A signal decaying in a few tens of milliseconds has already been identified in the CW FWM measurements of Bi_2TeO_5 and attributed to an impurity related excited state population grating [100]. In those measurements the write beam intensity was smaller by orders of magnitude than that of the present pulsed write beams and only one photon excitation was considered. Consequently, the displacement of the excited charge carriers was only in its initial stage and the unshifted component due to excited state population grating was predominant in the millisecond time regime after CW writing [100]. In the 18 ps pulse writing process, however, the free charge carriers are generated in large numbers by two-photon excitation and, according to the models discussed above, they may be spatially shifted before recombination or trapping occurs. A small shift of the charge carriers appears to occur even on the nanosecond time scale [102].

The FWM signal components decaying in microsecond and millisecond range may be related to the presence of shallow traps as has b been shown to be the case for other photorefractive crystals. In several oxide crystals impurity ions have been found to provide these shallow levels. Since a small concentration of iron impurities (about 20 ppm) is in the undoped Bi_2TeO_5 crystals, the iron ion electron levels are possible options as the source of the shallow traps in this material too.

A thermal excitation of the shallow traps and a subsequent re-trapping leads to a long range migration of the charge carriers with a trap-modulated mobility. In this way the contribution of the phase shifted grating becomes more and more dominant in the signal at longer times as was observed in the CW FWM measurements [100,101]. The CW FWM experiments have demonstrated the existence of a variety of different charge carrier traps and the deep traps are responsible for the longer time scale signals (seconds to minutes) [100,101]. The space charge field generated in the photorefractive process also leads to ionic displacements in Bi_2TeO_5. Oxygen ions can easily be shifted in the space charge field since there are large number (~18%) of open oxygen position in the crystal structure [67].

The build-up of the phase shifted photorefractive signal component is significantly faster with the 18 ps writing pulses than it was observed for the CW writing process which was investigated earlier [100,101]. The faster build-up of the phase shifted grating in short pulse writing experiments compared to the CW write process, also leads to a faster build-up of the long lived FWM component (>2 years) which was attributed to the displacement of oxygen ions [100,101].

Another possible contribution to the signal on the microsecond-millisecond time scale is a thermal grating. Since the thermal properties of Bi_2TeO_5 crystals have not been investigated this possibility can not currently be evaluated.

The most interesting character of the time evolution of the FWM signal is the local maximum in the ms time range (Fig. 50). This indicates a rearrangement in the photorefractive grating during the time evolution. A mathematical modeling is in progress to distinguish among the possible options. Simultaneous presence of unshifted and phase shifted gratings, absorption and refraction index gratings as well as their decay and transfer to each other is considered.

Conclusions

The experiments performed on different photorefractive crystals in pico and femto second time regimes resulted in TPA coefficients of a few cm/GW. In pulsed experiments, intensities of up to 5 GW/cm^2 are easily attainable. In these cases the two photon absorption can exceed the single photon absorption by up to two orders of magnitude. In such cases the electron generation is dominated by TPA. Since the scattering efficiency in a FWM experiment on these samples, dictated by their photorefractive behavior, depends on the number of generated carriers, an increase in the efficiency and response time can be expected if short pulse excitation is used. The limit on the efficiency, then, is dictated by the trapp density and not the generation rate.

Single picosecond and subpicosecond light pulses were used in independent experiments to induce refractive index gratings in SBN:60 and doped Bi_2TeO_5. In SBN crystals, the time evolution of the gratings appear to have at least two stages which are responsible for two distinct peaks in the FWM signal. The first peak is associated with induced absorption at the probe wavelength. In a single beam experiment, where no grating was present, it was shown that significant probe beam depletion is seen following intense excitation. This depletion is explained as induced absorption due to the population of an impurity or defect site and is associated with the first peak in the FWM signal because the time scales of the two phenomena overlapped. The second peak is explained as resulting from a grating due to a charge displacement photorefractive effect. It can only be observed when the beam geometry is such that photorefractive effects are possible.

In Bi_2TeO_5, the effect of dopants was investigated on the fast decaying photorefractive signal components (<2 ns) of Bi_2TeO_5. It was found that Cr and Fe doping resulted in only a moderate gain in the diffraction efficiency. This is unusual for oxide crystals where dopants generally increase the FWM signal by orders of magnitude, especially when combined by appropriate treatments to get the optimum ratio of empty traps and charge carrier source [122,123]. The dominant FWM signal components in the microsecond to seconds regime was attributed to electro-optically induced, phase shifted gratings involving impurity related traps with several different trap depths. The fast development of the real photorefractive signal is consistent with enhanced charge diffusion due to the higher density of free carriers created by the 18 ps laser pulses.

CHAPTER VI

RARE-EARTH DOPED GLASSES

Introduction

The last class of materials that has generated interest as possible memory storage materials are rare-earth doped glasses. Unlike the materials studied in the previous chapters, glasses are random structure with no translational symmetry. Much like the photorefractive crystals they are insulators, but unlike them the bonding between its various constituents is primarily covalent. The role of an ion in a glass is categorized as either network former (F) or network modifier(M). The network formers participate in the covalent bonding that compose the structure such as SiO_2, GeO_2. Presence of the modifier ions breaks the covalent bonding by competing for the shared electrons in the bonds. It has been shown that the role of an ion in the structure can be determined from its charge-to-radius-squared, Q/r^2 value. In particular, atoms with a large Q/r^2 display covalent bonding and as such behave as network formers. As the value for Q/r^2 decreases, the bonding becomes more ionic and the ion becomes a network modifier. In oxide glasses studied here the oxygen is the bridging atom with a large Q/r^2 ratio. Addition of the network modifiers such as Na^+ breaks the covalent bonding between oxygen and its adjacent atoms turning the oxygen into a non-bridging oxygen. These free radicals have a very strong response to an incident electromagnetic wave and are dominant contributors to the glass' dielectric function. Ions with closed outer shell electrons, such as rare-earths, display interatomic transitions in addition to acting as a modifier ion. Excitation of these atoms through interatomic transitions can alter the dielectric function of the glass. most of these alterations are transient, however permanent index changes have been reported previously in rare-earth doped phosphate and silicate glasses [124–130]. These gratings were produced using four-wave-mixing (FWM) techniques and resonant excitation of the trivalent rare-earth ions into excited states that undergo efficient radiation less relaxation. The transient component of the grating was attributed to a population grating of the rare-earth ions and a model based on a thermally induced change in the local glass structure at the site of the rare-earth ions was proposed to explain the formation of the permanent gratings [124–130].

The conventional view of glass as a structural network with modifying ions dispersed in the interstities can provide the essentials of this model if some of these ions have the ability to change their positions. In phosphate, silicate, germanate, and borate glasses the rare-earth (RE) dopant ions are in network-modifier positions, surrounded by nonbridging oxygen ions [131–135]. When the excited RE ions relax nonradiatively several high energy vibrational modes are created. The local heating associated with these vibrational modes produces a change in the structure of the local environment of the RE ions by causing the ions in that region of the material to move from one configuration to another. This leads to double-minima potential wells for the configuration coordinates of the RE ion electronic energy levels. The mechanism for switching the host ions between two equilibrium positions requires structures with high frequency local vibrational modes such as those associated with structural defects (lateral or nonbridging groups of ions) and further requires that the RE ions are strongly coupled to these vibrational modes[125]. The two-potential-well-model (TPWM) also assumes that the index of refraction of the material changes depending on which structural configuration is present.

There are still important questions to be answered concerning the exact nature of the local structural change in the glass and the origin of the refractive index difference for the two configuration. In order to answer these questions information is required as to how the chemical composition of the glass alters the characteristics of the permanent refractive index gratings produced. Also important is learning how to either optimize or minimize the production of these gratings. This is critical in understanding the general phenomenon of laser-induced index changes that have been observed in both bulk and fiber materials[136], since this effect can form the basis of important optical devices or can be detrimental to optical transmissions. With this in mind, this paper extends the previous work to include new types of lithium borate, lead silicate, lead borate-germanates, and lead germanate glasses. The results of this work are combined with the previous results on phosphate and silicate glasses to understand the effects of the chemical composition of the glass on its ability to produce gratings with high scattering efficiencies.

Experimental Results

LIG's in lithium-borate glasses

To determine the effects of different glass modifier ions on the ability to produce gratings with high scattering efficiencies, six Eu^{3+}-doped lithium-borate glasses (LiB) were investigated. These had identical compositions except for one modifier ion which was changed through the series of metallic elements: Mg, Ca, Ba, Zn, Al, and Pb. These glasses were selected since: (i) the general optical properties of Eu^{3+}-doped glasses have been previously analyzed[133], (ii) in the range of B_20_3 mole % used in these samples it is assumed that only fourfold coordinated boron atoms exist[137,138], and (iii) previous experiments have demonstrated permanent laser induced gratings in this type of glass[127]. The compositions of these glasses are listed in Table IX.

Gratings were produced in each sample at room temperature using the technique described previously[124–130]. Crossed beams from an argon laser tuned to the absorption transition of the $^5D_2$ level of the Eu^{3+} ions were used to write the gratings. The scattering efficiencies η of these gratings were measured using the output of a low power He-Ne laser for the read beam. A typical result for the time evolution of the FWM signal is shown in Fig. 51 for the LiB4 glass. In all six LiB glasses the signal builds up slowly in time reaching a maximum in about 30 min. It was observed that in each sample when the write beams were chopped off, the signal beam intensity decayed rapidly to about 70% of its maximum value in

TABLE IX Composition of glass samples

Sample	Network Former (mol %)	Network Modifier (mol %)	Eu^{3+} content (mol %)
LiB1	60.0 B_2O_3	15 Li_2O 20 BaO	5 Eu_2O_3
LiB2	60.0 B_2O_3	15 Li_2O 20 MgO	5 Eu_2O_3
LiB3	60.0 B_2O_3	15 Li_2O 20 CaO	5 Eu_2O_3
LiB4	60.0 B_2O_3	15 Li_2O 20 ZnO	5 Eu_2O_3
LiB5	60.0 B_2O_3	15 Li_2O 20 Al_2O_3	5 Eu_2O_3
LiB6	60.0 B_2O_3	15 Li_2O 20 PbO	5 Eu_2O_3
PbB	67.7 B_2O_3	24 PbO 3.3 BaO	5 Eu_2O_3
PbBGe	40.0 B_2O_3 27.7 GeO_2	24.0 PbO 3.3 BaO	5 Eu_2O_3
PbGe	67.7 GeO_2	24 PbO 3.3 BaO	5 Eu_2O_3
PbSi1	67.7 SiO_2	24 PbO 3.3 BaO	5 Eu_2O_3
PbSi2	57.7 SiO_2	34 PbO 3.3 BaO	5 Eu_2O_3

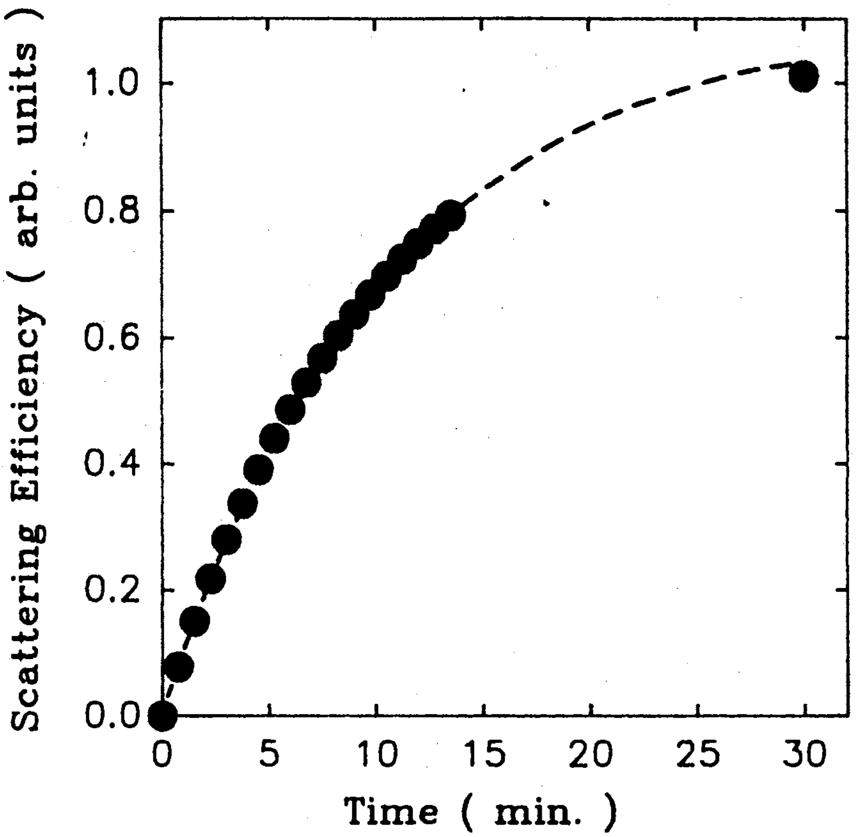

Figure 51. Time evolution of the buildup of the FWM signal in LiB4 sample at room temperature with write beam power of 70 mW.

a time given by the Eu^{3+} ion $^5D_0$ level lifetime. This initial decay was followed by a slow decrease in the signal intensity over a period of about 15 min. In these lithium-borate glasses the signals leveled off at about 40% of their initial values and remained there for several days, the longest period investigated. The results obtained for this time evolution of the signal from the LiB4 sample are shown in Fig. 52.

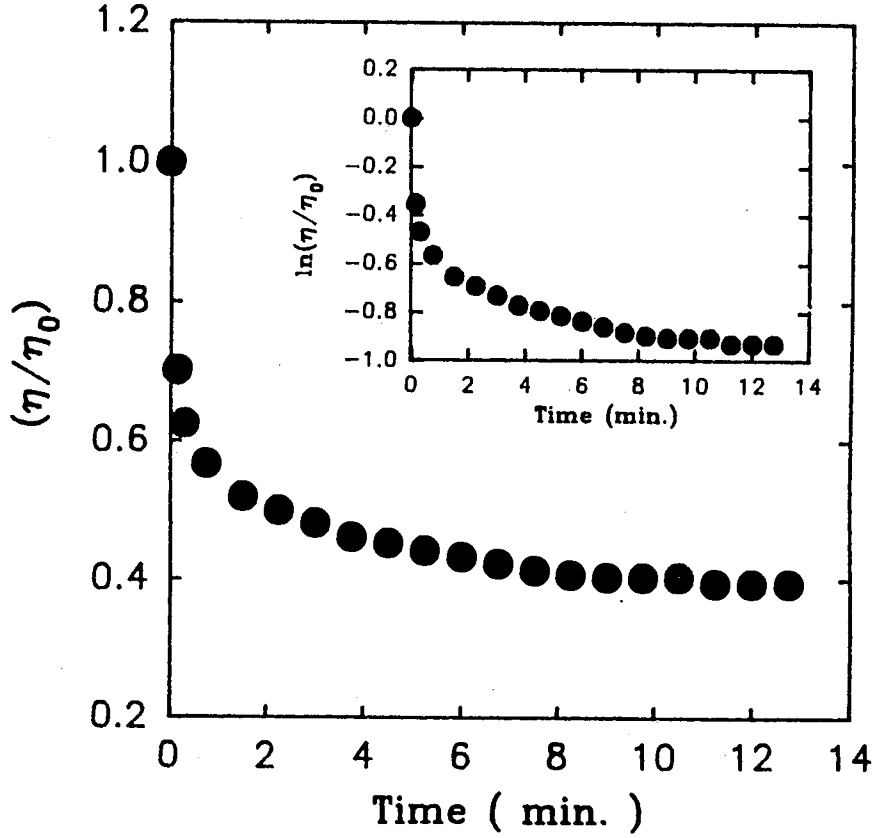

Figure 52. Time evolution of the scattering efficiency of the LIG in LiB4 after the write beams were chpped off..

It was found that the scattering efficiency of the permanent LIG in these LiB glasses was strongly dependent on the nature of the network modifier ions. Previous results from phosphate and silicate glasses also show efficiency changes with different modifier ions[124–130]. Table X lists the values of Q, r, and the mass are for each of the modifier ions used here along with relative values of Q/r^2.

In Fig. 53 the experimental values of the scattering efficiencies are plotted vs

TABLE X Relevant parameters of the modifier ions.

Glass	Modifier ion	Mass ($\times 10^{-24}$ g)	Q	r (Å)	Relative Q/r^2	$SCB_{M\text{-}O}$
LiB1	Ba	120	2	2.8	1.1	90
LiB2	Mg	35	2	2.0	2.0	79
LiB3	Ca	53	2	2.5	1.5	84
LiB4	Zn	76	2	2.1	1.8	66
LiB5	Al	38	3	1.8	3.4	116
LiB6	Pb	147	2	2.3	1.4	131

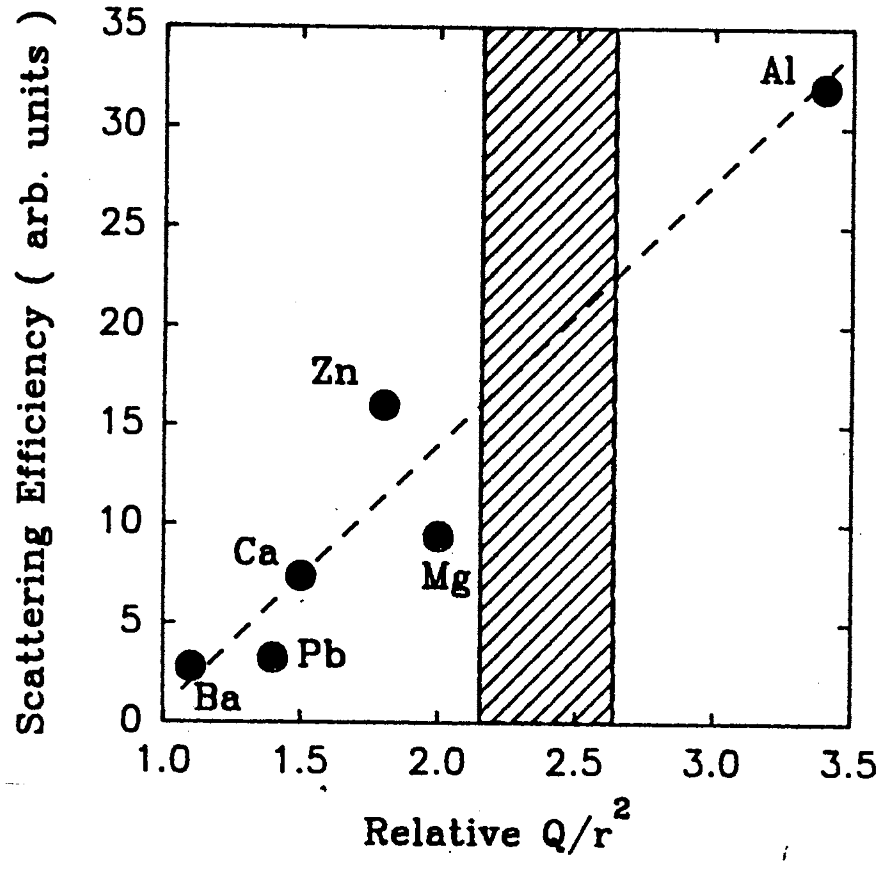

Figure 53. Scattering efficiency of LIG in the LiB samples as a function of $Q/r^2$of modifiers. The area bounded by vertical dashes contains the values of Q/r^2 for rare-earth ions..

Q/r^2 for the samples studied. To illustrate the effects of the mass of the modifier ions, the efficiency is plotted vs the mass for the Group II alkali metals Mg, Ca, and Ba in Fig. 54. Another parameter that is used to characterize different modifier ions is the bond strength between modifier and oxygen ions. The values of the strength-of-the-chemical-bond (SCB_{M-O}) between the various modifier ions and oxygen ions are listed in Table X and the dependence of the scattering efficiency on SCB_{M-O} is shown in Fig. 55. Further discussion of these results is left to a later section.

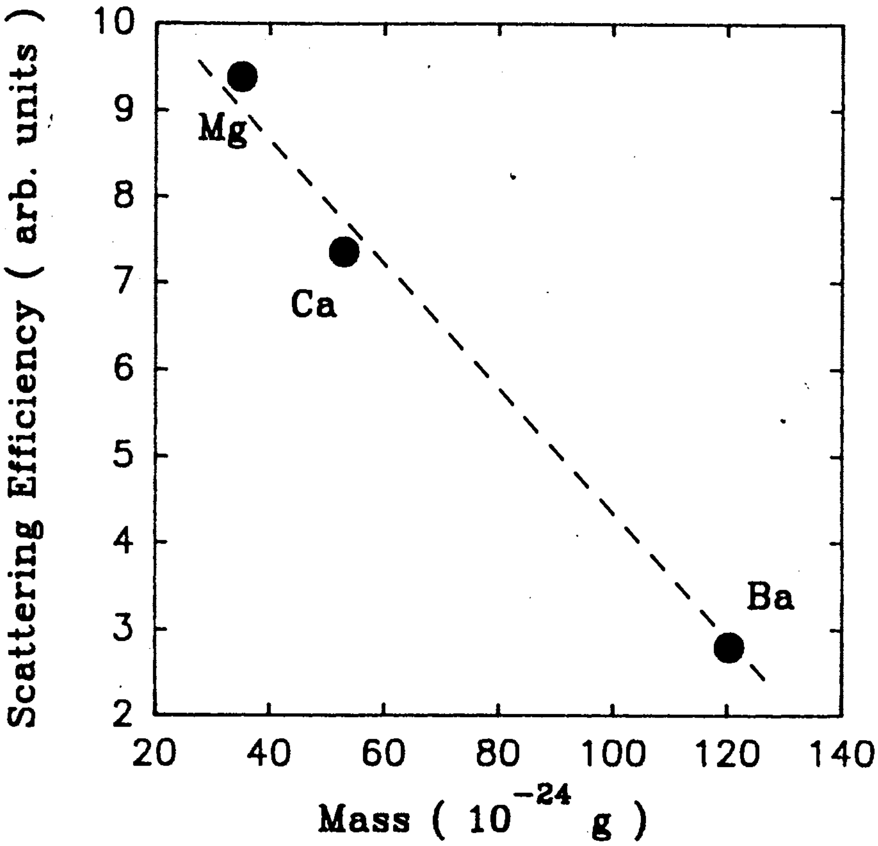

Figure 54. Scattering efficiency of LIG as a function of the mass of the modifier ions created at room temperature in LiB samples containing the Group II modifier ions Mg, Ca and Ba.

Effects of bond-strength and glass composition

Since the strength of the chemical bond between the network former ions and the oxygen ions (F-O) and the relative concentration of the network former and

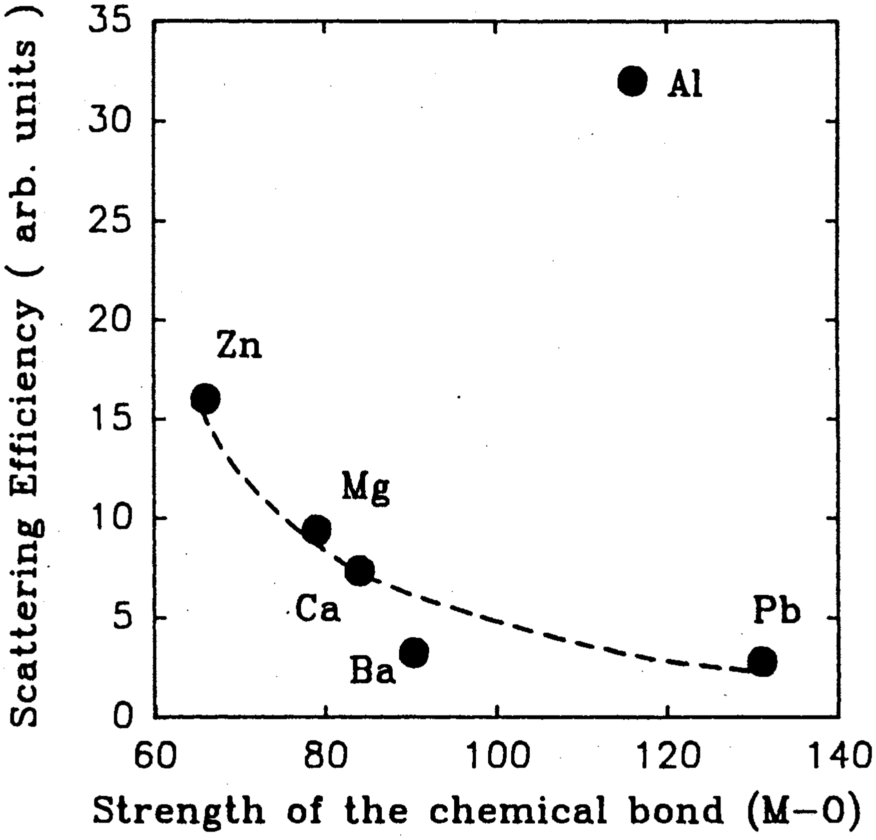

Figure 55. Scattering efficiency of the LiB glasses as a function of the strength of chemical bond between modifier and oxygen ions.

network modifier ions are two important parameters that determine the structure of the glass, five additional glasses were selected to study the influence of these parameters on the scattering efficiency of the permanent LIG. The compositions of these glasses are also listed in Table IX. They were selected since: (i) the strength of the chemical bonding between the network former and oxygen ions, SCB_{F-O}, increases as the network former ion changes with germanate<silicate<borate [139]; (ii) glasses are formed by all compositions in the system B_2O_3-GeO_2 [140]; and (iii) in the range of F_xO_y mole % selected, all of the network former ions are fourfold coordinated [141]. The scattering efficiency of the permanent LIG was found to decrease as the network former was changed to increase the SCB_{F-O} as shown in Fig. 56. In this figure a rule of additivity [142] was employed to estimate the

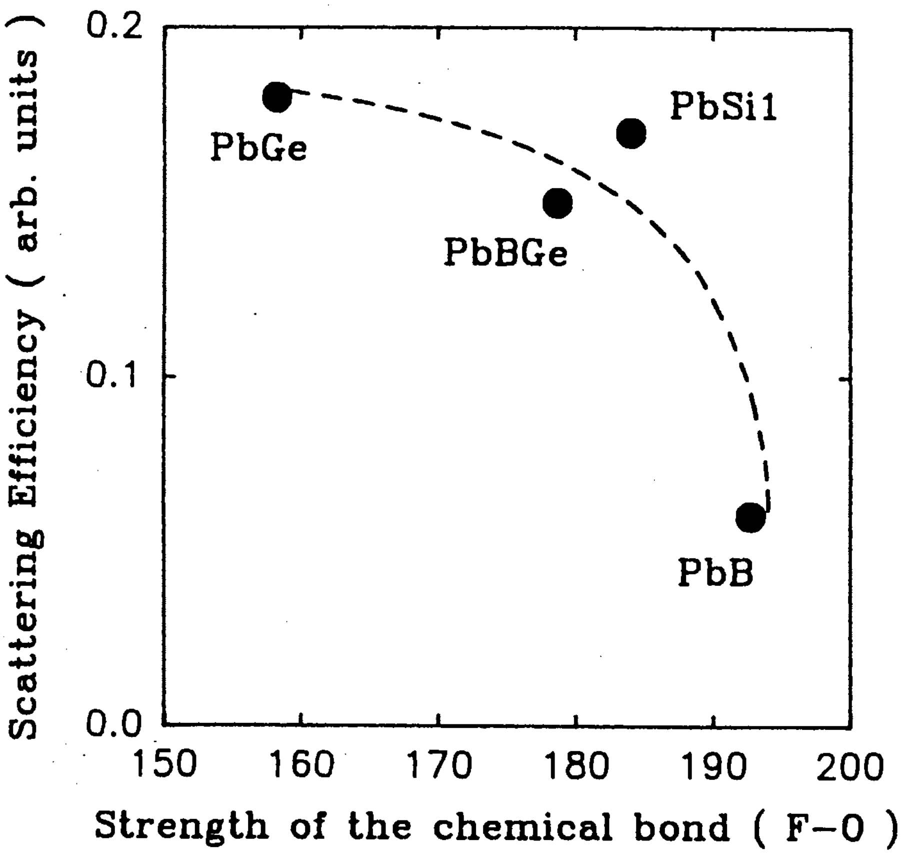

Figure 56. Scattering efficiency of LIG in four glasses as a function of the strength of chemical bond between the former and oxygen ions.

SCB_{F-O} in the sample PbBGe.

Interpretation

Transient gratings

In all the samples investigated, both permanent and transient gratings were created. The initial signal decay having a time scale of the order of a few milliseconds is consistent with the decay of the Eu^{3+} population grating. The slow decay of the LIG signal to the stable value that was observed here in the lithium borate glasses was not seen in the earlier experiments on the phosphate and silicate glasses. This difference can be explained by the different thermal properties of the different types of glasses.

The structural units that form the amorphous nature of these glasses have several possible configurations. The permanent gratings result from a periodic modulation in the configurations of these units. Each unit has a characteristic time for the change from one equilibrium configuration to another that depends upon the temperature. For a given relaxation mechanism in a bulk sample, there generally exists a distribution of relaxation times resulting from the distribution of structural units. For a thermally activated mechanism the distribution of relaxation times is given by [143]

$$\begin{aligned} \tau = & = \tau_o \exp(E_a/RT) \\ & = \frac{\hbar}{kT} \exp(-\Delta S_a/R) \exp(E_a/RT) \end{aligned} \tag{138}$$

where τ is the relaxation time, τ_0 is the pre-exponential factor, h is Planck's constant, k_B is Boltzmann's constant, R is the gas constant, T is the absolute temperature, ΔS_a is the activation entropy, and E_a is the activation energy. A distribution in relaxation times can be caused by either a distribution in the pre-exponential factor, which is related to the activation entropy, or by a distribution in the activation energies. An example of the slow decay observed in the LIG scattering signal is shown in the inset of Fig. 52 where the values of ln (η) vs time are plotted for the LiB4 sample. The nonlogarithmic dependence of the signal decay observed here is consistent with a distribution in the characteristic times of the thermally induced structural relaxation. Although it is not known whether the width of the distribution of the relaxation times in a specific glass is caused by the per-exponential term or by the activation energy, other studies of glass structural changes have been centered on the latter[143].

Effects of the network modifier ions on the FWM scattering efficiency of the LIG's

The lithium-borate glasses show a monotonic increase in scattering efficiency as Q/r^2 of the network modifier ion increases (Fig. 53). The significance of these results is discussed in the first instance for the Mg, Ca, and Ba modifier ions since they are common Group II elements and expected to have similar chemical properties. While it is ultimately the different mass that distinguishes these elements, the appropriate parameter that has the most influence on the scattering efficiencies is the bond strength. The ~300% increase in scattering efficiency from the Ba to the Mg ions is associated with a 400% increase in Q/r^2 and 400% decrease in mass, but only a 12% decrease in the SCB_{M-O}. Since Ba, Ca, and Mg are from the same group it is not surprising that the same dependence of the efficiency on Q/r^2 and mass is observed.

When comparing results from glasses having modifier ions from different parts of the periodic table, the importance of the Q/r^2 and SCB_{M-O} parameters becomes apparent. For example, Ca and Zn modifier ions have the same charge but Zn is the heavier ion (Table X). If these tow ions were part of the same group of elements it would b expected that the Zn sample would show the lower scattering efficiency. In fact the opposite is observed (Fig.53). Compared to Ca, Zn has the better values of the important parameters Q/r^2 and SCB_{M-O} for grating information. The results show that for a given mass, large values of Q/r^2 and small values of SCB_{M-O} are the desired properties for the modifier ions.

In order to understand the m mechanism of grating formation, it is necessary to consider the effects different values of Q/r^2 and SCB_{M-O} have on the ions involved in the process. It has been pointed out before that the rare-earth dopant ions and the network modifier ions compete in attracting the nonbridging oxygen ions[130]. A measure of this attraction is the charge-to-radius-squared ratio, Q/r^2. In Fig. 53 the area bound by the vertical dashed lines represents typical values for Q/r^2 for rare-earth ions. The increase in scattering efficiency with increasing Q/r^2 of the modifier ions is interpreted in the following manner.

In samples having modifier ions with low values of Q/r^2, the Eu^{3+} ions are less effective at attracting the nonbridging oxygen ions. Since the permanent gratings are produced by rearrangements of the nonbridging oxygen ions low values of modifier ion Q/r^2 result in lower asymmetry between altered and unaltered regions at the Eu^{3+} ion sites. This in turn results in a less efficient modulation of the refractive index. As the values of Q/r^2 for the modifier ions increase to approach the values for the rare-earth ions, they become better at stabilizing structural changes involving different arrangements of nonbridging oxygen ions. This leads to a greater modulation in the refractive index which is consistent with the observed dependence of the scattering efficiency.

It is well known that the bond st4rength between the atoms in simple oxides is a strong influence on heir tendency to form glass [144] and it has been shown here to be an important factor in grating formation. For the Group II elements Mg, Ca, and Ba an increase in grating scattering efficiency is observed when the SCB_{M-O} decreases (Fig. 55). Qualitatively this is understood as a stronger bonding between network modifier and oxygen ions results in a less efficient rare-earth-oxygen ion interaction and subsequent lower scattering efficiency. When comparing results between modifier ions from different parts of the periodic table the SCB_{M-O} does not appear to be a strong factor. For example, the samples with Pb and Ba ions exhibit similar scattering efficiencies but these ions have very different values of SCB_{M-O}.

In summary, when attempting to predict the properties of permanent LIG's produced in samples with different modifier ions, it is necessary to consider the positions of the ions relative to each other in the periodic table. For ions from the same part of the table and having similar chemical properties, the SCB_{M-O} and

Q/r^2 parameters are equally good in predicting the expected response. However, for ions from different parts of the periodic table it appears that only the Q/r^2 parameter can be relied on to give some idea of the trend in the efficiency.

When examining the results shown in Fig. 55 of the scattering efficiency as a function of SCB_{M-O}, it is apparent that some comment is required for the glass with Al modifiers. It is well known that Al_2O_3 is a conditional glass former which, in many cases, becomes a part of the main structure of the glass instead of acting as a modifier [145,146]. This is in contrast to the role played by the rest of the modifier ions investigated here which almost always occupy interstitial positions with respect to the main structure of the glass formers. In behaving more like a former than a modifier, Al ions becoming more involved in the covalent bonding of the glass rather than in localized ionic bonding. Thus the values of Q/r^2 may be interpreted as describing the degree of covalence to the modifier-oxygen interaction with large values of Q/r^2 for the modifier ion being associated with a m ore covalent interaction. This fact in itself may lie behind the observation of a very high scattering efficiency from this sample, however, the existence of additional oxygen ions should also be considered.

The glass samples discussed here are formed when nonglass forming oxides of the form MO (e.g., PbO, MgO) are added to glass forming oxides of the type F_xO_y (B_2O_3 for the borate glasses here). However, if the nonglass forming oxide is of the type M_mO_n (e.g., Al_2O_3) the number of oxygen ions is increased relative to the number of glass forming cations F [147]. Thus in lithium borate glasses studied here there are 50% more oxygen ions introduced when Al_2O_3 is present relative to one of the other modifier oxides. Unless the coordination number of the cation F is changed these additional oxygens cannot form linkages between neighboring F cations but must exist as single bonded oxygens, i.e., oxygens that are bonded to only one F cation. At the present time it is not clear if the very high scattering efficiency for the Al_2O_3 sample is the result of the increase in the number of nonbridging oxygen ions or the nature of Al_2O_3 as a conditional glass former.

Effects of the network former ions on the FWM scattering efficiency of the LIG's

The four glasses PbB, PbBGe, PbGe, and PbSi1 have the same network modifier composition but vary in the type and composition of network former (Table IX). This variation produces a change in the SCB_{F-O} between samples. In Fig. 56 the values of the grating scattering efficiency were plotted as a function of the SCB_{F-O} and show a decrease in efficiency as SCB_{F-O} increases in the order B-O>Si-O>Ge-O. This can be understood in a similar manner as the influence of the SCB_{M-O} on the efficiency. Qualitatively the ability of the Eu^{3+} ions to interact with the oxygen ions diminishes with the increasing strength of the interaction between network former and oxygen ions.

The two samples PbSi1 and PbSi2 contain the same elements but differ in the ratio o network former and modifier ions. In Fig. 57 the scattering efficiencies of

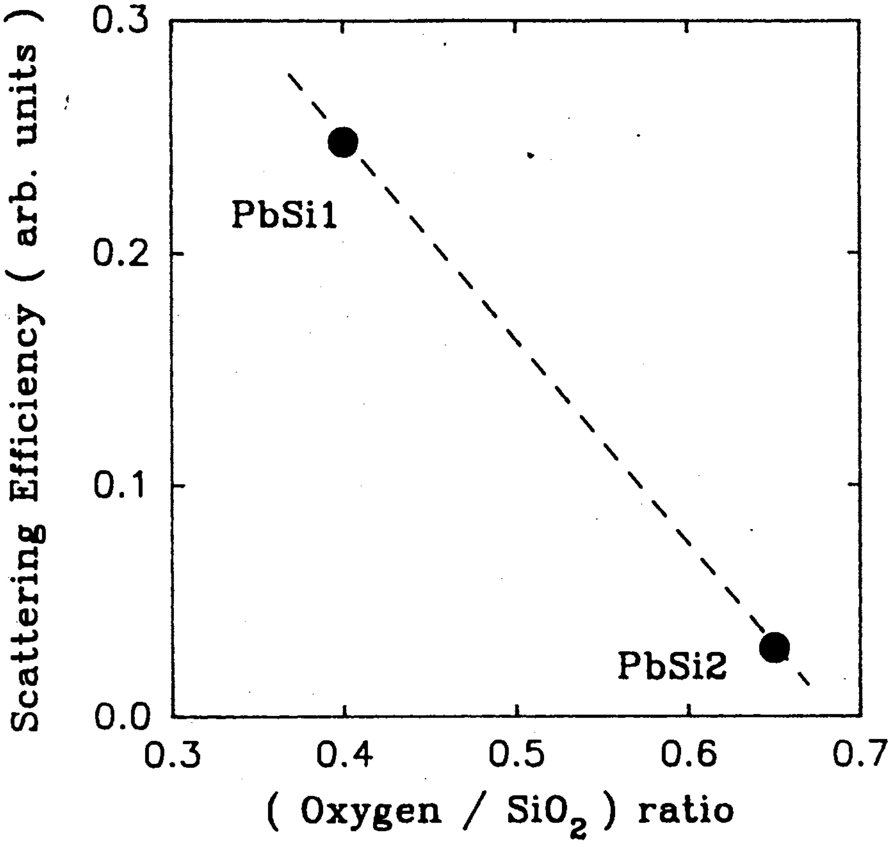

Figure 57. Scattering efficiency as a function of the ration of oxygen/SiO_2.

the permanent LIG's from these two samples are plotted vs the concentration ratio (oxygen/SiO_2) where the oxygen concentration is that contributed by the modifier ions. In PbSi2 t5he additional PbO increases the nonbridging oxygen content and might be expected to improve the scattering efficiency over PbSi1. However, the opposite dependence is observed and it appears that the role of PbO as an oxygen donor in increasing the efficiency is more than offset by the presence of additional heavy Pb modifier ions that decrease the efficiency.

Mechanism of erasure

It has been shown before that the permanent LIG's can be erased by heating the glass. This process involves the thermally activated relaxation of the structural modification created in the local environment of the Eu^{3+}ions. Additionally,the permanent signal can be erased optically by switching on only one of the write beams in resonance with the transition to the $^5D_2$ level of Eu^{3+}. In this case the optical excitation of the Eu^{3+} ions by the single beam creates a *uniform* structural modification in the local environment of the Eu^{3+} ions as before, i.e., the single beam removes the spatial modulation of the structure.

Of particular interest is the observation that a new, permanent LIG can be recreated at exactly the same point in the sample after optical erasure. Figure 58 shows a sequence of grating buildup and erasure curves in a Eu^{3+} silicate glass. In the upper part of this figure the erase beam intensity was 0.25 times the light intensity in the grating peak regions, while in the lower part it was 3.6 times. These results show that the efficiency of recreating a permanent LIG after optical erasure depends upon the actual intensity of the erasure beam.

Some insight into the processes taking place during the optical erasure and recreation can be obtained from an analysis of the time dependence of the signal. The contrast between grating peaks and valleys is provided by regions about Eu^{3+} ions that have undergone local structural change. During optical erasure, the time evolution of the concentration of these localized regions follows a simple rate equation [148]

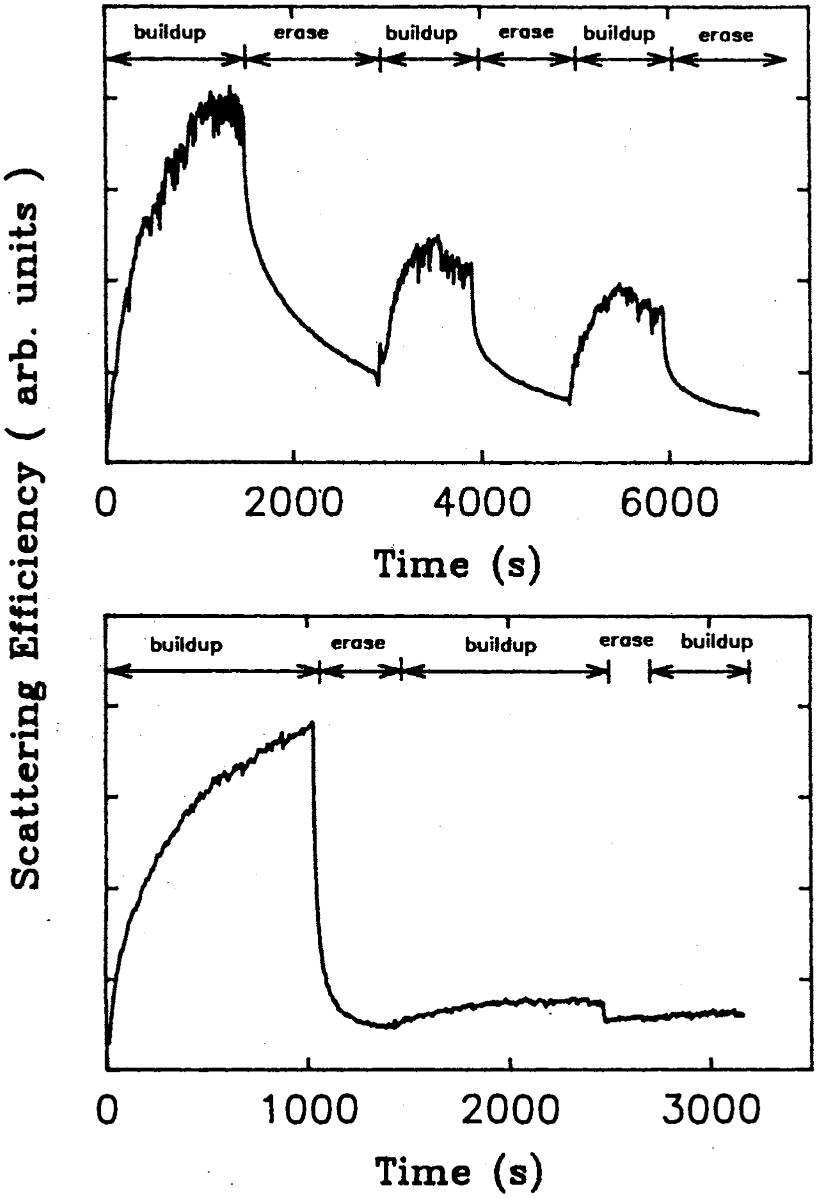

Figure 58. Time dependence of the Scattering efficiency for a series of grating creation and optical erasure experiments done in the same location. In the upper part the erasing beam was 0.25 times the intensity in the grating peak and the lower 3.6 times.

$$\frac{dn}{dt} = -n^x K \exp(-E/kT) \tag{139}$$

where E is the activation energy for the relaxation of the structural modification, K is a constant with units of $s^{-1}$and x is an integer that describes the order of the kinetics. The signal measured is the scattering efficiency, η, which is proportional to the square of the concentration of centers. Then

$$\frac{dn}{dt} \sim \frac{1}{n}\frac{d\eta}{dt} \tag{140}$$

and the expression describing the rate of change of the scattering efficiency is

$$\frac{d\eta}{dt} \sim -\eta^{(x+1)/2} \tag{141}$$

This equation describes the change in the signal as a function of time with the rate of change depending on the interaction between x groups of ions. With an initial condition of η=η_0 at t=0, the solution of Eq. (4) is

$$\left(\frac{\eta}{\eta_o}\right)^{(1-x)/2} = C\eta_o^{(x-1)/2}t + 1 \tag{142}$$

The experimental data of a single optical erasure curve, shown in Fig. 59 were analyzed and the term $(\eta/\eta_0)^{(1-x)/2}$ was plotted vs time for different integer values of x. The value of x giving the best straight line fit is interpreted as the order of tHe kinetics. The data points shown in Figs. 60 (a) and 60 (b) are optical erasure results analyzed using the model with a second and third order kinetics parameter, respectively. These results show a straight line was obtained for x=3. This suggests that the optical erasure involves a kinetic process between three neighboring structural units.

The interpretation of this is that there is an elastic interaction between these neighboring units that are trying to undergo simultaneous and perhaps competing structural changes. The third order kinetics arise as any individual unit is influenced by the changes taking place on either side of it in this one dimensional system defined by the grating wave vector. The center of each unit is a Eu^{3+} ion (or

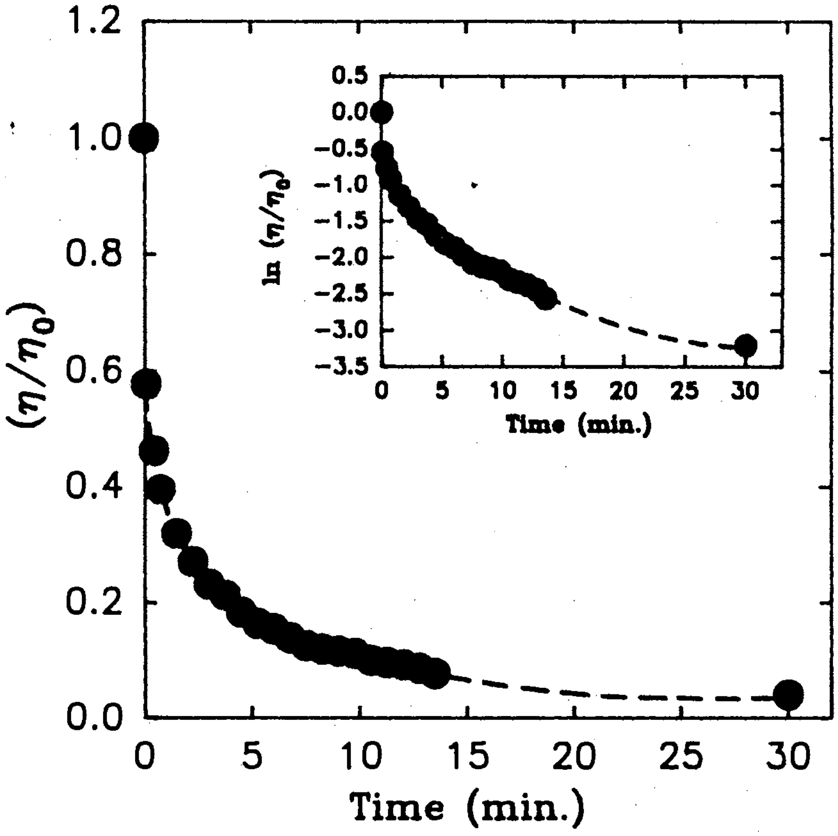

Figure 59. The nonlogarithmic time dependence of optical erasure.

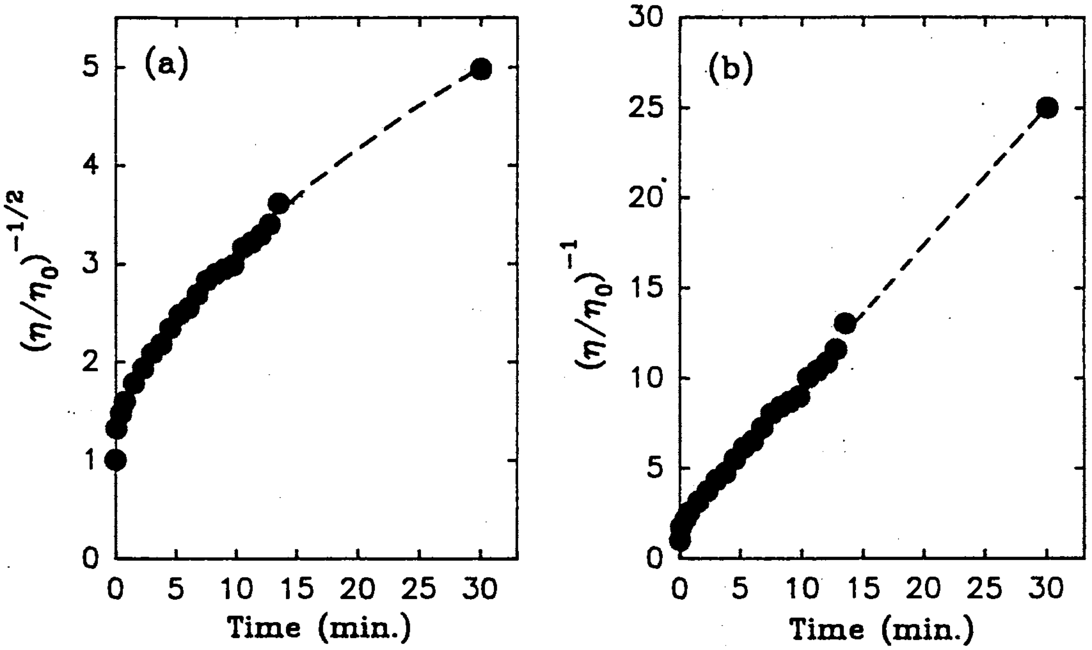

Figure 60. Scattering efficiency data and fit for different kinematic orders (a) $x = 2$ and (b) $x = 3$.

cluster) that acts as the catalyst for introducing thermal energy into the system. In both grating creation and optical erasure the equilibrium stabilization of the neighboring structural modifications can only be accomplished when the units are significantly far apart to eliminate the elastic interaction between them. In this picture only one of two optically active Eu^{3+} ions that are closer together than some critical distance R_0 is at the center of a stabilized structural modification. This critical distance is a function of the structure of the glass, the temperature and the optical intensity being used. This may also explain the saturation effects observed in some of the permanent LIG experiments. The scattering efficiency from a LIG in a metaphosphate glass containing 50 mol % of Eu^{3+} was considered to be saturated when compared to the intensity from a 10 mol % Eu^{3+} sample.[5] The theory predicted a 50-fold increase in scattering efficiency whereas only an 8-fold increase was observed. This saturation may be related to the onset of the regime where the elastic interaction between neighboring structural units extends over the distance between adjacent Eu^{3+} ions.

Discussion

The experimental results presented here show that the chemical composition of the glass host plays a major role in determining the scattering efficiencies of the LIG. By observing the response from different samples a set of empirical rules were developed to predict the relative scattering efficiency of a particular glass. For samples with modifier ions from the same part of the periodic table the charge-to-radius-squared ratio Q/r^2 and the strength of the chemical bond between modifier and oxygen ions SCB_{M-O} are parameters that can be used to predict the relative grating efficiency. For samples with modifier ions from different parts of the periodic table only the Q/r^2 parameter can be relied on to give some idea of the trend in efficiencies. The data show that large values of Q/r^2 and small values of SCB_{M-O} are desired for high scattering efficiencies.

The efficiency of forming a permanent LIG also depends on the glass former ions of the host. These affect the LIG's both through determining the number of nonbridging oxygen ions present and through restricting the polarizability determined by the strength of the former ion-oxygen chemical bond. This was also observed recently in thermal lensing experiments on the same glasses used here [23]. A pulsed laser operating at 457 nm with a duration of 7 ns was used to thermally induce changes in the refractive index. Since the wavelength used did not correspond to any Eu^{3+} absorption it was concluded that the nonbridging oxygen ions were responsible for the changes in refractive index. The results obtained on glasses with different types of former ions were consistent with those obtained in the experiments described here.

The dependencies of the permanent LIG's on host chemical composition are consistent with the local structural modification model proposed previously[124–130]. The nature of the two possible local structures appears to be due to the relocation of the nonbridging oxygen ions near to the rare-earth ions. Multiple local configurations of coordination spheres of rare-earth ions in glasses are well known from other types of investigations. For example, computer simulations of the molecular dynamics of rare-earth doped glass showed the RE oxygen coordination number increasing with the mass of the modifier ion [149,150].

On an experimental level it has been shown that the certain rare-earth doped silicate crystals undergo a structural phase transition at elevated temperatures that may be similar to those modification response for grating formation[151]. In these crystals the time scales for the transitions are the order of several minutes which are similar to the time scales measured here for the LIG buildup. Such a long buildup would indicate the mechanism for grating creation is not photoionization as has been recently suggested[152]. During the grating buildup large numbers of high frequency local vibrational modes are produced on a local scale by the efficient nonradiative decay of the $^5D_2$ level. Under such conditions it is reasonable to conclude that elevated temperatures are produced in the local environment of the Eu^{3+} ion and structural changes occur with corresponding changes in Eu^{3+}-oxygen coordination number and bond lengths.

Having established that structural changes occur in the creation of a permanent LIG, it remains to question the origin of the different values of the refractive index. It was suggested previously[130] that the local change of crystal field of the rare-earth ion changes the radial integral of the $4f \rightarrow 5d$ transition which is the dominant contribution to its polarizability. This predicts a reasonable value for the observed Δn.

However, a second source of variation in the local polarization is density changes due to different positions of the ions. In LIG experiments there are rearrangements of the nonbridging oxygen ions involved in the structural modifications. A change in their position of 0.1 A can produce a local polarization change leading to a refractive index change of $\Delta n = 10^{-5}$, which is the order of magnitude of the observed LIG modulation depth. Thus, the index change may be associated with a polarization change between the two structures that has its origin either in the rare-earth ion or in the nonbridging oxygen ions.

During grating formation the spatial regions undergoing structural modifications experience a decrease in density. This is inferred since the high temperature phase has an increase in volume that results from an increase in the Eu^{3+}-oxygen bond lengths. Consequently, to maintain uniformity there is an increase in the density in the dark regions.

Assuming a simple one dimensional picture, it is possible to write a density

$$\rho = N/x \tag{143}$$

where x is the coordinate along the grating direction and N is the concentration in this direction. Then the change in density between light and dark regions varies as

$$\Delta\rho \sim \frac{N}{x^2}\Delta x = \rho_o \frac{\Delta x}{\Lambda_g} \tag{144}$$

where Λ_g is the grating spacing , ρ_0 the equilibrium density and Δx the coordinate change cause by the structural modification. Since the scattering efficiency is determined by the density fluctuations, the dependence of $\Delta\rho$ on Λ_g predicts a general trend of increasing scattering efficiency with decreasing grating spacing. However, at some point the spacing between neighboring fringes becomes sufficiently small such that the increased density in the dark regions would exceed some critical value determined by the bond strengths and the scattering efficiency should saturate and possibly start to decrease.

After a steady state permanent LIG has been produced in the sample,the periodic density function can be expressed as

$$\rho(x) = \rho_o - \Delta\rho_{P1}\sin(k_g x) \tag{145}$$

where ρ_0 is the original density, k_g is the grating wave vector, and $\Delta\rho_{P1}$ is the change in density caused by the write beams with total power $P1$. In this case the scattering efficiency would be proportional to the square of $\Delta\rho_{P1}$. Optical erasure is done by blocking one of the write beams which results in a constant density function given by

$$\rho(x) = \rho_o - \Delta\rho_{P2} \tag{146}$$

Since the intensity of a single beam is 1/4 of the peak intensity during grating buildup $\Delta\rho_{P2}<\Delta\rho_{P1}$. Now during rewriting of the grating the density in the light regions again returns to i its former value of $\rho_0 - \Delta\rho_{P1}$ but the dark regions remain at the erasure density of $\rho_0 - \Delta\rho_{P2}$. Figure 61 shows plots of these functions. As can be seen, after optical erasure and rewriting the density fluctuation is smaller than before and the grating does not full recover its previous scattering efficiency.

It is known from previous work that the choice of the rare-earth dopant ion in the glass composition has an important effect on the efficiency of any permanent LIG's produced. Both Eu^{3+} and Pr^{3+} have been shown to produce permanent gratings while Nd^{3+} and Er^{3+} do not. The appropriate feature of the former two ions is that they have electronic excited levels that efficiently relax nonradiatively through the emission of high energy local vibrational modes. In Nd^{3+} the lack of a grating was attributed to cascade relaxation between closely spaced energy levels that involved only low energy vibrational modes. When pumped to high energy

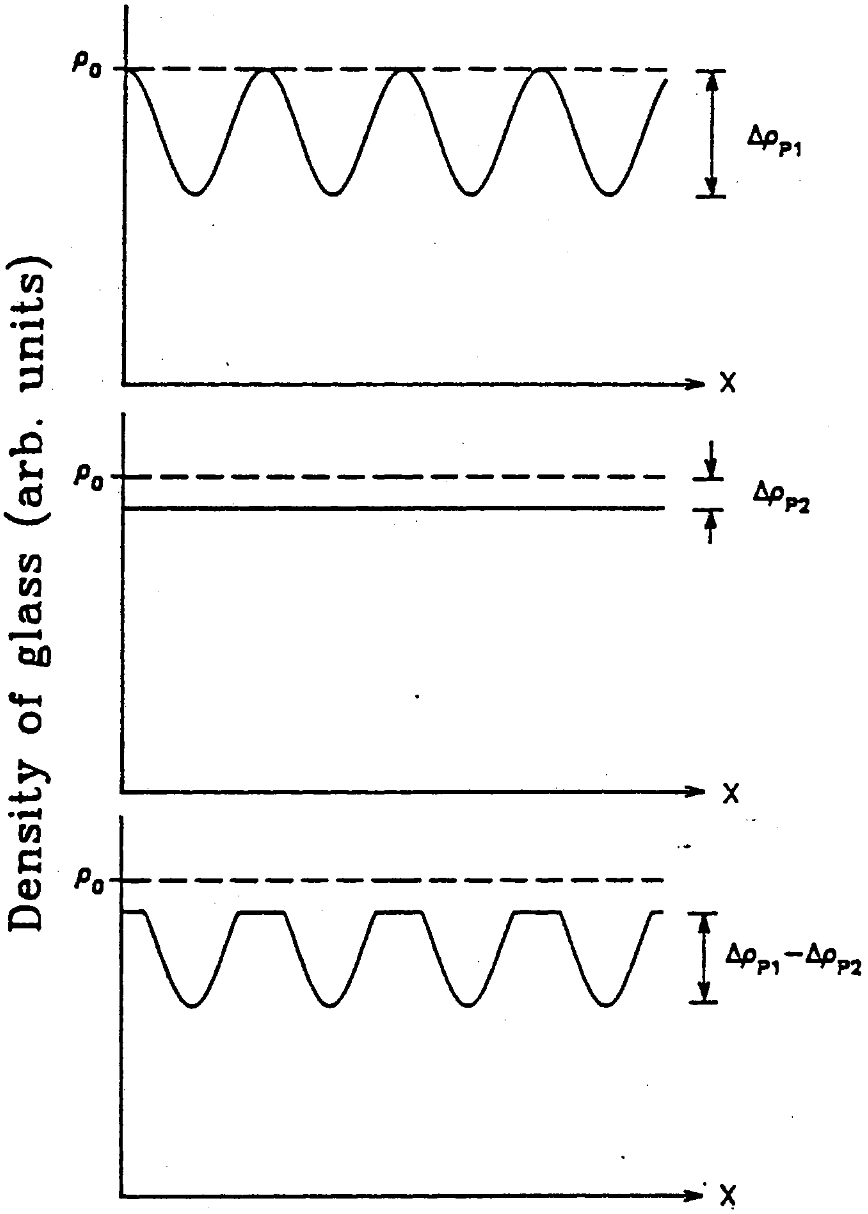

Figure 61. Schematic figure showing the density during LIG creation and erasure. Top: the sinusoidal decrease in initial creation, middle: uniform decrease after eraseure, bottom: smaller grating recovery.

excited levels, Er^{3+} ions under go predominantly radiative decay and this was suggested to be the reason for the absence of a permanent grating [126]. However, recent experiments [152] have not produced permanent gratings when Er^{3+}ions were excited to lower energy levels where efficient nonradiative relaxation does occur. Clearly a different explanation is required and the lack of a permanent grating in Er^{3+} samples may be associated with several different effects. One reason may be the difference in ionic size between Er^{3+} and Pr^{3+}, Eu^{3+} ions and the difference this makes in their interaction with the surrounding nonbridging oxygen ions. Also, based on observations from rare-earth silicate crystals [151] it is more difficult for Er^{3+} doped samples to undergo phase transitions at elevated temperatures that produce the difference between modified and unmodified regions that are observed in permanent LIG's. This was associated with the differences in Si-O bond interactions in the various rare-earth samples [153].

BIBLIOGRAPHY

1. A.D. McAulay, "*Optical Computer Architectures*", John Wiley & Sons, New York, 1991.
2. K.Hwang and F.A.Briggs, "*Computer Architecture and Parallel Processing*", McGraw-Hill Book Company, New York, 1984.
3. M.S. Petrovic, A. Suchocki, R.C. Powell, G.C. Valley and G. Cantwell, *Phys. Rev. B*, **43**, 2228 (1991).
4. F. Zernike and J.E. Midwinter, "*Applied Nonlinear Optics*", John Wiley & Sons, New York, 1973.
5. J.D. Jackson, "*Classical Electrodynamics*", John Wiley & Sons, New York, 1975.
6. M. Born and E. Wolf, "*Principles of Optics*", Pergamon Press, Oxford, 1980.
7. D. Marcuse, "*Light Transmission Optics*", Van Nostrand Reinhold, New York, 1972.
8. P. Meystre, M. Sargent III, "*Elements of Quantum Optics*", Springer-Verlag, New York, 1991.
9. Y.R. Shen, "*The Principles of Nonlinear Optics*", John Wiley & Sons, New York, 1984.
10. C. Kittel, "*Introduction to Solid State Physics*", John Wiley & Sons, New York, 1986.
11. H.J. Eichler, P. Gunter and D.W. Pohl, "*Laser-Induced Dynamic Gratings*", Springer-Verlag, New York, 1986.
12. H. Kogelnik, *Bell Syst. Tech. J.*, **48** 2909.(1968).
13. P.N. Butcher and D. Cotter, "*The Elements of Nonlinear Optics*", Cambridge University Press, New York, 1990.
14. L.V. Keldysh, *Sov. Phys. JETP*, **20**, 1307 (1965).
15. H.S. Brandi and C.B. de Araujo, *J. Phys. C: Solid State Phys.*, **16**, 5929, (1983).

16. H.D. Jones and H.R. Reiss, *Phys. Rev. B*, **16**, 2466 (1977).

17. M. Sheik-Bahae, D.C. Hutchings, D.J. Hagan and E.W. Van Stryland, "Dispersion of Bound Electronic Refraction in Solids", *IEEE J. Quantum Electron*, **27**, 1296 (1991).

18. R. Shankar, "*Principles of Quantum Mechanics*", Plenum Press, New York, 1988.

19. D.M. Valkov, *Z. Phys.*, **94**, 250 (1935).

20. R.K. Jain and M.B. Klein, in "*Optical Phase Conjugation*", Academic Press, New York, 1983.

21. P. Gunter, J.P. Huignard, in "*Photorefractive materials and their applications; vol I*", P. Gunter and J.P. Huignard, Eds., Springer-Verlag, Heidelberg, 1988.

22. R.C. Powell, S.A. Payne, L.L. Chase and G.D. Wilke, *Phys. Rev. B.*, **41**, 8593 (1990).

23. B. Taheri, A. Munoz F., W.D. St John, J.P. Wicksted and R.C. Powell, *J. Appl. Phys.*, **71**, 3693 (1992).

24. J.C. Phillips, "*Bonds and Bands in Semiconductors*", Academic Press, New York, 1973.

25. J.K. Furdyna, *J. Appl. Phys.*, **64**, R29 (1988). See for example, *Semiconductors and Semimetals*, R.K. Willardson and A.C. Beer, Treatise Editors; J.K. Furdyna and J. Kossut, Volume Editors, Academic, Boston, 1988, vol. **25**.

26. D. Weaire, B.S. Wherrett, D.A.B. Miller, and S.D. Smith, *Opt. Lett.*, **4**, 331 (1974).

27. E.W. Van Stryland, H. Vanherzeele, M.A. Woodall, M.J. Soileau, A.L. Smirl, S. Guha and T.F. Boggess, *Optical Engineering*, **24**, 613 (1985).

28. W. Zawadzki, in *Handbook on Semiconductors, vol 1: Band Theory and Transport Properties*, T.S. Moss and W. Paul, Editors, (North Holland, Amsterdam, 1980).

29. K.W. Boer, "*Survey of Semiconductor Physics*", Van Nostrand Reinhold, New York, 1990.

30. B. Taheri, A. Munoz F., R.C. Powell, J.J. Song, and J.K. Furdyna, *SPIE Proceedings*, **2229** (1994).

31. H.J. Eichler, F. Massmann, *J. Appl. Phys.*, **53**, 3237 (1982).

32. K. Jarasiunas and J. Gerritsen, *Appl. Phys. Lett.*, **33**, 190 (1978).

33. D.R. Huffman, *adv. Phys.*, **25**, 129 (1977).

34. H.W. Kroto, J.R. Heath, S.C. O'Brien, R.F. Curl and R.E. Smalley, *Nature*, **318**, 162 (1985).

35. W. Kratschmer, L.D. Lamb, K. Fostiropoulos, D.R. Huffman, *Nature*, **347**, 354 (1990).

36. H. Kroto, *Science*, **242**, 1139 (1988).

37. P.N. Parsad and B.A. Reinhardt, *Chem Mater.*, **2**, 660 (1990).

38. H. Hoshi, N. Nakamura, T. Nakagawa, S. Suzuki, H. Shiromaru and Y. Achira, *Jpn. J. Appl. Phys.*, **30**, L1397 (1991).

39. Y. Wang and L.T. Cheng, *J. Phys. Chem.*, **96**, 1530 (1992).

40. R. Vijaya, Y.V.G.S. Murti, G. Sundarajan, C.K. Mathews, and P.R. Vasudeva Rao, *Opt. Commun.*, **94**, 353 (1992).

41. W.J. Blau, H.J. Byrne, D.J. Cardin, T.J. Dennis, J.P. Hare, H.W. Kroto, R.Taylor, and D.R.M. Walton, *Phys. Rev. Lett.*, **67**, 1423 (1991).

42. Z.H. Kafafi, J.R. Lindle, R.G.S. Pong, F.J. Bartoli, L.J. Lingg, and J. Milliken, *Chem. Phys. Lett.*, **188**, 492 (1992).

43. Z. Zhang, D. Wang, P. Ye, Y. Li, P.Wu, and D. Zhu, *Opt. Lett.*, **17**, 973 (1992).

44. M.J. Rosker, H.O. Marcy, T.Y. Chang, J.T. Khoury, K. Hansen, and R.L. Whetten, *Chem. Phys. Lett.*, **196**, 427 (1992).

45. J.F. Nye, "*Physical Properties of Crystals*", Oxford University Press, London, 1976.

46. M.D. Fayer, *IEEE J. Quantum Electron.*, **QE-22**, 1437 (1986).

47. Y.X. Yan, L.T. Cheng, and K.A. Nelson, *J. Chem. Phys.*, **88**, 6477 (1988).

48. S. Kinoshita, W. Tsurumaki, Y. Shimada, and T. Yagi, *J. Opt. Soc. Am. B*, **10**, 1017 (1993).

49. K.A. Nelson, and M.D. Fayer, *J. Chem. Phys.*, **72**, 5202 (1980).

50. K.A. Nelson, D.R. Lutz, M.D. Fayer, and L. Madison, *Phys. Rev. Lett.*, **68**, 2705 (1992).

51. Z.H. Kafafi, F.J. Bartoli, J.R. Lindle, and R.G.S. Pong, *Phys. Rev. Lett.*, **68**, 2705 (1992).

52. S.N. Sen, "*Acoustics, Waves and Oscillations*", John Wiley & Sons, New York, 1990).

53. R.J. Sension, C.M. Phillips, A.Z. Szarka, W.J. Romanow, A.R. McGhie, J.P. McCauley Jr., A.B. Smith III, and R.M. Hchstrausser, *J. Phys. Chem*, **95**, 6075 (1991).

54. T.W. Ebbesen, K. Tanigaki, and S. Kuroshima, *Chem. Phys. Lett.*, **181**, 501 (1991).

55. G. Le Saux and A. Brun, *IEEE J. Quantum Electron.,* **QE-23**, 1680 (1987).

56. D. C. Jones and L. Solymar, *Opt. Comm.*, **85**, 372 (1991).

57. J. M. C. Jonathan, G. Roosen, and Ph. Roussignal, *Opt. Lett.,* **13**, 224 (1988).

58. G. Le Saux, G. Roosen, and A. Brun, *Opt. Comm.,* **56**, 374 (1986).

59. J. P. Hermann, J. P. Herriau, and J. P. Huignard, *App. Opt.,* **20**, 2173 (1981).

60. J.-L. Ferrier, J. Gazengel, X. N. Phu, and G. Rivoire, *Opt. Comm.,* **58**, 343 (1986).

61. G. Le Saux, J. C. Launay, and A. Brun, *Opt. Comm.*, **57**, 166 (1986).

62. A. Smirl, K. Bohnert, G. C. Valley, R. A. Mullen, and T. Boggess, *J. Opt. Soc. Am.,* **6**, 606 (1989).

63. L. Lam, T. Y. Chang, J. Feinberg, and R. Hellwarth, *Opt. Lett.,* **6**, 475 (1981).

64. I. Biaggio, M. Zqonik, and P. Gunter, *Opt. Comm.*, **77**, 312 (1990).

65. C.-T. Chen, D. Kin, and D. von der Linde, *IEEE J. Quantum Electron.,* **QE-16**, 126 (1980).

66. R. J. Reeves, H. Liu, and R. C. Powell, to be published *Phy. Rev. B.*

67. I. Foldvari, B. Taheri, R. J. Reeves, and R. C. Powell, *Opt. Comm.,* **102**, 245 (1993).

68. J.P. Huignard and F.Micheron; *Appl. Phys. Lett.*, **29**, 591 (1976).

69. G.C. Valley, M.B. Klein, R.A. Mullen, D. Rytz and B. Wechsler; *Ann. Rev. Mater. Sci.*, **18**, 165 (1988).

70. L. Arizmendi, J.M. Cabrera and F. Agullo-Lopez; *internat. J. Optoelectr.*, **7**, 149 (1992).

71. S.L. Hou, R.B. Lauer and R.E. Aldrich; *J. Appl. Phys.*, **44**, 2652 (1973).

72. B.C. Grabmayer and R. Oberschmidt; *Phys. Stat. Sol. (a)*, **96**, 199 (1986).

73. R.Oberschmidt; *Phys. Stat. Sol. (a)*, **89**, 263 (1985).

74. W. Rechwald, K. Frick, G.K. Lang and E. Meier; *J. Appl. Phys.*, **47**, 1292 (1976).

75. M.T. Harris, J.J. Larkin and J.J. Martin; *Appl. Phys. Lett.*, **60**, 2162 (1992).

76. P.Gunter; *Phys. Reports*, **93**, 93 (1982).

77. I. Foldvari, L.E. Halliburton, G.J. Edwards and L.Otsi; *Sol. State. Commun.*, **77**, 181 (1991).

78. J.J. Martin, I. Foldvari and C.A. Hunt; *J. Appl. Phys.*, **70**, 7554 (1991).

79. J.M.C. Jonathan, G.Roosen and Ph. Roussignal; *Opt. Lett.*, **13**, 224 (1988).

80. G. Le Saux, G. Roosen and A.Brun; *Opt. Commun.*, **56**, 374 (1986).

81. A.L. Khromov, M.P. Petrov and A.A. Kamshilin; *Sov. Phys. Sol. State*, **36**, 278 (1990).

82. G. Pauliat and G. Roosen; *J. Opt. Soc. Amer. B*, **7**, 2259 (1990).

83. G. Le Saux and A. Brun; *IEEE J. Quant. Electr.*, **23**, 1680 (1987).

84. D.C. Jones and L. Solymar; *Opt. Commun.*, **85**, 372 (1991).

85. D. von der Linde, A.M. Glass and K.F. Rodgers; *Appl. Phys. Lett.*, **25**, 155 (1974).

86. D. von der Linde, A.M. Glass and K.F. Rodgers; *Appl. Phys. Lett.*, **26**, 22 (1975).

87. T.F. Bogges, J.O. White and G.C. Valley; *J. Opt. Soc. Amer. B*, **7**, (1990).

88. M.Sylla, D. Rouede, R. Chevallier, N.P. Xuan and G. Rivoire; "*Tech. Dig. Topical Meeting on Photorefractive materials, Effects, and Devices II.*" (Opt. Soc. Amer., Washington D.C., 1990) p. 193.

89. I. Foldvari, J.J. Martin, C.A. Hunt, R.C. Powell and R.J. Reeves; *J. Appl. Phys.*, **74**, 783(1993).

90. I. Foldvari, A. Peter, R. Voszka and L.A. Kappers, *J. Crystal Growth,* **100**, 75 (1990).

91. B. Frit and M. Jaymes, *Rev. Chim. Miner.,* **3**, 453 (1971).

92. L.A. Demina, B.A. Dolgikh, B.A. Popovkin and A.V. Novoselova, *Dokl. Akad. Nauk. SSSR Ser. Khim.,* **244**, 94 (1979).

93. V.P. Avramenko, A.Yu. Kudzin, S.P. Reprentcheva, L.Ya. Sadovskaya and G.H. Sokolyanskii, *Ferroelectr.,* **82**, 173 (1988).

94. V.V. Kucha, A.V. Khomich, V.B. Kravchenko and P.I. Perov, *Izv. Akad. Nauk. SSSR Ser. Neorg. Mater.,* **20**, 414 (1984).

95. V.P. Avramenko, L.Ya. Sadovskaya, G.Kh. Sokolyanskii and O.V. Agafonov, *Bull. Acad. Sci. SSR. Ser. Phys.,* **54**, 184 (1990).

96. A.A. Astafev, A.A. Abdullaev, O.I. Vorobeva, V.A. dolgikh, B.A. Popovkin, I.M. Silvestrova and E.M. Spiridonov, *Izv. Adak. Nauk. SSSR Neorg. Mater.,* **27**, 60 (1991).

97. G. Mandula, L. Kovacs, A. Peter and E. Hartmann, *Opt. Mater.,* **1**, 161 (1992).

98. I. Foldvari, A. Peter, L.A. Kappers, O.R. Gilliam and R. Capelletti, *J. Meter. Sci.*, **27**, 750 (1992).

99. I. Foldvari, M.P. Scripsick, L.E. Halliborton and A. Peter, *Phys. Lett. A,* **154**, 84 (1991).

100. I. Foldvari, H. Liu, R.C. Powell and A. Peter, *J. Appl. Phys.,* **71**, 5465 (1992).

101. I. Foldvari, H. Liu and R. C. Powell, *SPIE Proc.,* **1626**, 9 (1992).

102. I. Foldvari, R.C. Powell, H. Liu and A. Peter, *Opt. Mater.*, **2**, 175 (1993).

103. M. D. Ewbank, R. R. Neurgaonkar, W. K. Cory, and J. Feinberg, *J. Appl. Phys.,* **62**, 374 (1987).

104. D. Rytz, B. A. Wechsler, R. N. Schwartz, C. C. Nelson, C. D. Brandle, A. J. Valentino, and G. W. Berkstresser, *J. Appl. Phys.,* **66**, 1920 (1989).

105. G. Salamo, M. J. Miller, W. W. Clark III, G. L. Wood, and E. J. Sharp, *Opt. Commun.* **59**, 417 (1986).

106. D. Mercurio, M. El Farissi, B. Frit, and P. Goursat, *Mater. Chem. Phys.,* **9**, 467 (1983).

107. H. Liu, and R.C. Powell, *J. Appl. Phys.*, **70**, 20 (1991).

108. G. L.Wood, W. W. Clark III, M. J. Miller, E. J. Sharp, G. Salamo, and R. R. Neurgaonkar, *IEEE J. Quantum Electron.,* **QE-22**, 2126 (1987).

109. J. B. Thaxter and M. Kestigian, *Appl. Opt.,* **13**, 913 (1974).

110. T. J. Hall, R. Jaura, L. M. Connors, and P. D. Foote, *Prog. Quant. Electr.*, **10**, 77 (1985).

111. A. L. Smirl, G.C. Valley, R. A. Mullen, K. Bohnert, G.D. Mire and T.F. Boggess, *Opt. Lett.*, **7**, 501 (1987).

112. R.J. Reeves, M.G. Jani, R.C. Powell and G.J. Mizell, *J. Luminesc.,* **45**, 419 (1990).

113. R.J. Reeves, M.G. Jani, B. Jassemnejad, R.C. Powell, G.J. Mizell and W. Fay, *Phys. Rev. B,* **43**, 71 (1991).

114. I. Biaggio, M. Zgonik and P. Gunter, *Opt. Commun.,* **77**, 312 (1990).

115. H. Liu, R.C. Powell and L.A. Boatner, *J. Appl. Phys.,* **70**, 20 (1991).

116. H. Liu, R.C. Powell and L.A. Boatner, *Phys. Rev. B,* **44**, 2461 (1991).

117. J.M.C. Jonathan, G. Roosen and Ph. Roussignol, *Optics Lett.,* **13**, 224 (1988).

118. I. Foldvari, B. Taheri, R.J. Reeves and R.C. Powell, *Opt. Commun.,* **102**, 245 (1993).

119. J.L. Ferrier, J. Gazengel, X.N. Phu and G. Rivoire, *Optics Commun.,* **58**, 343 (1986).

120. G. Lesaux, G. Roosen and A. Brun, *Optics Commun.,* **56**, 374 (1986).

121. G.C. Valley, *IEEE J. Quant. Electr.,* **QE-19**, 1637 (1983).

122. C. Medrano, E. Voit, P. Armhein and P. Gunter, *J. Appl. Phys.,* **64**, 4668 (1988).

123. R. Orlowski and E. Kratzig, *Solid State Commun.*, **27**, 1351 (1978).

124. F.M. Durville, E.G. Behrens, and R.C. Powell, *Phys. Rev. B,* **34**, 4213 (1986).

125. F.M. Durville, E.G. Behrens, and R.C. Powell, *Phys. Rev. B*, **35**, 4109 (1987).

126. E.G. Behrens, F.M. Durville, and R.C. Powell, *Opt. Lett.*, **11**, 653 (1986).

127. E.G. Behrens, F.M. Durville, and R.C. Powell, *Phys. Rev. B*, **39**, 6076 (1989).

128. E. G. Behrens, R.C. Powell, and D. H. Blackburn, *Appl. Opt.*, **29**, 1619 (1990).

129. E. G. Behrens, R.C. Powell, and D. H. Blackburn, *J. Opt. Soc. Am. B*, **7**, 1437 (1990).

130. V.A. French, R.C. Powell, D.H. Blackburn, and D.C. Cranmer, *J. Appl. Phys.*, **69**, 913 (1991).

131. R. Reisfeld, A. Honigbaum, and G. Michaeli, *Israel J. Chem.*, **7**, 613 (1969).

132. J.T. Fournier and R.H. Bartram, *J. Phys. Chem. solilds*, **31**, 2615 (1970).

133. R. Reisfeld, J. Hormodaly, and B. Barnett, *Chem. Phys. Lett.*, **17**, 248 (1972).

134. R. Reisfeld, *Structure and Bonding*, **Vol. 13**, 53 (1972).

135. R.A. Velapoldi, R. Reisfeld, and L. Boehm, *Phys. Chem. Glasses*, **14**, 101 (1973).

136. K.O. Hill, Y. Fujii, D.C. Johnson, and B.S. Kawasaki, *Appl. Phys. Lett.*, **32**, 647 (1978).

137. R. Reisfeld and Y. Eckstein, *J. Solid State Chem.*, **5**, 174 (1972).

138. J. Krogh-Moe, *Phys. Chem. Glasses*, **1**, 26 (1960).

139. *Handbook of Chemistry and Physics*, 70th ed. , CRC, Cleveland, 1990.

140. M.K. Murthy and B. Scroggie, *Phys. Chem. Glasses,* **7**, 68 (1966).

141. R. Reisfeld and N. Lieblich, *J. Phys. Chem. Solids*, **34**, 1467 (1973).

142. L. Ya Mazelev, "*Borate Glasses*" (Translated from Russian by Consultant Bureau, New York, 1960).

143. D.W. Moore and D.E. Day, *Phys. Chem. Glasses*, **12**, 75 (1971).

144. W. Vogel, "*Chemistry of Glass*", The American Ceramic Society, columbus, 1985.

145. A. Paul, "*Chemistry of Glasses*", Chapman and Hall Ltd., London, 1982.

146. P. Beekenkanp, *Phys. Chem. Glasses*, **9**, 14 (1968).

147. H.M. Heaton and H. Moore, *J. Soc. Glass Tech.*, **41**, 3 (1957).

148. N. Itoh, B.S.H. Boyce, and R. Smoluchowsky, *Phys. Rev.*, **137**, A1010 (1965).

149. S.N. Alekseichyk, Yu. E. Sverchkov, and S.E. Sverchkov, *Phys. Chem. Glasses*, (to be published).

150. S.A. Brawer and M.J. Weber, *J. Chem. Phys.*, **75**, 3522 (1981).

151. J. Felsche, *J. Less-Common Metals*, **21**, 1 (1970).

152. M.M. Broer, A.J. Bruce, and W.H. Goodkiewicz, presentation at the '8th International Conference on Dynamical Processes in Excited States of Solids,' Leiden, The Netherlands, August 1991 (unpublished).

153. J. Felsche, *Structure and Bonding*, **Vol. 13**, 99 (1972).

APPENDIX

APPENDIX A

Fresnel-Kirchoff Integral

Let us start with the scalar wave equation in free space:

$$(\nabla^2 + k_o^2)\psi(\mathbf{x}) = 0 \tag{A.1}$$

with k_o being the wavevector in free space. We can solve this in general using Green' theorem[5] to find the scalar field inside of a volume V enclosed by a surface S':

$$\psi(\mathbf{x}) = \oint_{S'} [\psi(\mathbf{x}')\mathbf{n} \cdot \nabla G(\mathbf{x},\mathbf{x}') - G(\mathbf{x},\mathbf{x}')\mathbf{n}'.\nabla'\psi(\mathbf{x}')]dS' \tag{A.2}$$

where $\mathbf{n}$ is an inward directing vector normal to the surface. The primes denote the integration coordinates and $G(\mathbf{x},\mathbf{x}')$ is the Green's function for the scalar wave equation satisfying:

$$(\nabla^2 + k_o^2)G(\mathbf{x}) = -\delta(\mathbf{x}-\mathbf{x}') = -\delta(\mathbf{r}) \tag{A.3}$$

which has a solution:

$$G = \frac{e^{iks}}{s} \tag{A.4}$$

From Eq. A.2 we have:

$$\psi(\mathbf{x}) = \int_{S'} \left\{ \psi(\mathbf{x}')\frac{\partial}{\partial n'}\left(\frac{e^{iks}}{s}\right) - \frac{e^{iks}}{s}\frac{\partial\psi(\mathbf{x}')}{\partial n'} \right\} dS' \tag{A.5}$$

In the above, s, denotes the distance from the source, P_1, on the surface S_1 to the observation point, P_2. At this point three routes can be taken. The first uses

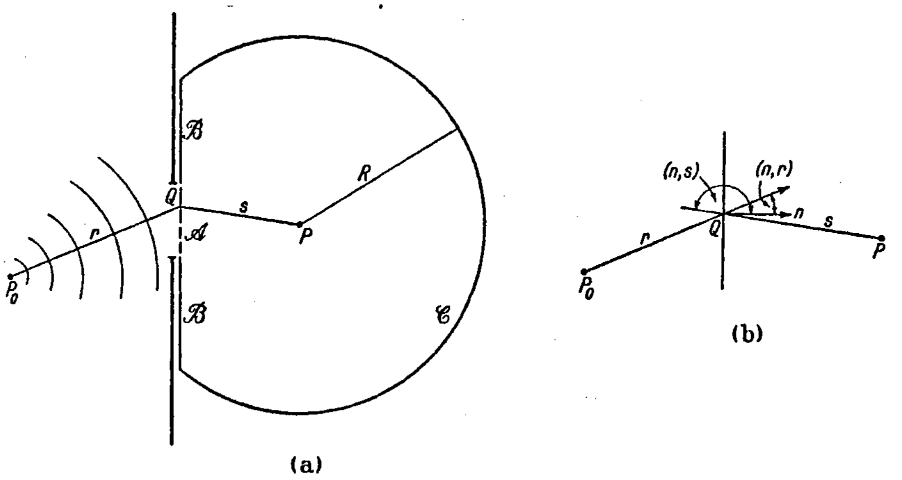

Figure 62. Geometry used for calculation of Fresnel-Kirchoff integral.

Neumann boundary condition which is used if $\partial\psi/\partial n$ is known on the surface. For this case we require a Green's function with the $\partial G/\partial n = 0$ on the surface. Alternatively, if ψ is known on the surface we use the Dirichlet boundary condition, $G = 0$ on the surface. Lastly we can use the Kirchoff's approximation which states that ψ and $\partial\psi/\partial n$ are only none zero at an opening on a surface. and their values equal to the values in the absence of a surface. Strictly speaking, only the first two methods are mathematically correct. However, in the domain were the above is analysis is valid, all three approaches yield similar results [5].

As an application of the above idea, we will attempt to determine the field at a point P due to a point charge, P_o, separated from P by an infinite screen with an opening. The geometry is presented in Fig. 62 taken from ref. [6]. Integration over the surface S', enclosing the observation point reduces to integration over the surfaces $\mathcal{A}, \mathcal{B}$, and $\mathcal{C}$. For times less than arrival times required for any light disturbances from the surface $\mathcal{C}$ [6] and assuming Kirchoff's approximation ($\psi \simeq \partial\psi/\partial n \simeq 0$), the integration over S' reduces to:

$$E(P) = -\frac{iE(P_o)}{2\lambda}\int_A \frac{e^{ik(r+s)}}{rs}[\cos(n,r) - \cos(n,s)]dA \tag{A.6}$$

For paraxial beam $\{\cos(n,r)-\cos(n,s)\simeq 2\}$and recalling that the strength of the field at any point on the opening is given by:

$$E(dA)=\frac{E(P_o)e^{ikr}}{r} \tag{A.7}$$

we get

$$E(P_2)=-\frac{ik}{2\pi}\int_S E(P_1)\frac{e^{iks}}{s}dS \tag{A.8}$$

which basically states the relation needed.

VITA

BAHMAN TAHERI

Candidate for the Degree of

Doctor of Philosophy

Thesis: CHARACTERIZATION OF SOLID STATE MATERIALS FOR USE AS OPTICAL SPATIAL LIGHT MODULATORS

Major Field: Physics

Biographical:

Personal Data: Born in Tehran, Iran, September 3, 1965, the son of Fereidoun and Mehry Taheri.

Education: Bachelor of Science in Physics from California Polytechnic State University, San Luis Obispo, California, June, 1989; Master of Science in Physics from Oklahoma State University, Stillwater, Oklahoma, July, 1992; Completed the requirements for the Doctor of Philosophy degree at Oklahoma State University, Stillwater, Oklahoma, December 1994.